UNIVERSITÀ DEGLI STUDI DI TRIESTE

XXVI CICLO DEL DOTTORATO DI RICERCA IN GEOSCIENZE

Crustal tomography of the Po Plain and calibration of location procedures

Settore scientifico-disciplinare: GEO 10

DOTTORANDA:
LARA TIBERI

COORDINATORE DEL COLLEGIO DEI DOCENTI:
Dott. GIOVANNI COSTA

SUPERVISORE DI TESI:
Dott. GIOVANNI COSTA

Anno Accademico 2012-2013

La fisica è decisamente troppo difficile per i fisici.
David Hilbert

Contents

Riassunto **7**

Introduction **13**

1 Picking and Location Methodologies **19**
1.1 STA/LTA algorithm 20
1.2 AIC function 22
1.3 Hypoellipse 25
1.3.1 Geiger's method 25
1.4 HypoDD 26
1.4.1 HypoDD technique 27
1.5 AutoPicker 27
1.5.1 AIC detector 27
1.6 Antelope 33

2 The Emilia sequence of May-June 2012 **37**
2.1 Database preparation 38
2.2 Manual picking and location 39

3 AutoPicker test: Comparison with manual pickings **57**
3.1 Data Set 57
3.2 Results 61

4 AutoPicker test: Comparison with Antelope **65**
4.1 Data Set 65
4.2 Results 68
4.3 Preliminary implementation 70

5 Travel-time tomography: Cat3D software **77**
5.1 Local earthquake tomography (LET) 77
5.1.1 Basic theory 78
5.2 Cat3D travel-time tomography 79

5.2.1 Wave choice and ray tracing 79
5.2.2 Inversion method 83
5.3 Attendibility of the inversion 84
5.3.1 Attendibility of the tomographic system 84
5.3.2 Error estimation 87
5.4 Particular procedures: Staggered grids 90

6 Travel-time tomography **91**
6.1 Study of the tomographic problem 91
6.2 Choice of the horizontal grid and checkerboard test 96
6.3 Tomographic results 108
6.4 Location solutions 110
6.5 Conclusions 118

7 Automatic and manual traveltimes tomography **121**
7.1 Input Data 121
7.2 Tomographic results and comparison 122
7.2.1 Location results 123
7.2.2 Tomographic results 124
7.3 Conclusions 127

Conclusions **131**

Acknowledgements **135**

References **136**

Riassunto

I terremoti costituiscono un disastro naturale ricorrente su tutto il territorio italiano e per questo sono estremamente importanti interventi mirati e rapidi di protezione civile. La rapidità di questi interventi dipende dalla produzione di localizzazioni veloci e possibilmente in tempo reale degli eventi sismici. La precisione delle localizzazioni, inoltre, è necessaria per identificare le faglie sismogenetiche. Per questi due aspetti, è necessario un miglioramento dei sistemi di monitoraggio esistenti in modo da poter accrescere la qualità delle localizzazioni automatiche in tempo reale. Lo scopo di questo studio è la scrittura di una procedura che localizza accuratamente eventi sismici in tempo reale.

La qualità delle localizzazioni è fortemente dipendente dalla corretta determinazione delle fasi P ed S. A volte è difficile riconoscere il corretto arrivo di una fase, poiché il segnale sismico può essere di difficile lettura per differenti motivi, come, ad esempio, la complessità del meccanismo della faglia generatrice e la presenza di rumore sia naturale che artificiale. Per questo motivo abbiamo studiato, analizzato e comparato differenti metodi per la rilevazione delle fasi e per la localizzazione degli eventi sismici. Gli algoritmi di rilevazione delle fasi che sono stati valutati sono lo Short Time Average su Long Time Average ratio (STA/LTA) e la funzione di Akaike Information Criterion (AIC). Il primo di questi è una tecnica comune usata per distinguere il segnale sismico dal rumore. E' basato sul calcolo continuo di due valori medi dell'ampiezza assoluta di un segnale sismico in due finestre di tempo di differente lunghezza: media sull'intervallo breve (STA) e media sull'intervallo lungo (LTA). Il rapporto di queste due medie (STA/LTA) viene comparato ad un valore di soglia. Quando questo rapporto è maggiore della soglia, viene rilevata una fase nel segnale sismico analizzato. Il settaggio di questo sistema dipende dalla scelta dei parametri, questo prouce instabilità.

La funzione di AIC è una metodologia sofisticata e precisa [Akaike and Hirotugu, 1974], basata sul classico metodo della massima verosimiglianza. La sua applicazione più comune consiste nella selezione tra più modelli: la stima della massima verosimiglianza dei parametri del modello da il min-

imo della funzione AIC. Questo metodo è strettamente correlato alla scelta della finestra di tempo nella quale applicare la funzione. Per questo motivo è necessaria una combinazione di più tecniche in modo da poter scegliere automaticamente la finestra corretta. In un segnale sismico il minimo della funzione AIC identifica l'arrivo delle onde P o delle onde S. Questa funzione è utilizzata nella procedura dell'AutoPicker [Turino et al., 2010].

Una volta identificate le fasi, è necessario elaborarle in modo da poter localizzare eventi sismici. In Antelope la procedura di localizzazione è chiamata orbassoc. Questa metodologia legge le fasi rilevate tramite il metodo STA/LTA e cerca di produrre una localizzazione dell'evento sulle tre possibili griglie: telesismica, regionale e locale. La soluzione, che produce tempi teorici di percorrenza per ogni stazione, che si accordano maggiormente con le osservazioni, viene considerata la migliore. Nell'AutoPicker l'algoritmo di localizzazione è Hypoellipse [Lahr, 1979], nel quale i tempi di percorrenza sono stimati utilizzando una struttura a strati piani paralleli e gli ipocentri sono calcolati utilizzando il metodo di Geiger [Geiger, 1912].

In questo lavoro abbiamo utilizzato metodologie per la localizzazione diverse da quelle assolute come Hypoellipse. L'HypoDD [Waldhauser and Ellsworth, 2000] è un algoritmo relativo, ovvero le localizzazioni vengono calcolate in riferimento alla localizzazione di un evento principale o dal sito di una stazione. Questo metodo può essere applicato solo nel caso in cui la distanza ipocentrale tra i due terremoti è piccola comparata alla distanza evento-stazione e alle eterogeneità laterali del campo delle velocità. In questi casi il percorso del raggio tra le due sorgenti e una stazione comune sono simili per gran parte del percorso del raggio.

Per testare le prestazioni dell'AutoPicker, lo abbiamo applicato ad un database di 250 eventi registrati nell'area di contatto tra le Alpi e le Dinaridi nell'anno 2011 dalla rete C3ERN - the Central Eastern European Earthquake Reasearch Network [Dipartimento di Matematica e Geoscienze (DMG), Istituto Nazionale di Oceanografia e di Geofisica Sperimentale (OGS), Agencija RS za okolje (ARSO) e Zentralanstalt fr Meteorologie und Geodynamik (ZAMG)]. L'algoritmo automatico proposto è risultato essere un utile strumento per l'assegnazione automatica degli arrivi delle onde P ed S. Questo risultato incoraggiante ci ha permesso di procedere nel confronto tra questa nuova metodologia e Antelope, utilizzato da noi quotidianamente in tempo reale per rilevare fasi e localizzare eventi.

La complessità del contesto tettonico influenza il percorso dei raggi e conseguentemente la localizzazione degli eventi. In regioni dove sono presenti molte strutture sismogenetiche, una localizzazione precisa della sequenza sismica è essenziale, in modo da capire quale è la faglia generatrice. In questi casi l'uso di modelli 1-D potrebbe non essere sufficiente, mentre un modello

3-D potrebbe descrivere al meglio l'area interessata. La tomografia dei primi arrivi è una tecnica comune per ottenere un modello tridimensionale dalla localizzazione degli eventi. In questo studio abbiamo utilizzato una tomografia di eventi locali (Local Earthquake Tomography, LET) [Aki, 1982].

La tomografia dei primi arrivi e la localizzazione 3-D degli eventi sono state eseguite, rispettivamente, utilizzando il Computer Aided Tomography per modelli 3D (Cat3D) [Cat3D user manual, 2008] e il Non Linear Location (NonLinLoc) [Lomax et al., 2000] attraverso una procedura iterativa. Il Cat3D viene utilizzato solitamente in sismica attiva, mentre in questo studio è stato applicato ad un caso sismologico. La principale differenza tra la sismica attiva e la sismologia sono le incertezze nel sistema tomografico. Nella sismica attiva la localizzazione della sorgente è ben definita mentre nella sismologia è una variabile con incertezza elevata che si propaga nella stima del percorso del raggio e dei tempi di percorrenza. Per risolvere questo problema, abbiamo utilizzato una procedura iterativa composta dalla tomografia dei primi arrivi e dalla rilocalizzazione degli eventi con il modello 3-D risultante.

Dopo il verificarsi della sequenza sismica emiliana nel Maggio-Giugno 2012, abbiamo deciso di analizzarla come interessante caso di studio. La sequenza sismica è iniziata il 20 Maggio (02:03:53 UTC), con un terremoto di Ml 5.9 [Scognamiglio et al., 2012]. Questa sequenza è composta da migliaia di eventi, sei dei quali con Ml maggiore di 5.0, tra cui un evento di magnitudo locale 5.8, il 29 Maggio (07:00:03 UTC).

Su questi eventi abbiamo testato le prestazioni dell'AutoPicker e di Antelope. Per fare ciò abbiamo rilevato manualmente le fasi e localizzato alcuni degli eventi maggiori della sequenza sismica. Questi eventi sono caratterizzati da fasi P, ma in particolar modo fasi S, difficili da rilevare, probabilmente a causa del complesso meccanismo di faglia. Inoltre la complessità del sistema tettonico assieme all'incertezza della profondità focale rendono problematiche le localizzazioni degli eventi. La sequenza sismica emiliana ha interessato un'area di 50 km con andamento E-W localizzata nell'angolo sud della Pianura Padana, interessando il settore centrale dell'arco di Ferrara appartenente al sistema esterno della cintura degli Appennini Settentrionali. L'arco di Ferrara è composto da due sistemi: le pieghe di Ferrara nel nordest e la piega di Mirandola localizzata nella parte più interna a sudovest [Govoni et al., 2014]. Abbiamo elaborato gli arrivi P ed S in modo da poter localizzare la sequenza sismica utilizzando differenti modelli di velocità trovati in letteratura: Bragato et al. [2011], Ciaccio and Chiarabba [2002],Costa et al. [1992], Iside, Zollo et al. [1995], Malagnini et al. [2012], Massa [2012] e quattro modelli geologici proposti da Lavecchia et al. [in prep.] L'idea è di produrre un insieme di localizzazioni di eventi clusterizzati con residui

minimi, in modo da poter capire quale è la faglia generatrice. Questo lavoro è stato svolto in collaborazione con l'Università di Chieti e il Dipartimento di Protezione Civile (DPC). Dalla distribuzione ipocentrale delle soluzioni, sembra che l'arco di Mirandola non sia coinvolto nella sequenza sismica, mentre i segmenti della parte interna e centrale del sistema di sovrascorrimento di Ferrara sembrano essere stati attivati dalle sequenze sismiche del 29 e del 20 Maggio, rispettivamente.

La complessità dell'area interessata dalla sequenza sismica dell'Emilia, richiede il calcolo di modelli tridimensionali di velocità in modo da poter localizzare più precisamente gli eventi. Come già detto, abbiamo elaborato una procedura iterativa: tomografia dei primi arrivi e localizzazioni 3-D degli eventi, attraverso l'uso rispettivamente del Cat3D e del NonLinLoc, in collaborazione con l'OGS. La sequenza sismica copre solo una piccola regione ($30x30\,km^2$ di larghezza e 20 km di profondità), per questo l'area investigata si limiterà alla porzione superiore della crosta. Come modelli iniziali di velocità abbiamo scelto: Costa et al. [1992]; Massa [2012] e NewModel1 [Lavecchia et al., in prep.], i quali avevano errori verticali inferiori al chilometro nello studio precedente. Il miglior modello iniziale sembra essere quello di Massa [2012], il quale mostra valori di rms bassi rispetti alle altre soluzioni. I tre modelli tridimensionali di velocità delle onde P risultanti mostrano caratteristiche comuni: uno strato superficiale a bassa velocità e uno strato spesso (5-20 km in profondità) a 5.5km/s. I risultati tomografici per i modelli Vs presentano un comune strato superficiale a bassa velocità e uno strato caratterizzato da valori di velocità per le onde S di 3.0 km/s.

Le tre serie di soluzioni, dei differenti modelli di velocità, sono comparabili all'interno dell'intervallo di errore, anche in termini di qualità. Le localizzazioni per la scossa principale del 20 maggio 2012 sono sparpagliate rispetto a quelle della seconda scossa principale del 29 maggio. Una possibile causa potrebbe essere l'installazione delle stazioni temporanee nel campo vicino della sequenza sismica dopo il 20 maggio 2012. Per l'evento del 29 maggio, infatti, si hanno molte più registrazioni che per il primo evento del 20 e tutte in campo vicino. Le localizzazioni degli eventi ottenute da modelli tomografici tridimensionali sono meno disperse di quelle ottenute con modelli unidimensionali, anche se le localizzazioni dei due eventi principali sono simili. In profondità le due serie di soluzioni non differiscono in modo significativo.

Per migliorare la qualità della procedura di localizzazione nel nostro centro di raccolta dati, vorremo installare una procedura automatica sia rapida sia precisa. Per raggiungere questo risultato abbiamo comparato l'AutoPicker con Antelope sulla sequenza sismica dell'Emilia. Questo confronto è di fondamentale importanza per comprendere quale dei due algoritmi

rileva fasi e/o localizza eventi in modo più preciso. Il nostro scopo, infatti, è quello di unire ed implementare queste due tecniche in modo da ottenere un miglior rilevatore di fasi e localizzatore. I risultati di questo confronto ci hanno portato a concludere che l'AutoPicker trova più fasi e con maggior precisione rispetto ad Antelope, sia per le fasi P che per le fasi S. Nonostante ciò il processo di associazione delle fasi in Antelope è in grado di correggere gli errori delle fasi e trovare la corretta localizzazione dell'evento. Questo ci ha suggerito di implementare l'algoritmo dell'AutoPicker nella procedura di Antelope, in modo tale che l' AutoPicker definisca gli arrivi P ed S e Antelope li associ e localizzi gli eventi.

Con il miglioramento delle reti sismiche e la possibilità di raccogliere enormi quantitativi di dati, è necessario produrre enormi database, in modo da poter avere un rapido accesso ad essi e di poterli rielaborare in tempo reale o quasi reale. Per questi enormi database la rilevazione manuale delle fasi è un lavoro oneroso, che richiede tanto tempo. La possibilità di avere uno strumento che rilevi automaticamente fasi di ottima qualità, che producano risultati similari a quelli ottenuti dall'inversione tomografica utilizzando le fasi rilevate manualmente, è sicuramente conveniente ed utile. Per questa ragione abbiamo confrontato due differenti tomografie dei primi arrivi, prodotte con la stessa tecnica dell'analisi precedente, che differiscono solo per i dati di partenza: la prima è stata ottenuta dalle fasi rilevate manualmente, la seconda dalle fasi rilevate automaticamente con l'AutoPicker per la sequenza sismica dell'Emilia. I risultati ottenuti indicano un incremento del valore medio dell' rms sia nelle localizzazioni sia nella tomografia per le fasi automatiche. Nonostante questo i modelli tridimensionali ottenuti (Vp, Vs and Vp/Vs) sono comparabili. Quindi per database contenenti enormi quantità di dati è possibile utilizzare le fasi automatiche come dati di partenza, ottenendo risultati comparabili a quelli ottenuti con le fasi manuali.

Introduction

Earthquakes constitute a recurring natural disasters all over the Italian territory, for that reason, civil defence focused interventions are extremely important. The rapidity of these interventions are correlated to the production of a fast and in real time locations of the seismic events. To identify the seismogenic faults, it is considerably important to have a precise location of event. For these two aspects, the upgrade of monitoring systems is fundamental to produce an improvement on the automatic locations quality in a quasi real time mode. The main purpose of this study is the production of accurate seismic event locations in real time. Earthquakes constitute a recurring natural disaster all over the Italian territory, and therefore civil defence focused interventions are extremely important. The rapidity of such interventions strongly depend on the production of fast and possibly real-time locations of the seismic events. The precise location of events is also needed to identify seismogenic faults. For these two aspects, an upgrade of the existing monitoring systems is fundamental to improve the automatic locations quality in a quasi real-time mode. The main purpose of this study is the production of a routine that will accurately locate seismic event in real-time.

The quality of the locations strongly depends on the correct determination of the P- and S- phases. Sometimes it is hard to recognize the correct onset of a phase, since the signal can be blurred by various causes, such as, e.g., the complexity of the generating fault mechanism and the presence of natural or man-made noise. For this reason we have studied, analyzed and compared different phase picking and location methods. The picking algorithms that were evaluated are the Short Time Average over Long Time Average ratio (STA/LTA) and the Akaike Information Criterion (AIC) function. The first one is a common technique used to distinguish the seismic signal from noise. It is based on the continuous calculation of the average values of the absolute amplitude of a seismic signal in two moving-time windows with different lengths: the short-time average and the long-time average. The STA/LTA ratio is compared with a threshold value. When the ratio is larger than this threshold, the onset of a seismic signal is detected. The main disadvantage of

this method is its instability, due to the parameters choice: a too long STA window could cause the non-detection of local events, whereas a too short STA window could cause the detection of man-made seismic noise. A high STA/LTA threshold records less events than the ones those have occurred, but false triggers are eliminated. If this value is chosen to be lower, more events will be detected, but more frequent false triggers could be recorded. This algorithm is part of the Antelope (BRTT, Boulder) detection procedure, used in this study.

The AIC function is a precise and sophisticated methodology, being a revision of the classical maximum likelihood estimation procedure [Akaike and Hirotugu, 1974]. The AIC function is designed for statistical identification of model characteristics. Its most classical application consists in the selection of the best among several competing models; the maximum likelihood estimate of the model parameters gives the minimum of AIC function. It is strictly correlated to the correct choice of the time window in which apply the function, so it is necessary combined with other techniques, in order to automatically choose a correct window. This dependence on other methods, makes the application of the AIC function to detect phases, a complex methodology, which can be affected by errors in the parameter choices. The AIC function is used in the AutoPicker procedure [Turino et al., 2010]. In a seismic signal the minimum of the AIC function identifies the P- or S- onset. In this automatic phase picker the time window in which to apply the function, in the case of P phases, is chosen by a combination of a band-pass filter and an envelope time function, used as energy detector to select the event in the waveform; for the S phases, the selection of the window is guided by a preliminary location of the P- phases. Once the P- and S- phases are identified, it is necessary to elaborate them in order to locate the seismic event.

In Antelope the location procedure is called orbassoc. This methodology reads the pickings, determined through the use of the STA/LTA technique, and tries to produce an event location over three possible grids: teleseismic, regional and local. The solution that produces the minimum travel time residuals set (differences between synthetic travel times and observed travel times) is considered as the best one. In the AutoPicker the location algorithm is Hypoellipse [Lahr, 1979], in which the travel-times are estimated from a horizontally-layered velocity-structure and the hypocenter is calculated using Geiger's method [Geiger, 1912] to minimize the root mean square (rms) of the travel time residuals. In order to test the performances of the AutoPicker, we have applied it to a database of 250 events recorded in the year 2011 by the C3ERN - the Central Eastern European Earthquake Reasearch Network [Department of Mathematics and Geosciences (DMG), Istituto Nazionale

di Oceanografia e di Geofisica Sperimentale (OGS), Agencija RS za okolje (ARSO) and Zentralanstalt fr Meteorologie und Geodynamik (ZAMG)] at the Alps-Dinarides contact. In order to improve the location quality we have used in this work various location methodologies with respect to the absolute ones, such as Hypoellipse. The HypoDD [Waldhauser and Ellsworth, 2000] is a relative algorithm, the locations depend either on the location of a master event or on a station site. This method can be applied only in the case when the hypocentral separation between two earthquakes is small compared to the event-station distance and the scale length of the velocity heterogeneities. In such cases the ray paths between the source region and a common station are similar along almost the entire ray path.

The complexity of the tectonic environment influences ray tracing and consequently the event locations. In regions where many seismogenic structures are present, a precise location of a seismic sequence is essential, in order to understand which fault is the generating one. In such cases the use of a 1-D velocity model might not be sufficient, so a 3-D velocity model is a better solution to describe the studied area. The travel-time tomography is a common technique to obtain a 3-D velocity model, from event locations. In this study we have chosen a local earthquake tomography (LET) [Aki, 1982]. The LET goal is to improve the model parameters, by perturbing them in order to minimize some measure of the misfit to the data. Compared with the teleseismic tomography (which uses as input teleseismic events characterized by a huge station-event distance), the LET offers a much higher spatial resolution of the structure, due to increased ray density sampling, higher wave frequency and closer station spacing. On the other hand, the thickness of the retrieved velocity model is constrained by the maximum earthquake focal depths in the area, whereas the thickness of models retrieved by teleseismic tomography can be of the order of the array dimensions. The travel time tomography and the 3-D event location are performed, respectively, using the Computer Aided Tomography for 3D models (Cat3D) software [Cat3D user manual, 2008] and the Non Linear Location (NonLinLoc) software [Lomax et al., 2000] through an iterative procedure. The Cat3D is basically used in active seismics, but in this study it is applied to a seismological case. The main difference between active seismics and seismology are the unknowns in the tomographic system. In seismology the source location is an unknown parameter with a high uncertainty, while in active seismics the source locations are well defined. In this study, the introduction of the source location in the tomographic system, introduces uncertainties in obth the ray tracing and travel-times estimation. In order to solve this uncertainty, we used an iterative procedure composed by the application of tomography and the event location in resulting 3-D velocity model. In the Cat3D software,

in order to estimate the velocity field (inversion of arrivals time), we use the SimuItaneous Reconstruction Technique (SIRT) algorithm. The velocity of each pixel is upgraded at each iteration, considering all the rays, as the average of the single values of velocity calculated for each ray passing through this pixel. The NonLinLoc technique is used to locate the events using the 3-D velocity model resulting from the tomographic inversion.

After the occurrence of the Emilia seismic sequence in May-June 2012, we have decided to investigate it as an interesting study case. The May-June 2012 Emilia seismic sequence affected a 50-km wide roughly E-W trending region located at the southern edge of the Po river alluvial plain. The sequence started on May 20 (02:03:53 UTC), with a M_L 5.9 earthquake, preceded by a $M_L \geq 4.1$ foreshock, three hours earlier [Scognamiglio et al., 2012]. The aftershock sequence comprised thousands of earthquakes, six of them with $M_L \geq 5.0$. Among these, a M_L 5.8 earthquake, on May 29 (07:00:03 UTC), caused probably more damages than the first shock. Through the study of this seismic sequence we have tested the performances of the automatic picking algorithms. In order to do that, we have manually picked and located some of the major events of this seismic sequence. These events are characterized by P- and especially S-phases, which are really difficult to detect, probably because the fault system of the Emilia earthquake area is complex. Moreover, the complexity of the tectonic environment along with the focal depth uncertainty make the event locations problematic, because it is not always easy to assess which fault has moved. The Emilia sequence occurred in the central, roughly E-W trending, sector of the Ferrara arc belonging to the external fold-and-thrust system of the Northern Apennines belt. The Ferrara arc is structured into two major fold-and-thrust systems: the Ferrara system in the northeast and the Mirandola system located in a more internal position to the southwest [Govoni et al., 2014]. We have processed the P- and S- onsets in order to locate the seismic sequence using different velocity models found in literature: Bragato et al. [2011], Ciaccio and Chiarabba [2002],Costa et al. [1992], Iside, Zollo et al. [1995], Malagnini et al. [2012], Massa [2012] and four geological models proposed by Lavecchia et al. [in prep.]. The idea is to produce a set of clustered event locations with the lowest residuals, in order to understand which is the generating fault in the complex system of faults. This work is being performed in collaboration with Universit di Chieti and Department of Civil Defence (DPC).

The complexity of the seismic sequence area in Emilia requires the calculation of a tridimensional velocity model in order to locate more precisely the events. As already said, we elaborated an iterative procedure: travel-time tomography and 3-D event locations, through the use of the Cat3D and NonLinLoc softwares, in collaboration with OGS. This is done to minimize the

uncertainties introduced in the tomographic system by the unknown source locations. Since the seismic sequence covers only a small part of this region (about $30 \times 30\,km^2$ wide and $0 - 20\,km$ deep), the investigated area will be limited to its upper crustal part.

To improve the quality of the location procedure in our datacenter, we would like to install a precise and rapid automatic procedure. Therefore, we have compared the AutoPicker method with a more tested and solid one, the Antelope picking method, on the Emilia seismic sequence of data, using as reference pickings and locations the manual ones. This comparison is of fundamental importance which one of the two algorithms better detects phases and/or locates events. Our aim is, in fact, to merge and implement these two techniques to obtain a better detector and locator.

With the improvement of seismic networks and the possibility to store huge amounts of data, it is necessary to produce big databases, in order to have a rapid access to the data and to re-elaborate them in real time o quasi real time mode. For big databases, the manual picking is an onerous work, requiring a lot of time. The possibility to have a good-quality automatic tool for phase recognition and picking, which produces similar results to those obtained from the tomographic inversion by using manual phases picking, is certainly convenient and useful. For this reason, we have compared two different travel time tomographic inversions made with the same technique of the previous analysis, differing only in the input phase files: the first one obtained from manual pickings, the second one from the automatic AutoPicker pickings of the Emilia sequence. This test is done to analyze and compare the different results in terms of locations and velocity models, in order to study how much the location errors influence the tomography errors and to understand if automatic phases could be used as input in a travel- time tomography obtaining similar results as those obtained using manually picked phases.

Chapter 1

Picking and Location Methodologies

In this work we have studied, analyzed and compared different methods of picking and location.

The picking algorithms, that we have evaluated, are the STA/LTA and the AIC function. The first one is a common technique, which is based on the continuos calculation of the average values of the absolute amplitude of a seismical signal in two consecutive moving-time windows: the Short Time Average and the Long Time Average (see section 1.1). The main disadvantage of this method is the instability and it is not so unusual to detect 'ghost' events or to miss a real one. On the other hand the AIC function is a more precise and sophisticated methodology, but it is strictly correlated to the right choice of the time window in which apply the function (see section 1.2), so it is necessary combined with other techniques, in order to automatically choose a correct time window. This dependence of other methods, makes the application of AIC function to detect phases, a complex methodology, which can be affected by errors in the parameter choices.

In this chapter we introduce also different techniques, able to locate events, in detail: Hypoellipse [Lahr, 1979], HypoDD [Waldhauser and Ellsworth, 2000], AutoPicker [Turino et al., 2010] and Antelope written by BRTT, Boulder Real Time Technologies. Hypoellipse (section 1.3) and HypoDD (section 1.4) are two different methodologies, one is absolute and one is relative respectively, but both of them are used only to locate seismic events. Otherwise the AutoPicker (section 1.5) and Antelope (section 1.6) are combined techniques, which are able to detect phases and to locate events, using different algorithms from each other.

1.1 STA/LTA algorithm

A waveform is basically noise or signal plus noise. A signal is noticeable from the noise because the variance of the time series increased when a signal is present.
It is possible to assume that firstly the recorded time series are independent measurements of a zero-mean Gaussian random variable, and also that the fact that the recording is noise can be tested by measuring the power within a time window. If this power exceeds a threshold value, then the recording is signal plus noise. This threshold value can not be calculated precisely, but it is possible to approximate this detector in seismology, using the STA/LTA algorithm. This consists on the estimation of the power over a long time interval (LTA), and over a short time interval (STA). Then the ratio STA/LTA, which is usually called signal-to-noise ratio (SNR), is compared with a threshold value. If the SNR is larger than this threshold, the recording is a detected seismic signal. The estimation of the short time average STA of a seismic trace w(t), is:

$$STA(t) = \frac{1}{L} \cdot \sum (w(t-j)) \tag{1.1}$$

with

$$L = samplingrate \cdot STAlenght$$

the recursive definition of the long time average LTA is:

$$LTA(t) = 2^{-\zeta} \cdot STA(t-\epsilon)t(1-2^{-\zeta}) \cdot LTA(t-1) \tag{1.2}$$

where ϵ is a time delay, and ζ is a steering parameter for the LTA update rate.

The signal-to-noise ratio (SNR) is defined as:

$$SNR(t) = \frac{STA(t)}{LTA(t)} \tag{1.3}$$

The STA/LTA algorithm parameters are:

1. STA window duration
2. LTA window duration
3. STA/LTA trigger threshold level
4. STA/LTA detrigger threshold level.

The STA window duration influences the capturing of distant or local events. If the STA window is shorter, the trigger's sensitivity becomes higher to local events; on the other hand if the STA window duration is longer, the most sensitive is the trigger for distant earthquakes. However it is necessary to point out that the STA duration is also important to prevent false triggers. If the STA windows is too short, the triggering becomes more sensitive to spyke-type of man-made seismic noise.

The LTA window duration of 60 seconds is a common initial value. A LTA value shorter than the common one, is able to exclude the emergent regional events from triggering or man-made seismic noise. A LTA value longer than 60 seconds can be use to detect distant regional events.

The STA/LTA trigger threshold level establishs which event will be detected and which not. If this value is higher, it is possible to record less events than the ones happened, but the false trigger are eliminated. If this value is chosen as lower, more events will be detected, but more frequent false triggers could be recorded.

The STA/LTA detrigger threshold value is useful to record or not the coda waves (if the value is low, the coda waves are recorded; if this one is high, viceversa) and to eliminate the noise of the some seismic site (if the value is high, it is possible to exclude the noise; if is low, viceversa).

A good working of a trigger algorithm does not depend only on these four parameters, previously described, but also on the choice of the trigger filter, the pre-event time and the post-event time.

In Figure 1.1 and Figure 1.2 we present two examples of the parameter choice in the case of local events for the STA/LTA algorithm. We choose to analyze the correct set of parameters for a local event, because in this study we are trying to compare two different automatic algoritm applied in a local network, so we are interested on the good locations of local events. In the first case, (Figure 1.1) we analyze a seismogram collected for a local event occurred in 2011 from a very close station to the epicenter. We have filtered this waveform with a bandpass Butterworth filter from 1 to 8 Hz, chosen after several tests. The STA window length is the window in time (0.3 s in this case), in which sample by sample it is calculated the short time average; for the LTA, long time average we have chosen 20.0 seconds. In the third image the yellow line is the short time average and the red line is the long time average for this signal. In the last box the yellow line is the signal to noise ratio and the red line is the threshold value that we have chosen, as 4.0. The detections are the samples which pass over the threshold line. In this case there are two detections.

In the second example (Figure 1.2) we analyze the same event but from a station far from the epicenter. We have used the same parameter of the

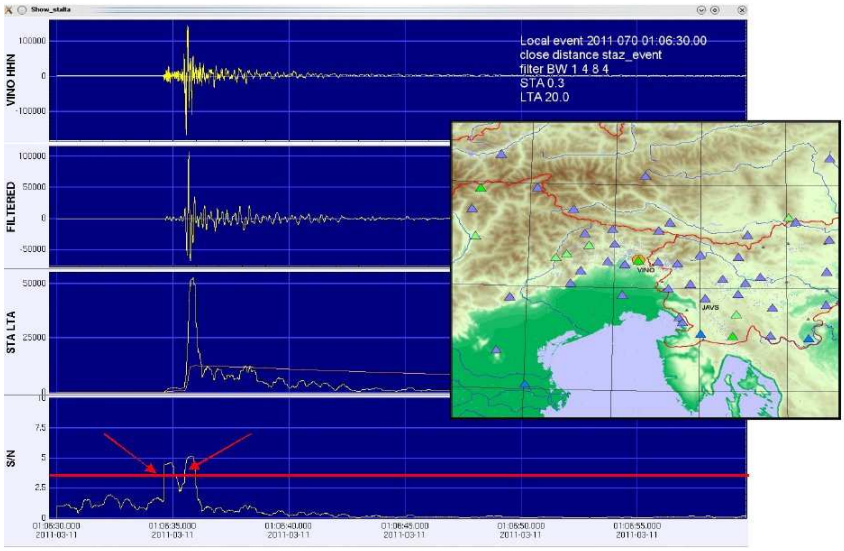

Figure 1.1: Waveform registered for a local event in a very close station to the epicenter of it. First it is the seismogram, then filtered with a Butterworth filter from 1 to 8 Hz. Then there is the Short Time average(yellow line) with the Long Time Average (red thin line). Finally there is the Signal Noise Ratio (yellow thin line) and the theshold value (red line) of 4, in this case. The detections are the samples whose have the SNR upper than the threshold value. In this case are two detected phases indicated by the red arrows. On the right it is possible to see how much are closest the station VINO examined in this example (green triangle) and the epicenter (red circle).

previous case in order to demonstrate that these parameters are reliable to detect a local event. In fact it is clear from the last image that the signal to noise ratio exceeded the threshold value (the red line) in two samples, which are two good phases. So the parameters chosen for the STA/LTA algorithm, the two window length (sta and lta window length), the filter and the threshold value are a good match for a local event.

1.2 AIC function

The Akaike Information Criterion (AIC) function is a revision of the the classical maximum likelihood estimation procedure [Akaike and Hirotugu, 1974]. The AIC function is designed for statistical identification. The most classical application of the AIC, is when there are several competing models and the maximum likelihood estimates of the parameters gives the minimum

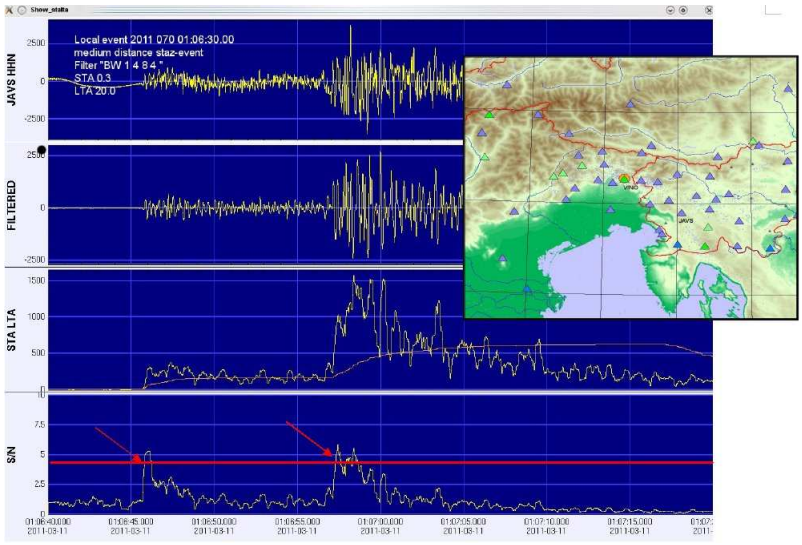

Figure 1.2: Waveform registered for a local event from a station not so close to the epicenter. First it is the seismogram, then filtered with a Butterworth filter from 1 to 8 Hz. Then there is the Short Time Average (yellow line) with the Long Time Average (red thin line). Finally there is the Signal Noise Ratio (yellow thin line) and the theshold value (red line) of 4, in this case. The detections are the samples whose have the SNR upper than the threshold value. In this case are two detected phases, indicated by two red arrows. On the right it is possible to see how much far are the station JAVS examined in this example (green triangle) and the epicenter (red circle).

of AIC. In seismology, for a seismogram x of length N, the AIC function is:

$$AIC(k) = k \log var(x[1,k]) + (Nk - 1) \cdot \log var(x[k+1,N]) \qquad (1.4)$$

where k ranges through all the seismogram samples.

It should be pointed out here that only the global minimum of the AIC function is related to the arrival time of the detected phase in the AIC phase picker. For this reason, we need to guide the work of the AIC picker by choosing a time window that includes only the seismogram segment of interest. So it is necessay to combine this technique, with others in order to detect phases. If the time window is chosen properly, the AIC picker is likely to find the P and S -wave arrival accurately [Zhang et al., 2003]. For a seismogram with a very clear onset, AIC values have a very clear global minimum that corresponds to the wave arrival. When there is more noise than signal in the seismogram, the global minimum cannot be guaranteed to indicate the wave arrival. Here, there are three examples of the AIC function application (1.3).

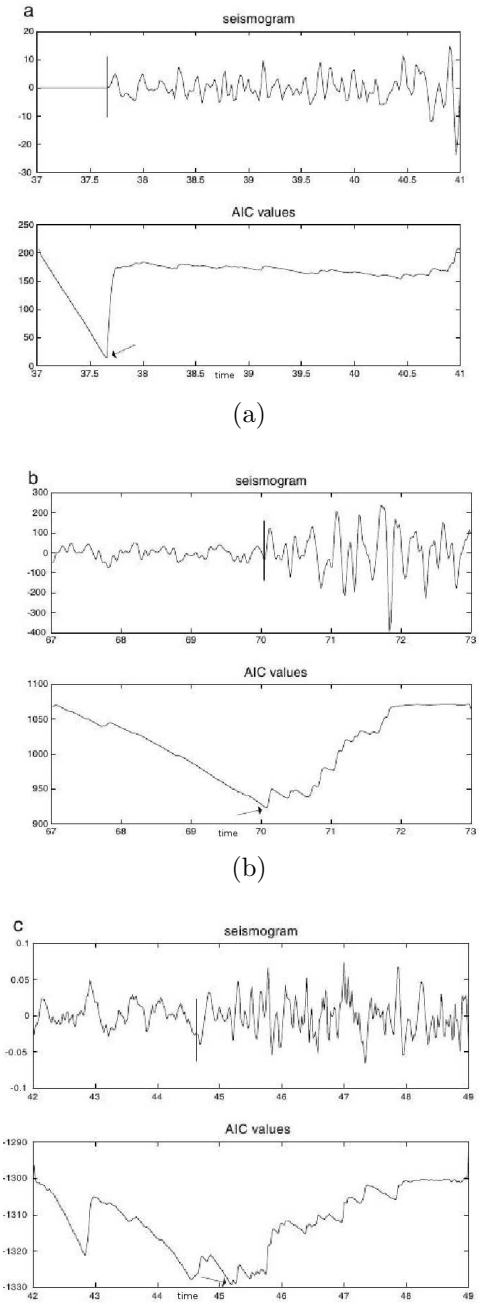

Figure 1.3: Seismograms and their corresponding AIC values. (a) For a seismogram with a very clear P-wave arrival (indicated by a thick line), the AIC value is a very clear minimum point (indicated by an arrow). (b) For a seismogram with a rather clear P-wave arrival but with relatively lower S/N ratio, the AIC function has many local minima, whereas the global minimum (arrow) still corresponds to the P-wave onset. (c) For a very low S/N seismogram, there are a few local minima close to each other. In this case, the global minimum (arrow) cannot be guaranteed to be the P-wave arrival [Zhang et al., 2003].

1.3 Hypoellipse

Hypoellipse is a software, used for determining the hypocenters of local or near regional earthquakes. The program was originally developed on the Lawrence Berkeley Laboratory computer [Lahr, 1979]. Travel-times are determined from a horizontally-layered velocity-structure, or a linear increase of velocity with depth, or a linear increase of velocity over a half-space, or a previously generated travel-time table. In the solutions can be used arrival times for the first arrival of P waves and S waves, and S-minus-P interval times. Each arrival can be weighted according to the reading clarity, the epicentral distance to the station, and the deviation of its residual from the mean. The hypocenter is calculated using Geiger's method [Geiger, 1912] to minimize the root-mean-square (RMS) of the travel-time residuals.

1.3.1 Geiger's method

Geiger [1910, 1912] introduced an iterative least-squares technique for earthquake location. The earthquake location problem is highly non-linear in the sense that there is no simple linear relationship between the observed arrival times and the desired spatial and temporal coordinates of the source. This non-linearity arises from the determination of the distances and azimuths for the source to each observation and also from the model predicted travel-time as a function of distance and depth. One approach is to linearize the problem, by focusing on slight changes in the source coordinates. To simplify the presentation, we will consider a local earthquake problem, for which a cartesian coordinate system is used.

Let the coordinates of the earthquake be (X, Y, Z, T), where X,Y and Z are the spatial coordinates and T is the origin time. Let the coordinate of the kth station be $(x_k, y_k, 0)$, where we assume the station is at the surface. The corresponding observed arrival time is tobs . For the given spatial coordinates, the residual, that is the difference between the observed and predicted arrival time for an event j and a station k, is defined as:

$$r_k^i = (t^{obs} - t^{cal})_k^i \tag{1.5}$$

where

$$t^{cal} = T - TT(x_k, y_k, 0, X, Y, Z)$$

where TT is the predicted travel-time as a function of the particular phase and the station and hypocenter coordinates. The linearization of this problem starts with the assumption that the residual is due to an incorrect location (X_0, Y_0, Z_0, T_0), where, the index 0 indicates the initial value. If we wish to

predict the travel-time for a new location, $(X_0 + \Delta X, Y_0 + \Delta Y, Z_0 + \Delta Z, T_0 + \Delta T)$, the estimated predicted arrival time is:

$$T_0 + \Delta T + TT(x_k, y_k, 0, X, Y, Z) + \frac{\partial TT_k}{\partial X}\Delta X + \frac{\partial TT_k}{\partial Y}\Delta Y + \frac{\partial TT_k}{\partial Z}\Delta Z \quad (1.6)$$

where the partial derivatives are evaluated at the current coordinates (X_0, Y_0, Z_0). So the residual becomes:

$$r_k^j = \Delta T + \frac{\partial TT_k}{\partial X}\Delta X + \frac{\partial TT_k}{\partial Y}\Delta Y + \frac{\partial TT_k}{\partial Z}\Delta Z \quad (1.7)$$

One way to approach this problem is to select the changes such that the minimize the following expression (hence least squares):

$$R = \sum r_k^{j^2} = Ax \quad (1.8)$$

The conditions to force this to be a minimum are:

$$\frac{\partial R}{\partial \Delta T} = 0; \frac{\partial R}{\partial \Delta X} = 0; \frac{\partial R}{\partial \Delta Y} = 0; \frac{\partial R}{\partial \Delta Z} = 0; \quad (1.9)$$

in a matrix language, resolving the R = Ax, we obtain:

$$A^T Ax = A^T R, \quad (1.10)$$

$$x = (A^T A)^{-1} A^T R \quad (1.11)$$

The solution x of the system of linear equations provides the change in source coordinate in an iterative way, which continues until the changes are less than a predifined amount to define convergence.

1.4 HypoDD

The HypoDD technique developed by Waldhauser and Ellsworth [2000], is a relative location method. Basically it differs from the absolute hypocenter location methods, as Hypoellipse (section 1.3), from the fact that the locations depend or on the location of a master event or on a station site.

This method could be applicated only in the case that the hypocentral separation between two earthquakes is small compared to the event-station distance and the scale length of the velocity heterogeneity, then the ray paths between the source region and a common station are similar along almost the entire ray path. In this case, the difference in travel times for two events observed at one station can be attributed to the spatial offset between the events with high accuracy.

So the HypoDD technique combine P- and S-wave differential travel times derived from cross-spectral methods with travel-time differences and minimize residual differences (or double differences) for pairs of earthquakes by adjusting the vector difference between their hypocenters. Thus we are able to determine inter-event distances between correlated events that form a single multiplet to the accuracy of the cross-correlation data while simultaneously determining the relative locations of other multiplets and uncorrelated events to the accuracy of the absolute travel-time data, without the use of station corrections.

1.4.1 HypoDD technique

In Section 1.3 the residuals are defined as:

$$r_k^i = (t^{obs} - t^{cal})_k^i \tag{1.12}$$

Now we have to define the differences between residuals of the events i and j at the station k:

$$dr_k^{ij} = (t_k^i - t_k^j)^{obs} - (t_k^i - t_k^j)^{cal} \tag{1.13}$$

We define dr_k^{ij} as the double-difference. Note that it may use either phases with measured arrival times where the observables are absolute travel times, t, or cross-correlation relative travel-time differences.

1.5 AutoPicker

The AutoPicker is an automatic phase picker for local earthquake based on Turino et al. [2010], which include envelope calculation, AIC detector, checking for inpulsive arrivals, definition of expected S window (a priori information) on the basis of preliminary location derived from P arrival times and quality assessment.

1.5.1 AIC detector

Seismic phases onsets are generally characterized by a rapid change in amplitude and/or the arrival of high-frequency energy. Assuming that the seismogram can be divided into locally stationary segments as an autoregressive (AR) process and the intervals before and after the onset are two different stationary processes [Sleeman and Van Eck, 1999] the autoregressive-Akaike information criteria (AR-AIC) method can been used to detect P and S arrival times [Sleeman and Van Eck, 1999, Leonard and Kennett, 1999, Leonard, 2000].

The AutoPicker is an improved automatic phase picker for local earthquake. The advantage of this technique is that it provides consistent arrival time picks for P and S wave and provide reliable automatic earthquake location.

The AIC picker used in this study is based on Maeda [1985] which proposed another method different from the former AR-AIC algorithm, in which the AIC function (see section 1.2) is obtained directly from the waveform data, instead of the AR coefficients.

As we have previously described on section 1.2, the AIC requires the combination of other techniques in order to determine the correct time window, in which calculate the AIC function. So, here, we described the AutoPicker procedure, which includes the AIC detector, is summarized in figure 1.4. The P onsets are calculated as follows:

1. The envelope function is calculated after an appropriate bandpass filter has been applied to the vertical component of the ground motion. The envelope function is used as energy detector to choose an appropriate window for the AIC picker; the minima of the AIC function is considered the onset time (Paic).

2. For signals with low S/N ratio the global minima of the AIC calculated from the filtered vertical component of the seismogram shows few local minima, but the global minimum still indicates accurately the P-wave onset. This algorithm separates weak emergent arrivals (Figure 1.5) from impulsive ones (Figure 1.6) and corrects for impulsive. An arrival is considered impulsive when the average SNR, in an appropriate frequency band, exceeds a threshold value. The procedure developed to adjust P_{aic} for strong impulsive arrivals, is based on a time window of a given length which is moved, starting from P_{aic}, up and down the trace, sample by sample, and calculate at each location the ratio between the variance of the unfiltered signal before that location and the variance of the unfiltered signal before that location. The sample which maximize the ratio of variances is considered the P_{sample}.

3. Quality assessment of P_{aic} or P_{sample}: on the basis of SNR, Fmin is defined as the smallest frequency in a chosen frequency band for which the SNR is higher than a threshold value; in the same way, Fmax is defined as the greatest frequency in another frequency band for which the SNR is higher than threshold value. If Fmin or Fmax cannot be estimated, the waveform is rejected.

The S onsets are calculated as follows:

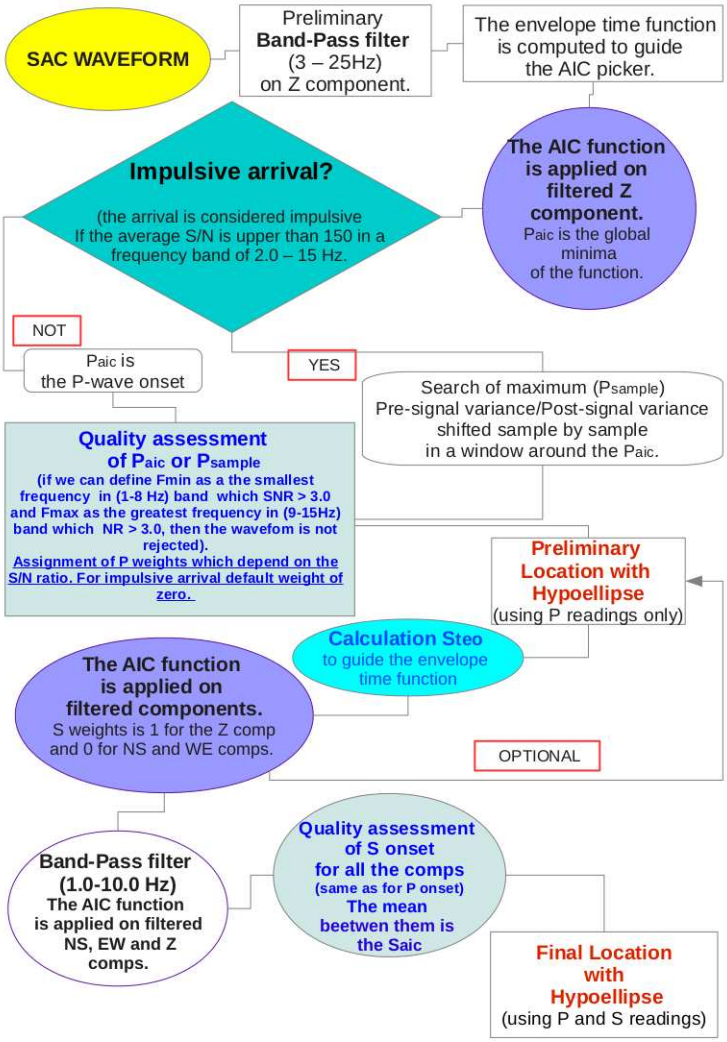

Figure 1.4: Flow chart of the AutoPicker P and S wave picking approach.

1. A preliminary location based on the P readings is computed using the Hypoellipse code (see section 1.3); predicted S-arrival time S_{teo} are also calculated (theoretical arrival time in an appropriate regional velocity model, usually one-dimensional P-wave velocities divided by a constant V_P/V_S ratio).

2. S_{teo} is used to guide the envelope time function, which, as for the P phases, is used as energy detector to choose an appropriate window for the AIC function; S onsets are estimated for horizontal (weight

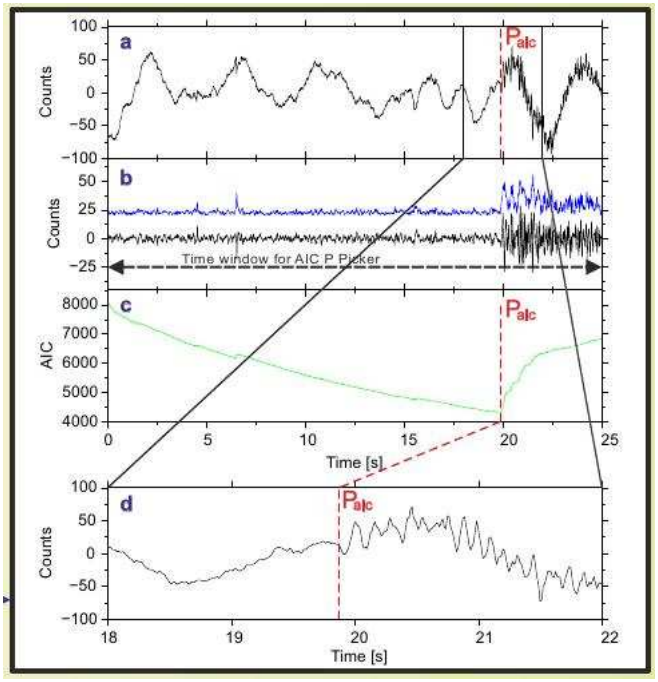

Figure 1.5: Example of P AIC picker applied to a low SNR vertical component; (a) unfiltered seismogram; (b) bandpass filtered seismogram and corresponding envelope function; (c) correspondig AIC function; (d)detailed view of the P onset.

0, the most significant) and vertical (weight 1, less significance than 0) components after an appropriate bandpass filter has been applied (Figure 1.7).

3. Quality assessment (same as for P onset) of S onset for all the components. The mean between them is considered the S-arrival time S_{aic};

4. Final location is computed using the Hypoellipse code (section 1.3).

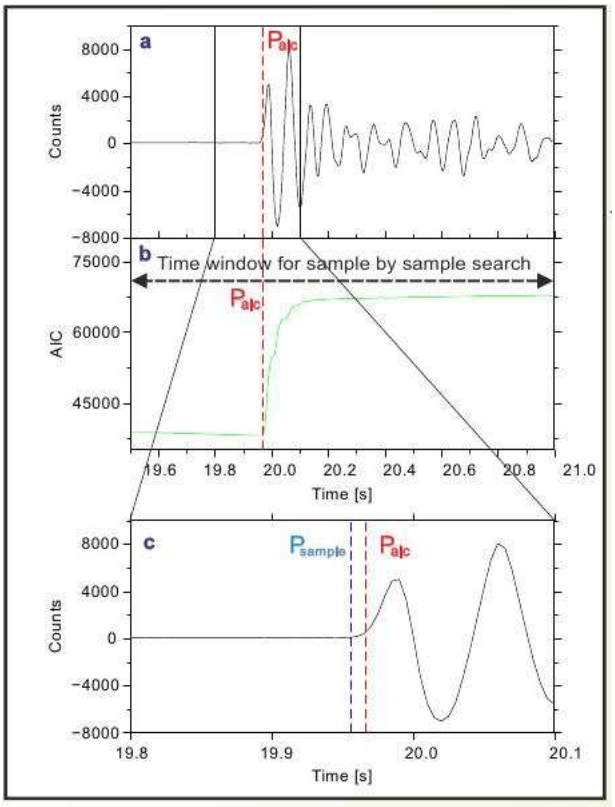

Figure 1.6: Example of P AIC picker applied to a low SNR vertical component; (a) unfiltered seismogram; (b) bandpass filtered seismogram and corresponding envelope function; (c) correspondig AIC function; (d)detailed view of the P onset.

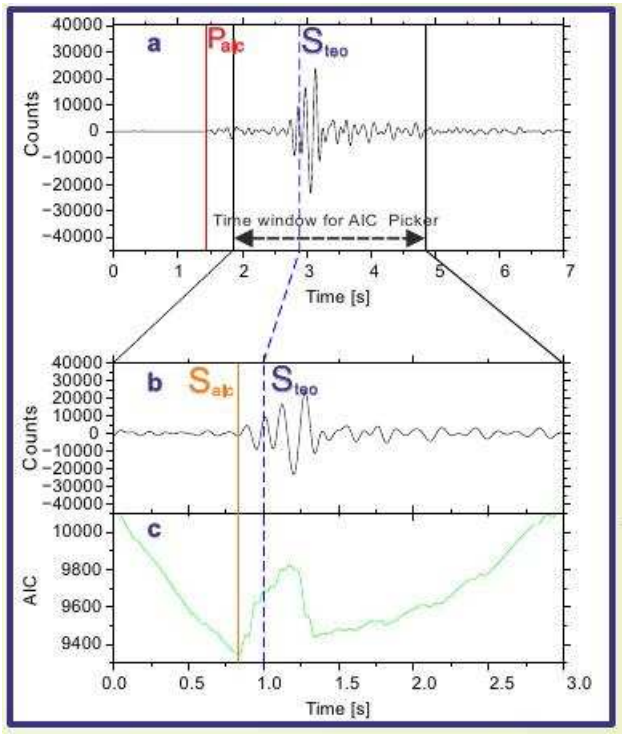

Figure 1.7: Example of S AIC picker applied to NS component; (a) unfiltered seismogram; (b) band pass filtered seismogram; (d) correspondig AIC function.

1.6 Antelope

Antelope is an integrated collection of programs for data collection and seismic data analysis written by BRTT, Boulder Real Time Technologies. In particular for the seismic data picking, Antelope uses the STA/LTA algorithm, well described in paragraph 1.1. Here in this paragraph we described, how the Antelope locator works in a quasi real-time mode (Figure 1.8): The loca-

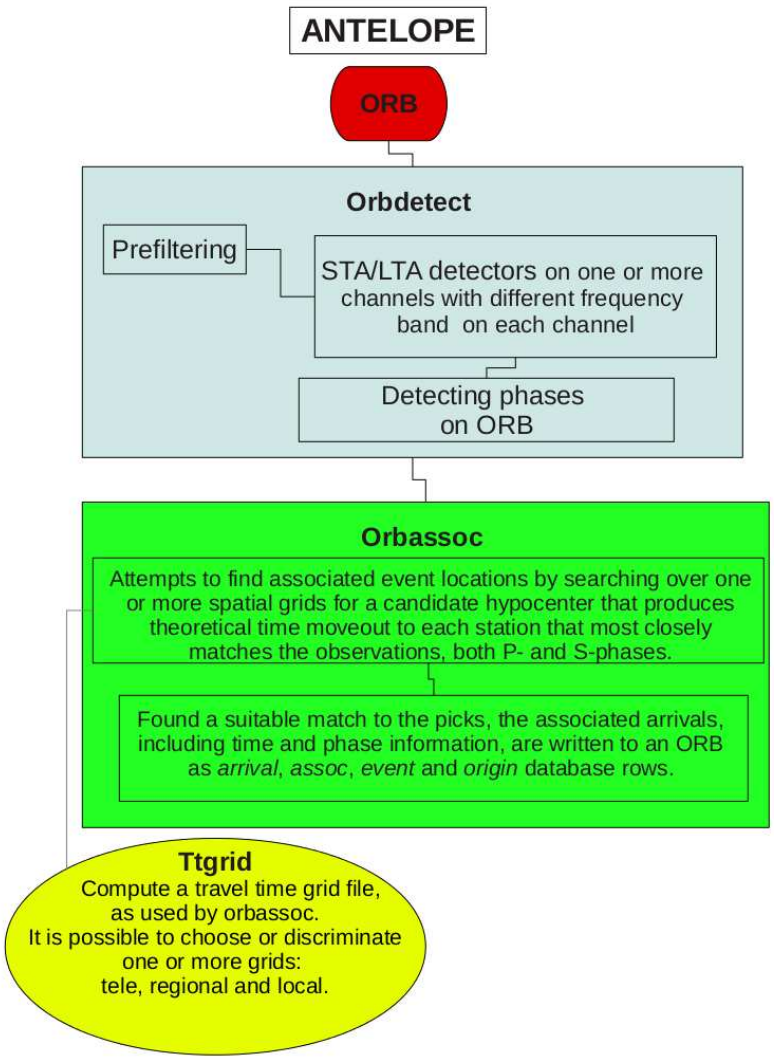

Figure 1.8: Flow chart of the Antelope P and S wave picking and event location approach.

tor procedure, in Antelope, is called orbassoc. This methodology reads the pickings, determined through the use of the STA/LTA technique (described in the paragraph 1.1) and tries to associate them into an event location, over the three possible grid: tele, regional and local. The solution, which produces the minimum time residuals set, is considered as the best one. This process, from the picks reading to the best location, is done recursively. Each time an event is found, its associated picks plus all other picks, that fall close to the predicted arrival times, are removed from the list and the remaining picks are reprocessed. This is done until no more events can be extracted.

This procedure, in seeming simple, is characterized by a lot of parameters. Here, we describe the most important and characteristic.

The *process_time_window* represents the time window in seconds that will be used to catch the arrival picks, detected with the STA/LTA procedure. This value should correspond to the total phase moveout time difference between the closest grid node and the furthest one. This number should be set no larger than several minutes for most *local/regional* networks, in this study the chosen value is 350.0*sec*. The *process_ncycle* specifies how often the running pick list is processed through the grid searches, as a number of picks, 50.0 in this work. If this value is too low, the internal pick list will be grid processed often at the expense of computer resources. If it is too high, the internal pick list will be grid processed infrequently resulting a higher time latency in determining an event. The *process_tcycle* is set to 20.0 sec, and determines how often the running internal pick list is processed through the grid searches, as a time increment in seconds. If *process_tcycle* is set to 0.0, then this method of triggering the pick list processing is disabled. The *process_timeout* is a timeout clock in seconds, in this study 30 seconds and it is necessary to force grid processing of the internal pick list as long as any picks have been added to the list. If it is 0, this function is disabled. The *trigger_number_stations* (5) are the minimum number of stations with detection pick times within *trigger_time_window* (20 sec) seconds that will initiate immediate pick list processing.

It is possible to define different sets of parameters for the three possible grids: tele, regional and local. The most significant are described above.

The *nsta_thresh* is the minimum number of stations that have triggered the event. Obviously the number of station depends on the distance of the hypothetical epicenter. The three option: *try_S*, *associate_S* and *reprocess_S* are strictly correlated each other. The option *try_S* indicates if the associator has to consider both P and S observations or only P. After that Antelope calculates a possibile time window in which finds the S-phases and associates them, if *associate_S* is set to yes. Then the associator makes the final location with P- and S- phases, if *reprocess_S* is activated. It is also possible

to choose which phases used for the location with the $phase\_sifter$ option, and in which channel detect P and in which detect S phases, with the P channel sifter and S channel sifter. With the priority number it is possible to indicate a favourite grid. The option relocate is really important, because through the use of it, it is possible to choose a relocation scripts to refine the final solution. In our study we choose to relocate the desire solution with the genloc package, in the Antelope software.

The dbgenloc collection of parameters is the interface for the use of the GENeralized LOCation (GENLOC) library [Pavlis et al., 2004], which implements the Gauss-Newton method used for single event locations, proposed by Geiger [1910] and described in the paragraph 1.3. For the grid determination it is possible to choose between different approaches; the most stable is to derive the origin time from the earliest arrival time recorded by the data, t_1^k, and set the origin time estimate as

$$\widehat{\tau} = t_1^k - T_{model}^k(r_1, \widehat{x}) \tag{1.14}$$

where r_1 is the location of the station with t_1^k, and $\widehat{x}$ is a trial hypocenter in the grid. The location estimate returned by the grid with the smallest misfit. This is an useful interface because the algorithm does not need informations about the geometry of the grid being searched; it only searches for the minimum from the list of trial values.

Chapter 2

The Emilia sequence of May-June 2012

In this chapter we examine the Emilia seismic sequence occured in Maj-June 2012 as an interesting case of study. Through the study of this seismic sequence, we have tested the performances of automatic picking algorithms in chapter (4). In order to do that, we have manually picked and locate some of the major events of this seismic sequence. These events are really complex to locate, because the fault system of the Emilia earthquake area is complex and it is not easy to assess which fault has moved. As it is possible to see from the Figure 2.1 many structures are present in the area of interest, so a precise localization of the sequence is essential, in order to understand which one of faults are the generating one. For that reason it is hard to recognize the P- and in particular the S- pickings. These ones, the S-onsets are really important to determine the depths of the events, and in this case of a complex fault system it is fundamental to know the depth with the highest precision. To obtain this result, we have processed the P- and S- onsets using different velocity models found in literature: Bragato et al. [2011], Ciaccio and Chiarabba [2002],Costa et al. [1992], Iside, Zollo et al. [1995], Malagnini et al. [2012], Massa [2012] and four geological models proposed by Lavecchia et al. [in prep.] (Figure 2.3). The idea is to find a velocity model which produces the solutions with the lowest residuals and which produces the locations which better fit the fault profiles. This work is being performed in collaboration with Universit di Chieti and DPC.

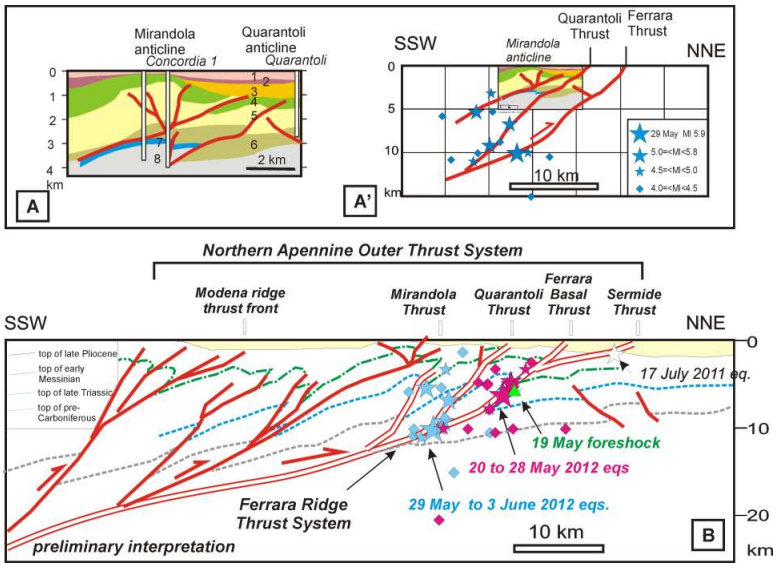

Figure 2.1: Fault system in the area studied from Lavecchia et al. [2012]

2.1 Database preparation

We have collected a strong motion database, starting from the RAN national strong motion database, to be later on merged with other available databases, for the relocation of the Emilia 2012 sequence. This work was done in strict collaboration with the Mirandola Earthquake Working Group (Department of Civil Protection, DPC, University of Chieti, SeisRaM, Regione Umbria), that pre-processed all the quasi-real-time data, with magnitudes Ml 4.0 recorded by the National Accelerometric Network (RAN) managed by DPC. All the available waveforms of these ($M_l \geq 4.0$) events have been manually picked. RAN counts more than 500 stations covering all the Italian territory. All the stations are equipped with three-components (24 bits) digital instruments and make use of the GPRS data transmission. The data acquisition centre of the network, the CAED center, is located in Rome, at the DPC [Gorini et al., 2010, Zambonelli et al., 2011]), where all the data are collected and processed in real time. Two technically different networks are included in the RAN: one is the old network located inside ENEL electric transformer cabins (more than 190 stations) and now mainly equipped with the Reftek acquisition system and Syscom sensors; the other network is the one composed of stations recently installed in the free field, mainly equipped with Kinemetrics Etna accelerometers. Two local networks, the Friuli Venezia Giulia Accelerometric Network (Costa et al. [2009]; http://rtweb.units.it/), located in NE Italy, and the Irpinia Seismic Network (Weber et al. [2006];

http://isnet.na.infn.it/) contribute their data into the RAN data acquisition system. A dataset is maintained containing the raw waveforms, all the information about the instrumental responses, the association of events with INGV locations, and the related strong motion engineering parameters (PGA, PGV, PGD, PSA, Arias, Housner ecc.). About 140 stations of the RAN triggered due to the main shock of the Emilia sequence, seven of these stations were operating within 50 km from the mainshock epicentre. The RAN stations recorded the strong motions of the mainshock, as well as of the foreshock and of the aftershocks of magnitude $M_l \geq 4.0$. Soon after the mainshock, the DPC installed 15 temporary stations to increase the network coverage in the epicentral area. The strong motion database, constructed with the Antelope software, contains 35 events with $4.0 < M_l < 5.9$ and 13 events, with $4.5 < M_l < 5.9$ (available online). The database contains more than 900 waveforms (3 channels) with epicentral distances from 4 to 210 kilometers recorded by 164 stations.

In order to construct a complete database used for the relocation of Emilia sequence, the RAN strong motion database has been merged with the available velocity and acceleration data extracted from the EIDA database (European Integrated Data Archive) and velocity data recorded by the Southeastern Alps Integrated Network (Department of Mathematics and Geosciences (DMG), Istituto Nazionale di Oceanografia e di Geofisica Sperimentale (INOGS), Agencija RS za okolje (ARSO) and Zentralanstalt fr Meteorologie und Geodynamik (ZAMG)).

2.2 Manual picking and location

We have tested the quality of our manual pickings using the modified Wadati diagram (Figure 2.2). In the y-axis the dTs(s) are the differences of S-phases for each couple of stations and in the x-axis the dTp(s) are the differences of P-phases for each couple of stations. The modified Wadati diagram studies the Vp/Vs ratio as the slope of these lines, whose are the regression of the dTs(s) and dTp(s) for each couple of stations. The Vp/Vs ratio indicates the material nature of the media passed through the seismic waves. Our area of study is composed, basically, by carbonatic sediments, with a Vp/Vs ratio of about 1.8. This is the value, which we are aiming for. The green line is the interpolation found using all the phases of all the events studied, the value of the slope in this case is Vp/Vs ratio as 1.79. The red line is the interpolation of the phases of only the 29th May 2012 event and in this case the value of the Vp/Vs ratio is 1.83. These two lines, the green one and the red one, fit very well to the theoretical value, 1.8. The light blue line is the interpolation

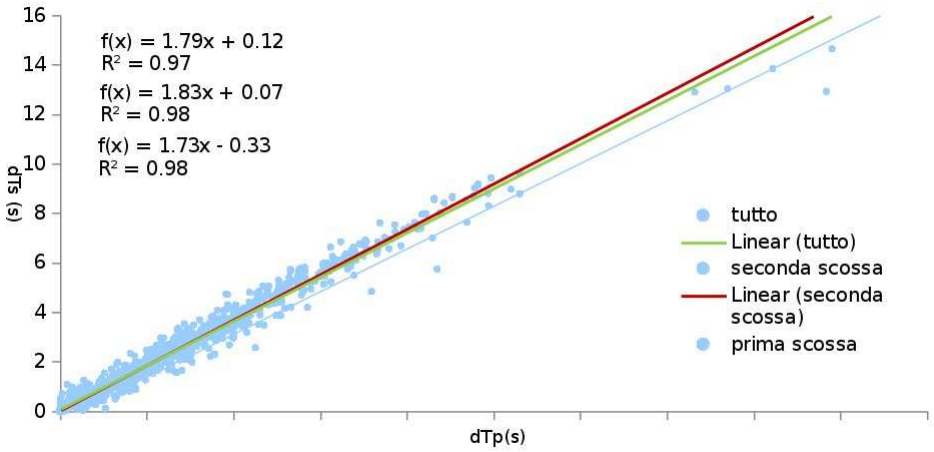

Figure 2.2: Wadati diagram of the manually P- and S- picked phases. The green line is the interpolation found using all the phases of all the events studied. The read line is the interpolation of the phases of only the 29th May 2012 event. The light blue line is the interpolation of the phases of the main event of the 20th May 2012

of the phases of the main event of the 20th May 2012 with a Vp/Vs ratio of 1.73. As it is clear from the diagram the light blue line distance itself from the other two, a possible reason could be that for the major event of the 20th May of 2012, we have only the data of a few permanent stations. After this mainshock, many temporary stations were installed, this could be the cause of why we have a different result examining only the second mainshock of the 29th May of 2012. After this analysis we can consider as plausible a Vp/Vs ratio of 1.80 as the average between the one calculated using all the events and the one calculated only the second mainshock.

As starting point we have studied the existing bibliography of the studied area, and then we have selected eleven different velocity models (Figure 2.3), such as: Bragato et al. [2011], Ciaccio and Chiarabba [2002],Costa et al. [1992], Iside, Zollo et al. [1995], Malagnini et al. [2012], Massa [2012] and four geological models proposed by Lavecchia et al. [in prep.]. The choice of the Iside model could be singular, because is an average velocity model for all the Italy, but we have used it to start our elaboration and we report the preliminary results with all the studied models for further information, in addition is the velocity model, used by INGV, for the quasi real-time location in the Italian Seismic Bulletin. Afterwards, the P and S pickings have been used to locate with program Hypoellipse (see Section 1.3) all the events. Here, we present all the locations, made with Hypoellipse, with all the eleven velocity models in Figure 2.4. As it is possible to evince from

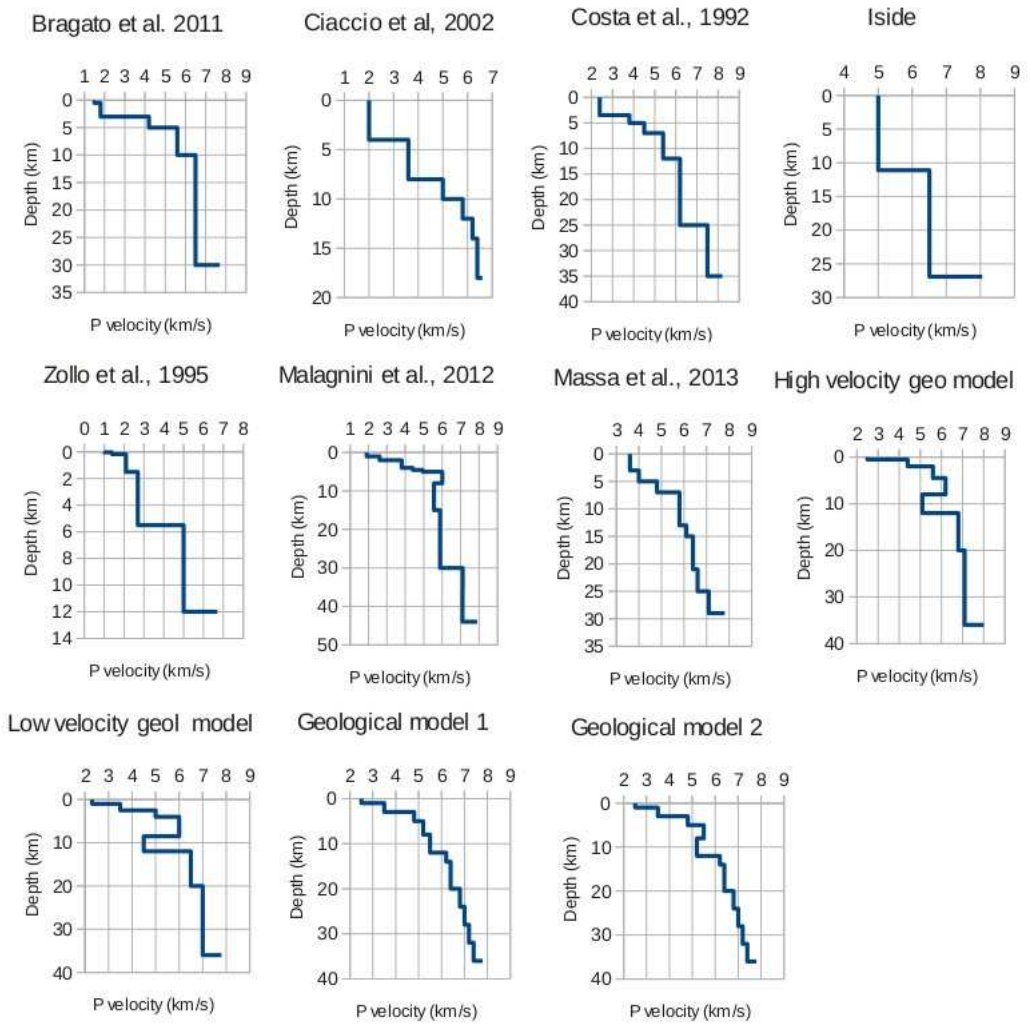

Figure 2.3: P velocity profiles of all the models used to locate the Emilia sequence.

the figure 2.4 all the different solutions don't differ a lot in the horizontal coordinates. In Figure 2.5 we show the different vertical profiles from all the eleven velocity models, in depths the solutions are not so similar than in the case of the horizontal coordinates, but we are not able to discriminate a velocity models respect an other from those solutions. As it is easy to see from the Figure 2.5, the solutions are quite similar so there is not a favourite velocity model respect the others, instead all the velocity models used differ quite a lot. In order to solve this issue, we have calculated the average (for all the 48th events studied) of the root means squares (RMS), horizontal and

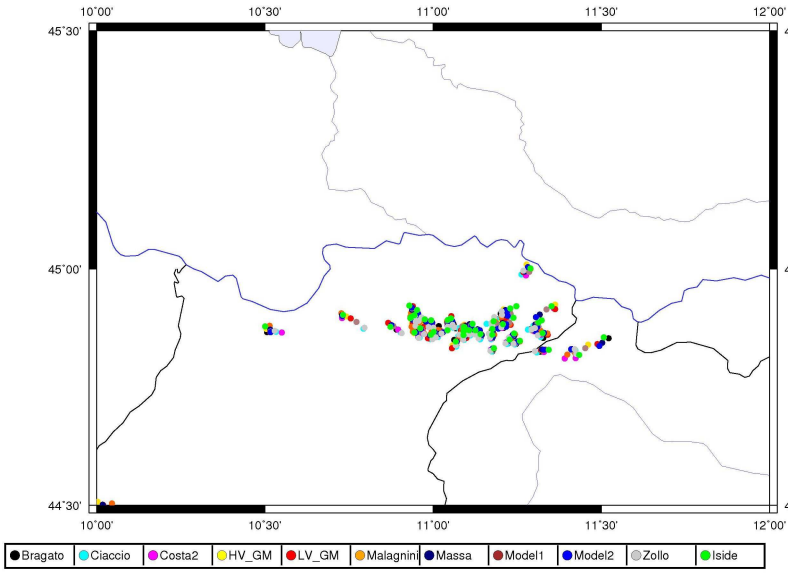

Figure 2.4: Locations of all the studied events of the Emilia sequence of May-June 2012 solved with eleven different velocity models

vertical errors for each model in figures 2.6, 2.7, 2.8 respectively. From these preliminary results it seems that the Malagnini et al. [2012] velocity model, which is a slow-velocity model, causes a shift towards the surface for all the events, this is the explanation of the high mean vertical error respect the other models (Figure 2.8). Then we have made other different analysis in order to study how much the locations made from different velocity models, differ from an average location. To do that, we have calculated the average location between all the models studied and then we have calculated the horizontal and the vertical distances between each location with the average one, for each velocity model used. For the first test, we have calculated the mean between all the average distances calculated for each velocity model (Figure 2.9)for each event. It is possible to see that only few events (numbers 10 and 27) are not consistent with all the others. In details these three events have only few available waveforms, so probably this is could be the reason of such result. In general analyzing all the other events, we can see that there is no particular event which can modify the general trend of the misurations. We have done the same analysis for the vertical component, calculating the depth differences with a mean depth value (Figure 2.10). As in the previous analysis, the events numbered 10, 11, 27 and in this case also the 45, scatter from the general trend of all the events. In this case, we see a greater scattering than in the case of the horizontal coordinates.

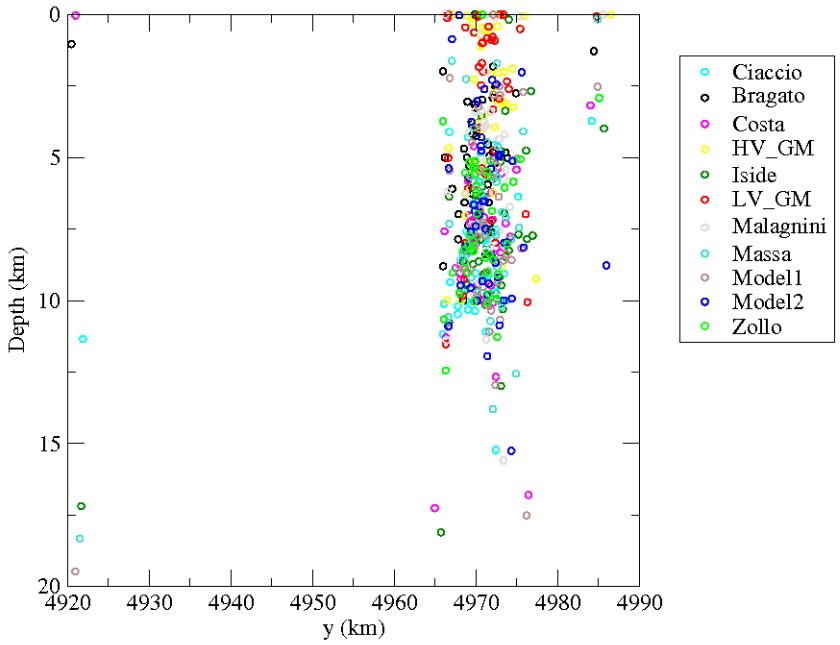

Figure 2.5: Depth profile of the locations calculated using the Bragato velocity model (black circles), using the Ciaccio velocity model (sky blue circles), using the Costa2 velocity model (magenta circles), using the HV_GM velocity model (yellow circles), using the Iside velocity model (green circles), using the LV_GM velocity model (red circles), using the Malagnini velocity model (grey circles), using the Massa velocity model (light blue circles), using the Model1 velocity model (brown circles), using the Model2 velocity model (blue circles) and using the Zollo velocity model (light green circles)

For the second test, we have calculated the mean between all the average distances calculated for each event (Figure 2.11) for each velocity model . For our purposes this test could be more significant to know how the velocity model influences the location. It is clear to see from Figure 2.11 that the velocity model does not influence very much the horizontal coordinates in fact for each model we have consistent results from each other. We have made the same test for the vertical distances (Figure 2.12). From the Figure 2.12 we can notice that the choice of the velocity models mainly influences the depths instead of the horizontal coordinates, even if in the standard deviation range. For that reason, it is not possible to discriminate a velocity model respect an other.

After this study, we have located these sequence of events using the HypoDD (see section 1.4) software, based on the double differences technique,

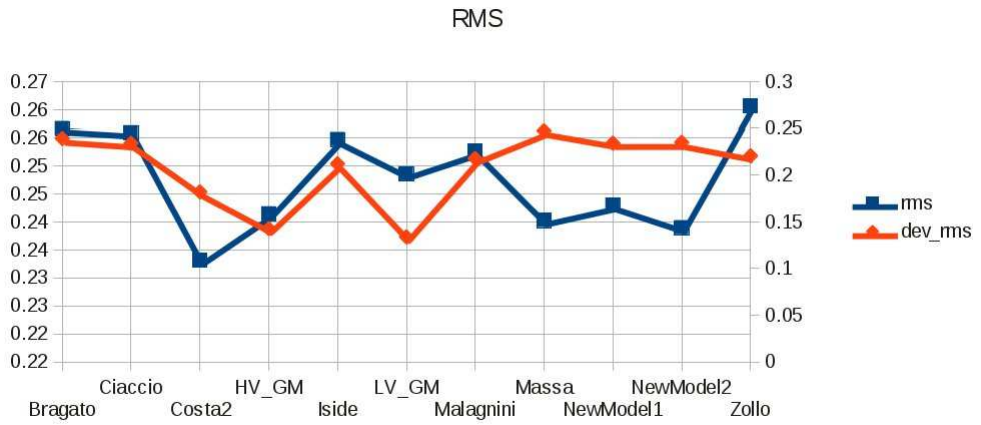

Figure 2.6: Chart of the average RMS (left column) for all the studied velocity models and the st. dev associated (right column)

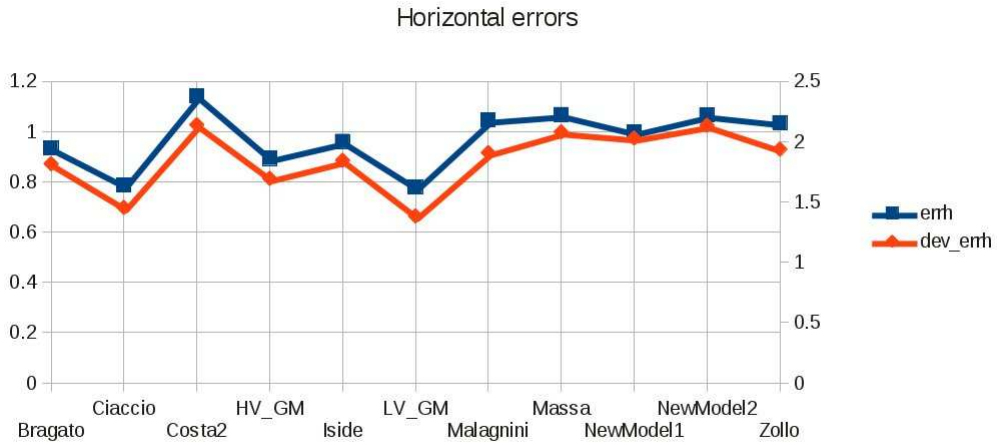

Figure 2.7: Chart of the average horizontal errors (errh on the left column) for all the studied velocity models and the st. dev associated (dev_errh on the right column)

in order to determine, in a quantitative mode, the degree of clusterization of two or more events in a small area as in this case. In figure 2.13 are reported the event locations using the eleven different velocity models. The eleven sets of solutions do not differ too much from each other, so also in this analysis we could not discriminate a model respect another. We report also the different solutions in depth (figures 2.14-2.24), one for each model used compared with the Hypoellipse solutions. In many cases it is possible

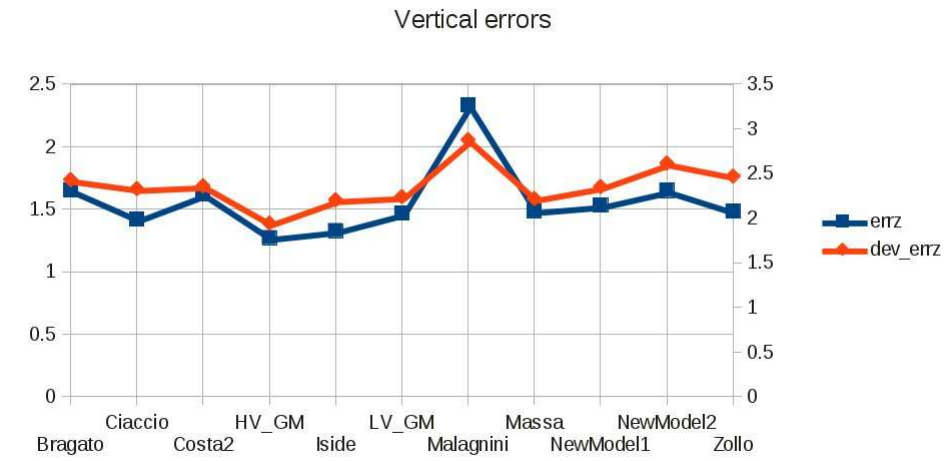

Figure 2.8: Chart of the average vertical errors (errz on the left column) for all the studied velocity models and the st. dev associated (dev_errz on the right column)

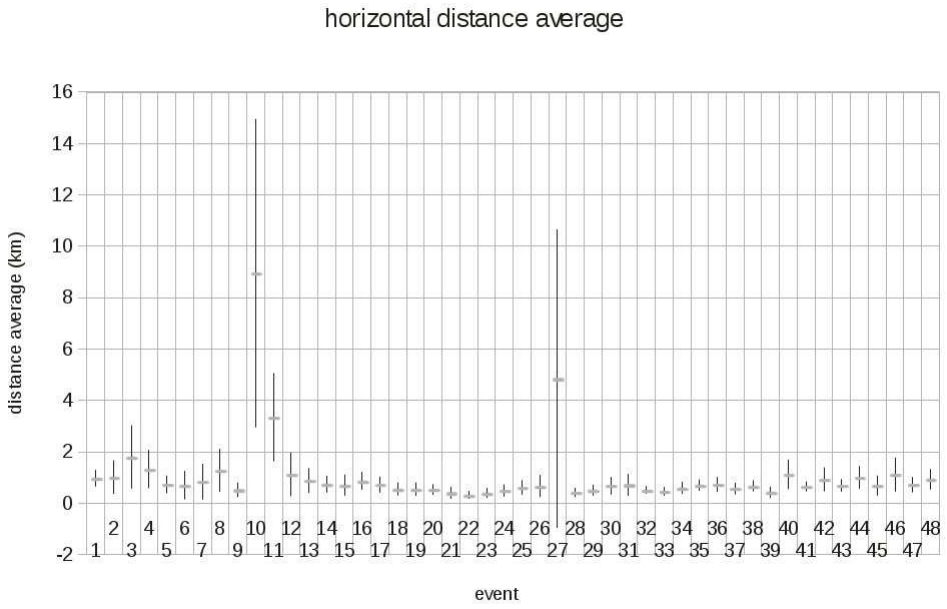

Figure 2.9: Horizontal distance average for each event, between the different location results with an average ones

to see that the HypoDD algorithm does not locate all the events as Hypoellipse does, because it clusterizes the solutions, but not too much to identify a better velocity models.

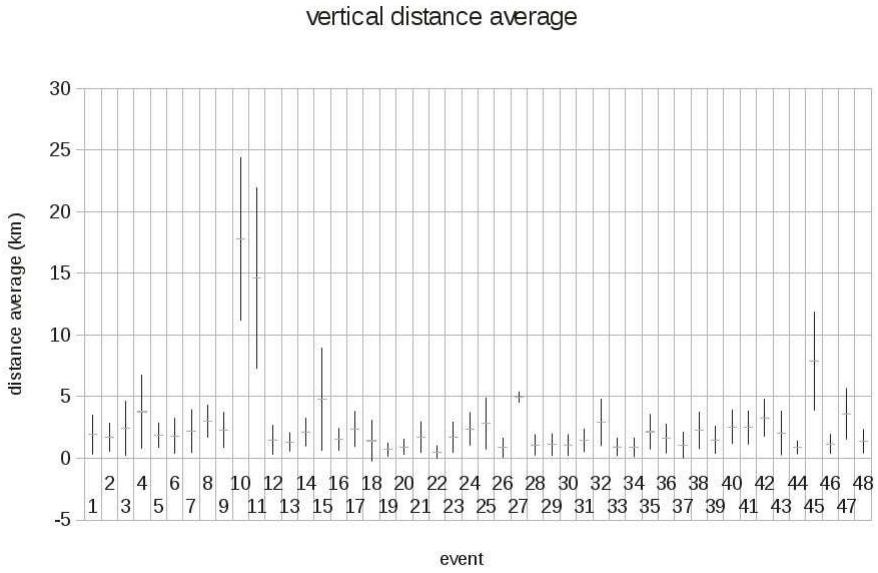

Figure 2.10: Vertical distance average for each event, between the different location results with an average ones

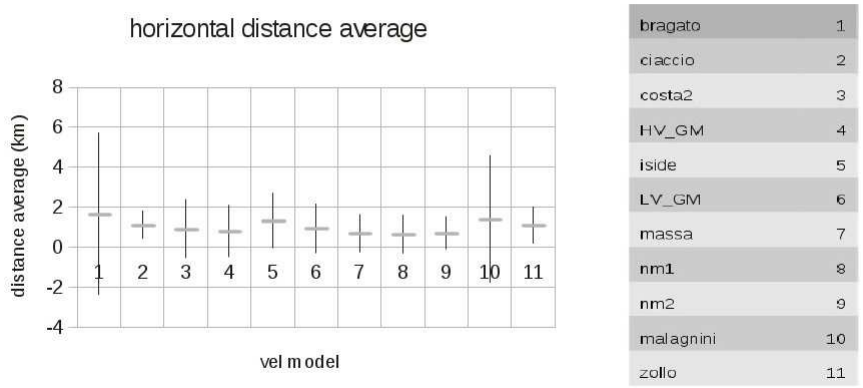

Figure 2.11: Horizontal distance average for each velocity model, between the different location results with an average ones

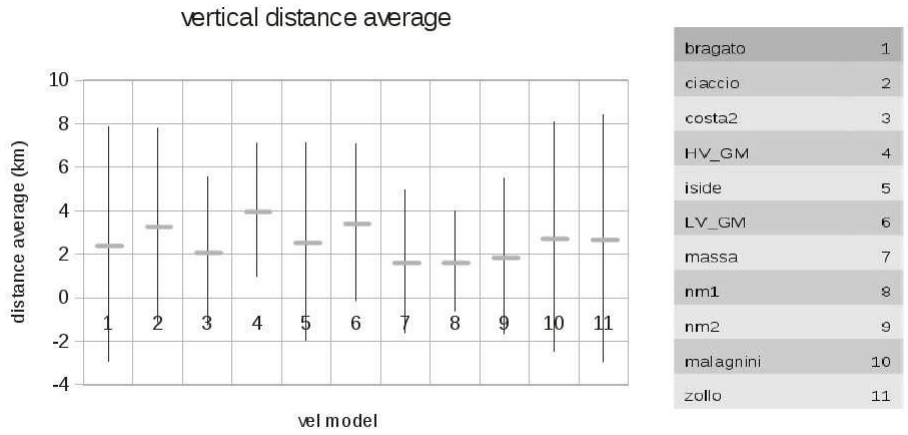

Figure 2.12: Vertical distance average for each velocity model, between the different location results with an average ones

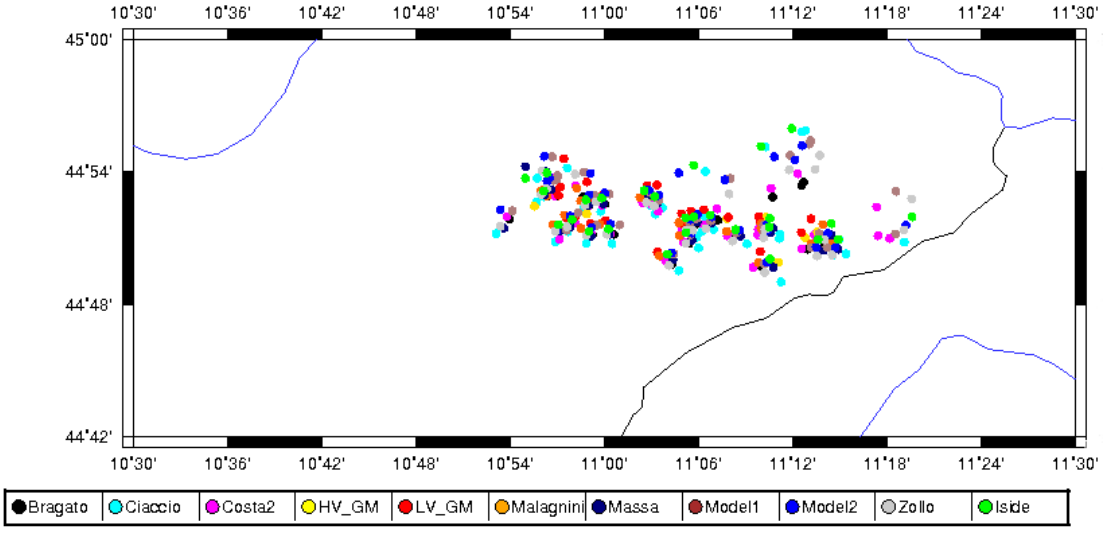

Figure 2.13: Map of the event locations produced by different velocity models with the HypoDD technique

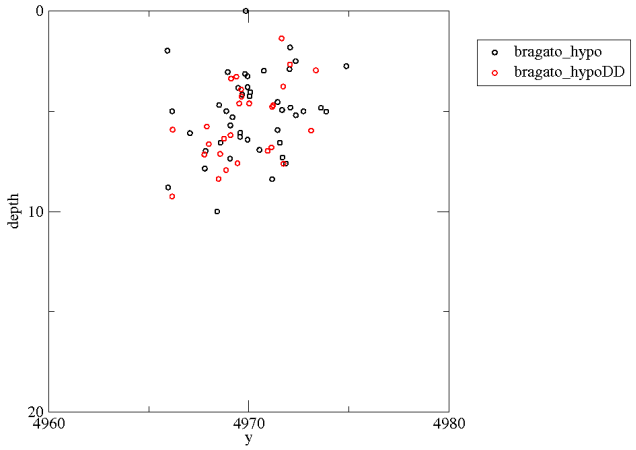

Figure 2.14: Depth profile of the locations calculated using the Bragato velocity model

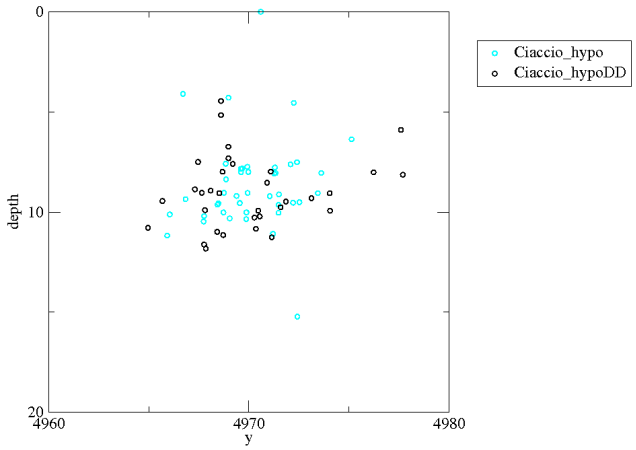

Figure 2.15: Depth profile of the locations calculated using the Ciaccio velocity model

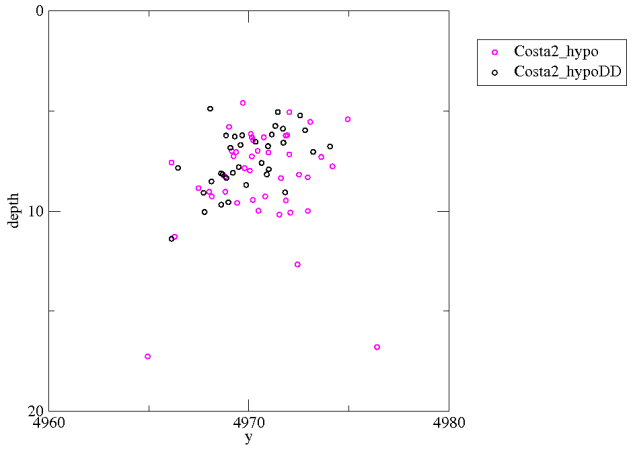

Figure 2.16: Depth profile of the locations calculated using the Costa velocity model

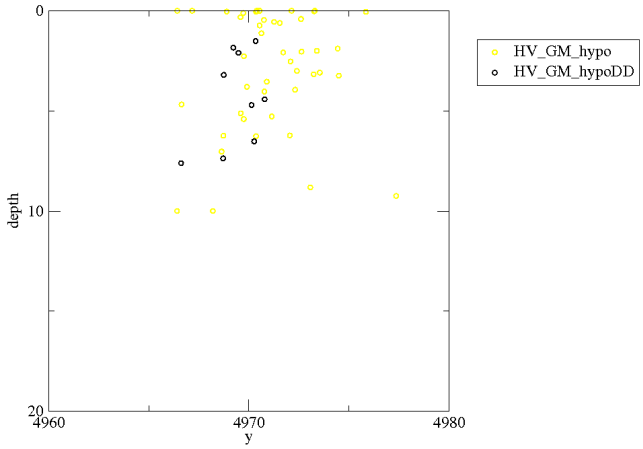

Figure 2.17: Depth profile of the locations calculated using the HV_GM velocity model

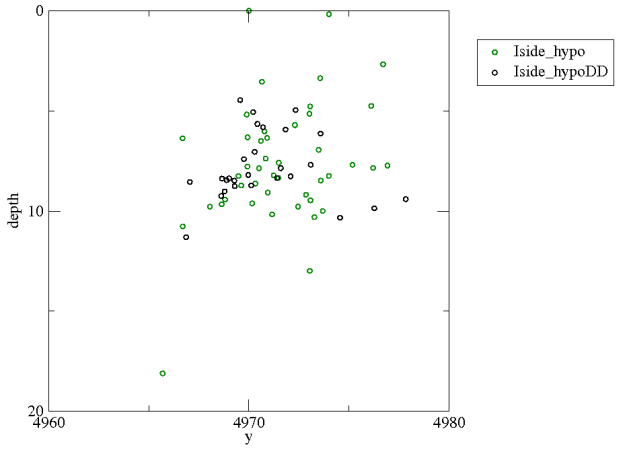

Figure 2.18: Depth profile of the locations calculated using the Iside velocity model

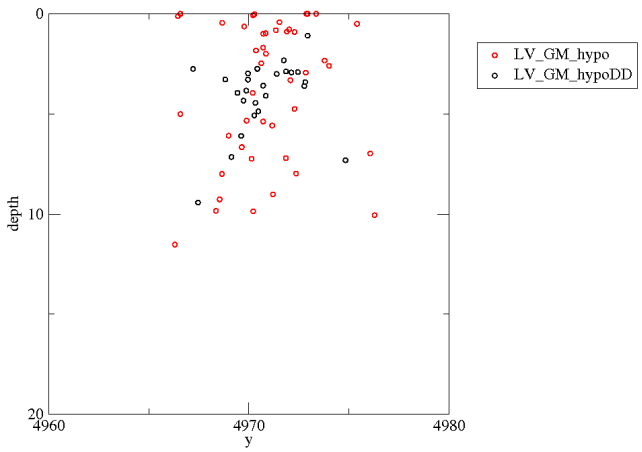

Figure 2.19: Depth profile of the locations calculated using the LV_GM velocity model

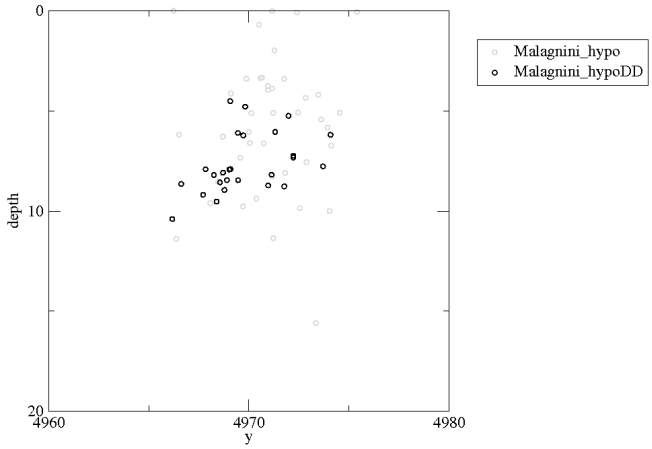

Figure 2.20: Depth profile of the locations calculated using the Malagnini velocity model

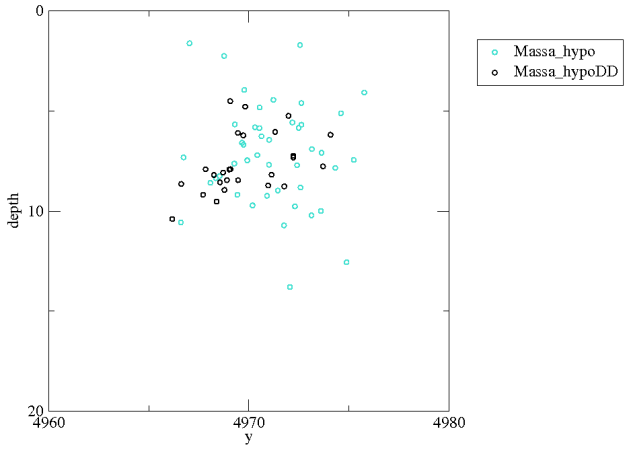

Figure 2.21: Depth profile of the locations calculated using the Massa velocity model

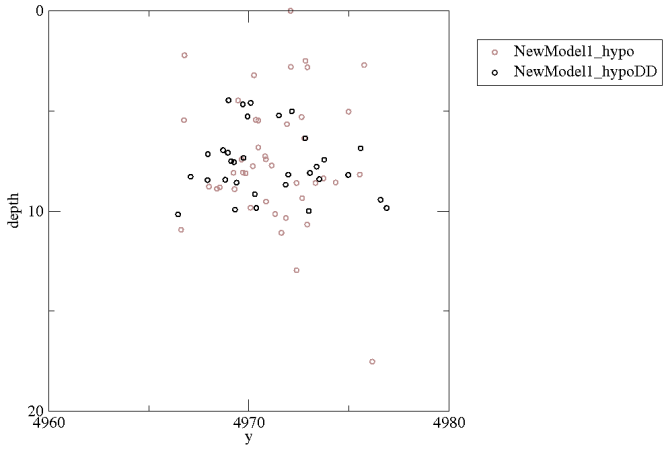

Figure 2.22: Depth profile of the locations calculated using the NewModel1 velocity model

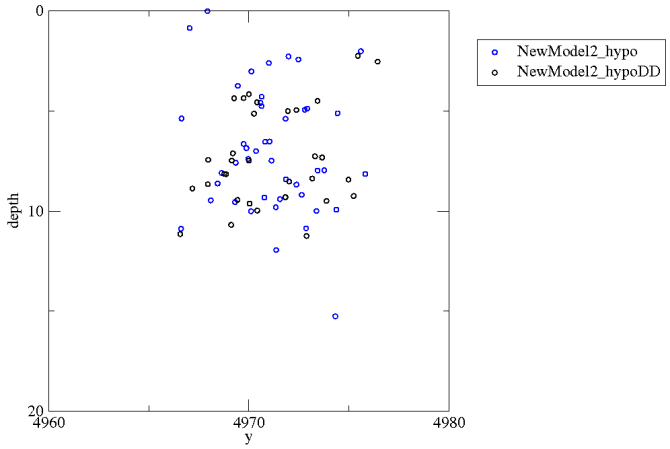

Figure 2.23: Depth profile of the locations calculated using the NewModel2 velocity model

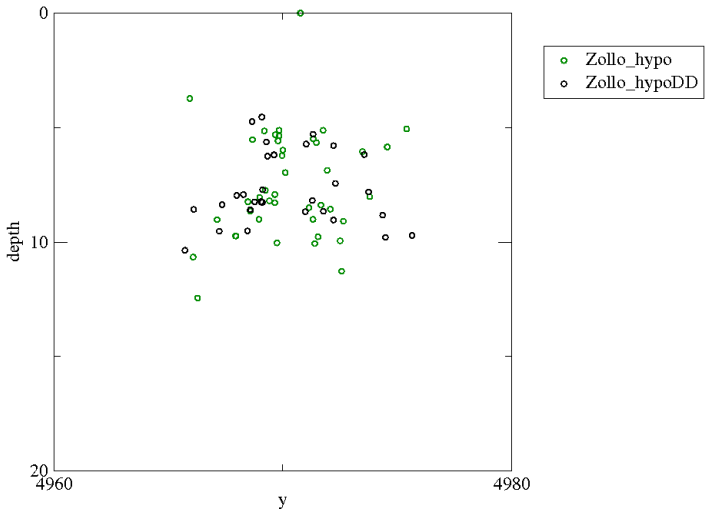

Figure 2.24: Depth profile of the locations calculated using the Zollo velocity model

At this point we have excluded from the statistical analysis, all the 'bad' events. An event is defined 'bad', or of a D-quality when the RMS (root mean square) is upper then 0.5 and the SEH (the horizontal 68% confidence limit in the least-well-constrained direction) is upper than 5.0 and also we have eliminated from our statistical study the events which have a D-quality station distribution, which it means that the number of phases are less than 6, the GAP(largest azimuthal separation between stations from the epicenter) is upper than 180 and the distance between the event location and the nearest station is upper than 50 km. So from 48 events we examine only the 41 with best quality. We have selected also few velocity models among the ones in Figure 2.2.2, the chosen velocity models are summarized in Figure 2.2.25. We have decided to eliminate from the final tests the models: 'Iside', because it is an average model from all the Italian territory and we need a more precise model; 'Ciaccio' because it is the starting point from the Massa [2012]; and we have chosen only one of the four geological models because they are similar.

By the study of the mean residuals and RMS (figure 2.27, first two columns; and figure 2.26 on the left), as in the previous data set, it is not possible to discriminate a velocity model with respect to another. On the contrary, as it possible to note in Figure 2.27 and 2.26, the distribution of

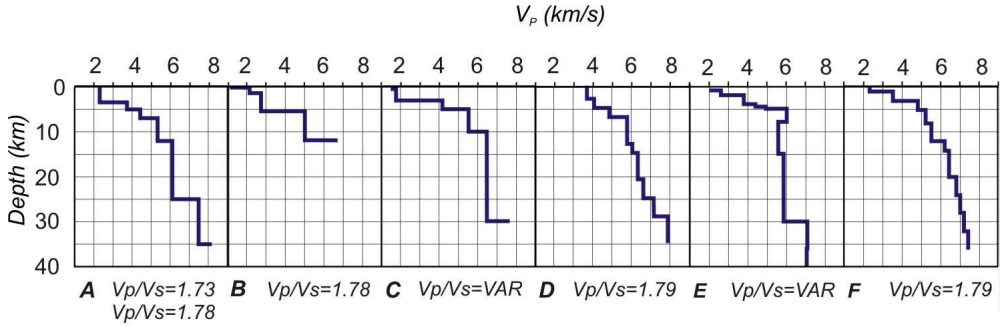

Figure 2.25: P velocity profiles of all the models used to locate the major events (Ml) of Emilia seismic sequence ($Ml \geq 4.0$). Key: A= Costa et al. [1992], B= Zollo et al. [1995], C= Bragato et al. [2011], D= Massa [2012], E= Malagnini et al. [2012], F= geological model proposed by Lavecchia et al. [in prep.])

the vertical errors among the considered velocity models are different, three models differ from the others by the vertical errror st.devation values higher than 1 km. Based on that, we have selected the velocity models: Costa et al. [1992]; Massa [2012] and the NewModel1 [Lavecchia et al., in prep.] (in Figure 2.25) as the best ones among the analyzed ones.

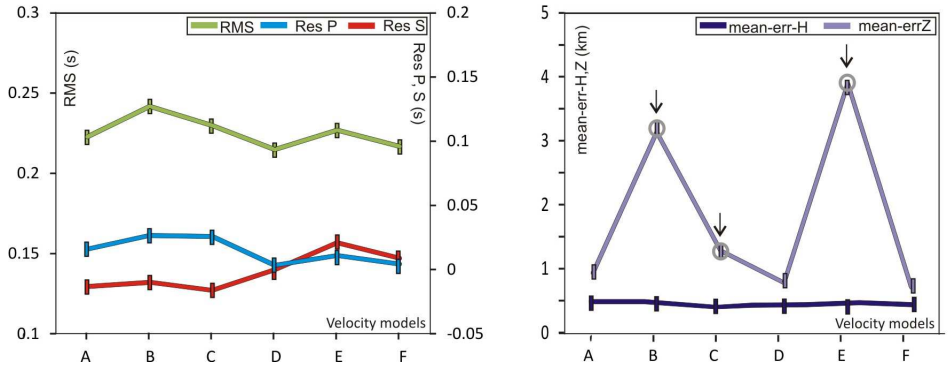

Figure 2.26: (On the left) RMS average (green line), Mean P residuals (blue line) and mean S residuals (red line) for each velocity model studied. (On the right) Mean horizontal errors (dark purple line) and mean vertical errors (light purple line). From this last one we have select only the velocity models with mean vertical error less than 1 km.

The obtained epicentral distribution of the corresponding events are reported in the map of Figure 2.28 and the range of variation in depth for each event is represented in the section of the same figure. In this section, the

geometry of the fold-and-thrust system as inferred from the interpretation of the seismic line App. Orient 1 (in Figure 2.28) is also reported (Lavecchia et al., in prep). From this analysis It seems that the Mirandola thrust (M in the section of Figure 2.28) was not involved during the Emilia sequence, whereas the internal and middle segments of the Ferrara thrust systems (e.g. Quarantoli, Q, and Ferrara, F, thrusts in Figure 2.28) were activated by 29 and 20 May seismic sequences, respectively.

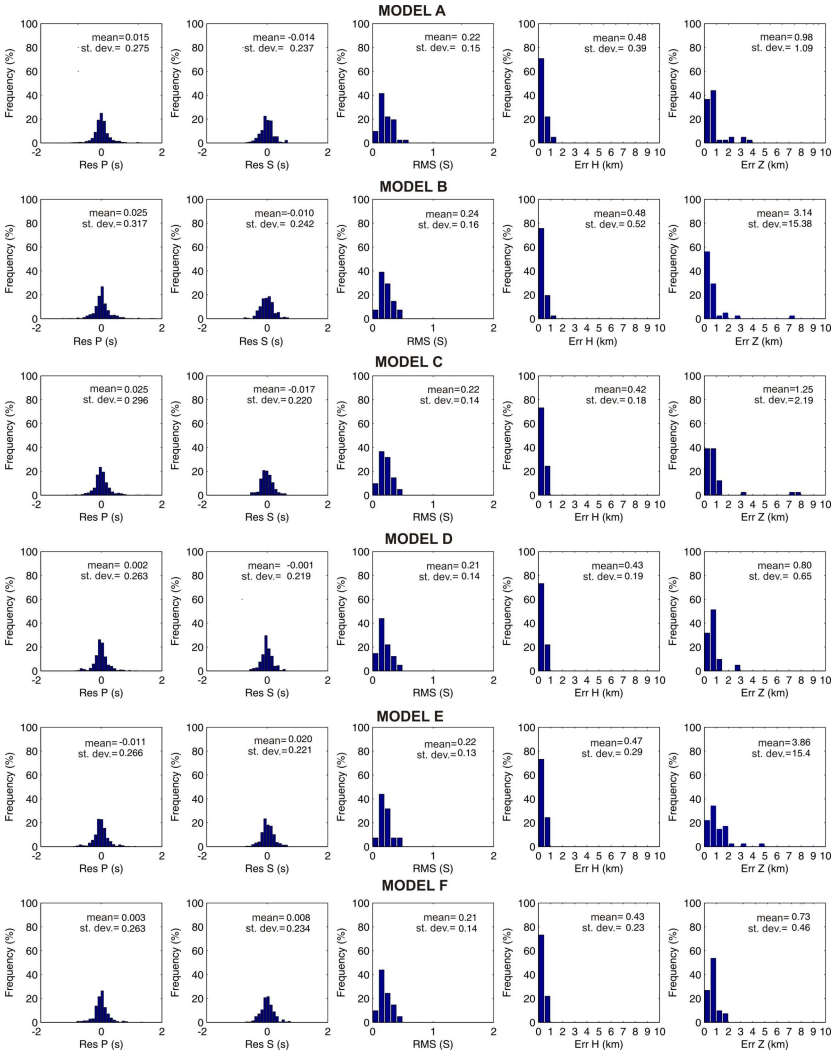

Figure 2.27: Summary of results of relocated events. Histograms of residuals of P and S phases (ResP, ResS); Root mean square of travel time residuals (RMS); Horizontal and vertical formal errors (err-H, err-Z)

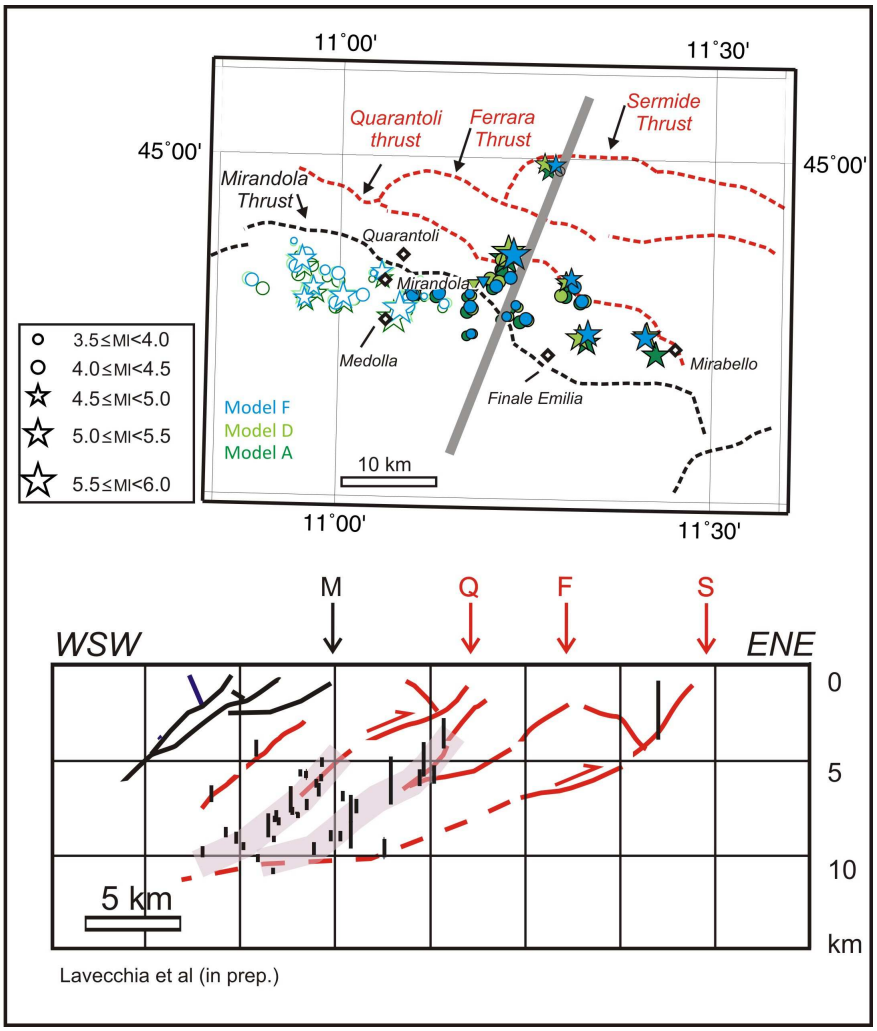

Figure 2.28: Location map of the relocated epicenters of the major events ($ML \geq 4$) of May-June 2012 Emilia seismic sequences according to different input velocity models. The empty and full simbology adopted for the epicenters refers to different time intervals (full = 20 to 28 May 2012; empty = 29 to 3 June 2012). The relocated epicenter of the major event of the July 2011 sequence is also reported. The range of vertical variation in the hypocentral depth resulting from the different input velocity model is schematically represented (vertical black line) along an interpretative geological section which extends across the Ferrara Arc fold-and-thrust system, along the trace of the seismic line App_Orien-1 [Lavecchia et al., in prep.]

Chapter 3

AutoPicker test: Comparison with manual pickings

The automatic phases detection is a long-standing problem, still under debate between seismologists. The possibility to have a precise event location in quasi real-time is considerably important and essential for focused interventions for civil defence purposes. One of the main goal of this work is the improvement and optimization of automatic monitoring system for civil defence purposes. The continuos innovation and upgrading of the monitoring system is fundamental to produce an improvement on the automatic locations quality in a quasi real time mode. The possibility to improve the phases detection (P and S) is essential in the determination of the event location. To do that, in this chapter, we evaluate the performances of the AutoPicker, described in section 1.5, a picking and locator procedure.

3.1 Data Set

This study was computed using a database composed of over 2,500 traces corresponding to 250 events recorded in the year 2011 (see Figure 3.1) by the CE3RN (Central Eastern European Earthquake Reasearch Network) in Northeastern Italy and surrounding regions (Figure 3.2). The reliability and robustness of the proposed algorithm is tested by comparing manually derived P, S readings, earthquake location (determined by an experienced seismic analyst), serving as reference database, with the corresponding automatically estimated P, S arrival times and earthquake location.

These data are collected through the use of the software Antelope (see Section 1.6). We have developed an automatic procedure which prepares the input for the AutoPicker reading directly from the Antelope database. The

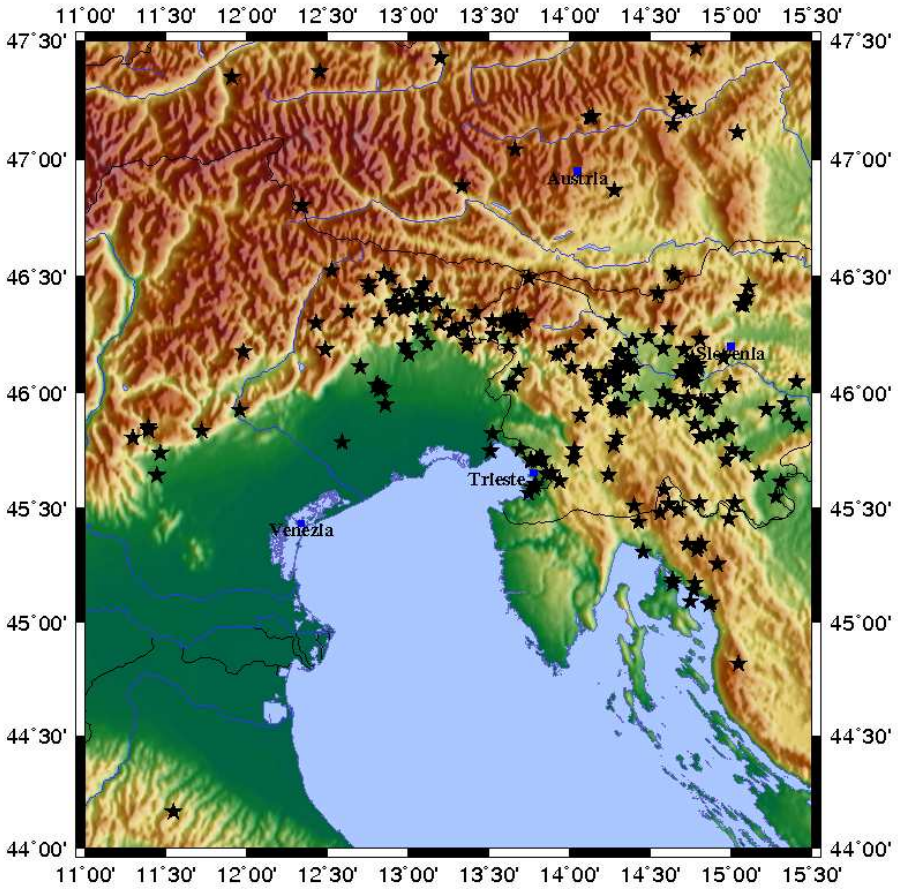

Figure 3.1: Map of the area of interest with all the epicenters (black stars) of analyzed events located with Hypoellipse using manually picked P- and S-phases used as reference.

procedure is summarized in the flowchart 3.3.

From the Antelope database we can select all the arrivals collected for the events occured only in a selected geographic area. In this study as it is possible to notice from the map in Figure 3.1, we have selected only the events occured from $11°00' E$ to $15°30' E$ and from $44°00' N$ to $47°30' N$. Then we have written into a file all the origin times of these events. A Fortran program reads this file and calculates the presignal time and the postsignal time depending on the presignal and postsignal value chosen. These two parameters have been chosen after several tests, depending on the kind of events and station network used, in order to catch the correct portion of the waveforms from all the SAC data. We have a local network and we would like to locate only locale events, so the presignal value is 60 sec as

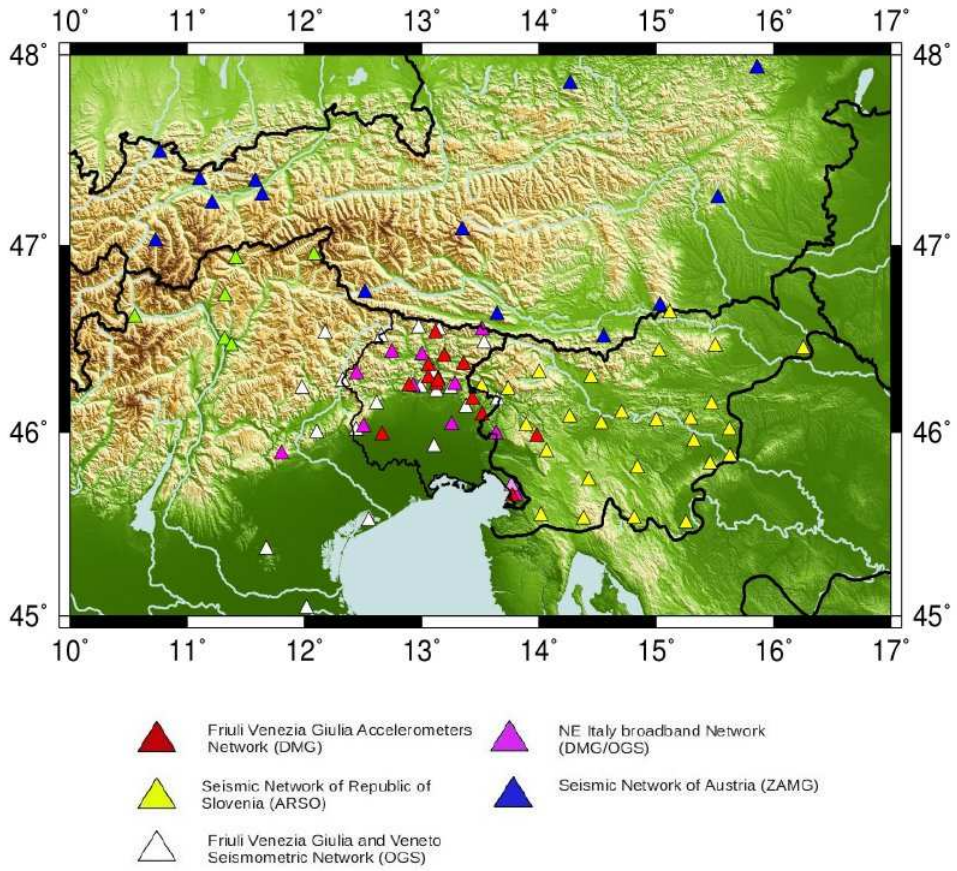

Figure 3.2: Map of the SouthEastern Alps with the seismological stations of the CE3RN network

the post signal one. We have maintened a large time window for a local event, because the AIC function needs a lot of pre-event signal in order to calculate a right energy detector of the entire signal, the envelope time function, necessary to choose a correct time window, in shich apply the AIC function (see section 1.2). Then a praticle script db2sac extracts the SAC data, from the presignal time to the post signal time, that we have chosen. Finally our procedure creates a directory for every event studied and puts in, all the cutten waveforms collected in the Antelope database. Selected the studied events, we have manually revised P- and S- readings using the SacPicker program, which displays the waveforms, event by event. All these waveform data, set, a very heterogeneous qualities of P and S onsets basically characterized by a low SNR. Then Hypoellipse processes these readings (see section 1.3) in order to obtain the hypocentral locations. These manually

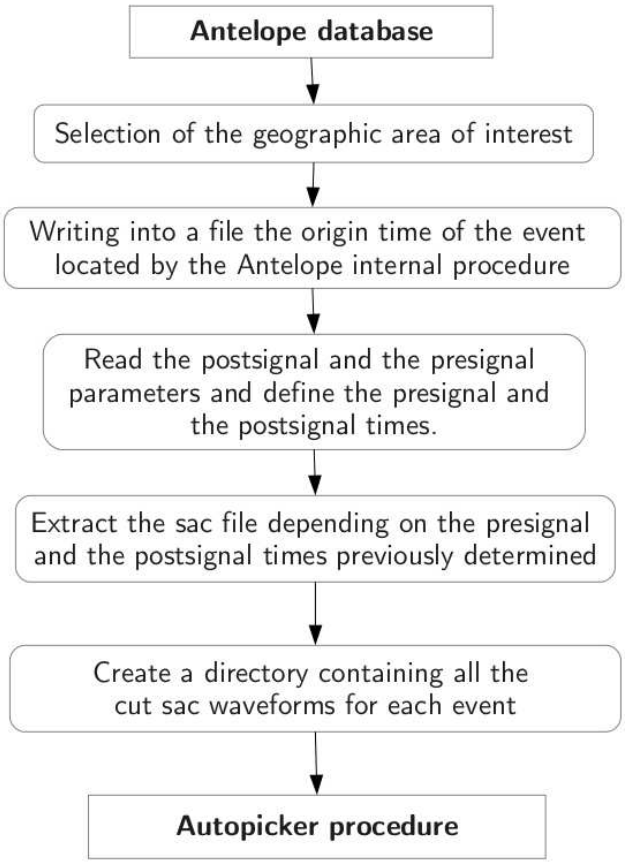

Figure 3.3: Flowchart describing the automatic procedure developed by us which automatically prepares the input for the AutoPicker starting from the Antelope database

revised P- and S- phases and the hypocentral locations obtained are used as reference data to test the automatic picking and the automatic location algorithm, respectively.

In order to use at its best the AutoPicker procedure, we have chosen the best parameters for our data. The AutoPicker algorithm requires a lot of variables to set up the picking and location methodologies, so it was necessary to make a lot of tests to obtain the best configuration: for the P-phases, after several tests we chose a four-pole Butterworth filter with a frequency range of 3.0-25 Hz as the optimal filter. We have sperimentally changed the parameters and tested the performances of the AutoPicker in order to obtain the right configuration. Instead for the S-phases we choose, even in this case,

a four-pole Butterworth filter but with a frequency range of 0.1-40 Hz. In the AutoPicker procedure (see section 1.5) we have to define when an arrival is impulsive and in this study we have defined it when the average SNR in the frequency band between 1.0 Hz and 25.0 Hz exceeds the threshold value of 200. The procedure developed to adjust Paic for strong impulsive arrivals is based on a time window of a given length, 0.3 s in this study. The two frequencies, whose define the quality of the Paic or Psample, in this work, are: Fmin is defined as the smallest frequency between 1 and 8 Hz for which the SNR is higher than 3.5 after several test; in the same way, Fmax is defined as the greatest frequency between 9 and 15 Hz for which the SNR is higher than the threshold value of 3.5.

3.2 Results

The picker has been tuned and implemented for local earthquake recorded by the CE3RN Network in Northeastern Italy and sourrounding regions. The results of comparing the analysts' picks with the automatic picks are summarized in Figure 3.4 and Figure 3.5 for P and S phases, respectively.

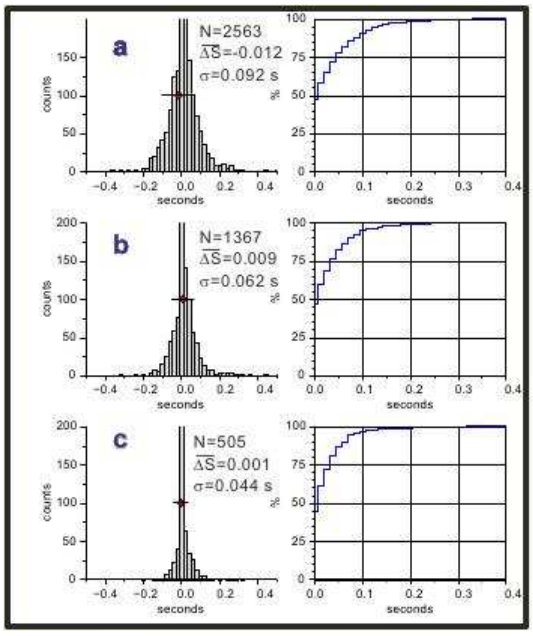

Figure 3.4: Comparison of analysts picks with automatic picks for P arrivals. Left panel: distrubution of differences. Right panel: cumulative distribution of the absolute value of differences. (a) whole dataset; (b) hypo_dist< 60 km; (c) hypo_dist < 30 Km

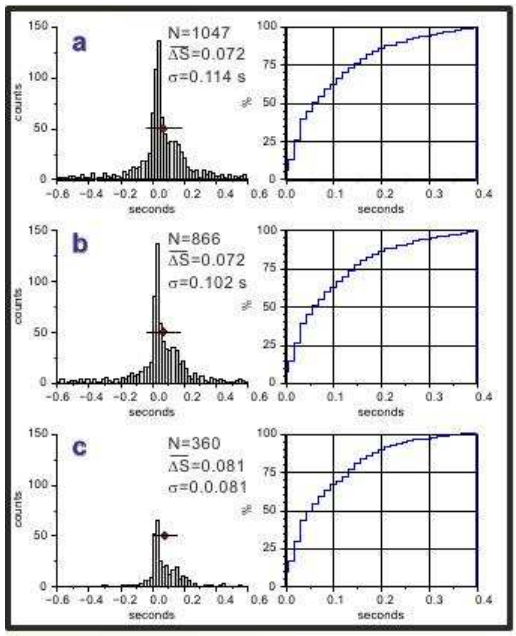

Figure 3.5: Comparison of analysts picks with automatic picks for S arrivals. Left panel: distrubution of differences. Right panel: cumulative distribution of the absolute value of differences. (a) whole dataset; (b) hypo_dist < 60 km; (c) hypo_dist < 30 Km.

Out of 3100 P-phase onsets our implementation detects 85% and gives a mean difference of -0.012 sec (Figure 3.4a). For S-phase our implementation detects 70 % and gives a mean difference of 0.072 sec (Figure 3.5a). For hypocentral distances less than 60 km we found that about 95% of P autopicks are within 0.1 sec of analyst picks (Figure 3.4b). For S phases about 85% of autopicks are within 0.2 sec of the analyst picks (Figure 3.5b). In Figure 3.6 is shown the effect of the automatic picking on the location of the 250 events used in this study.

For more than 90% events the epicentral difference is less than 5 km (Figure 3.6 left panel). The average value of differences between depths is 0.4 km and the standard deviation is 3.9 (Figure 3.6 right panel).

In summary, the proposed automatic picker appears to be a useful tool for assigning automatically onset P and S times to detected seismic signals for the purpose of rapid epiceter calculations. Provided, however, that an high frequency filtering is applied to broad-band data and minimum a priori information (time windows for the AIC function application, for details see paragraph 1.2 and 1.5) is used to guide the picker.

This encouraging results have allowed us to proceed comparing this new

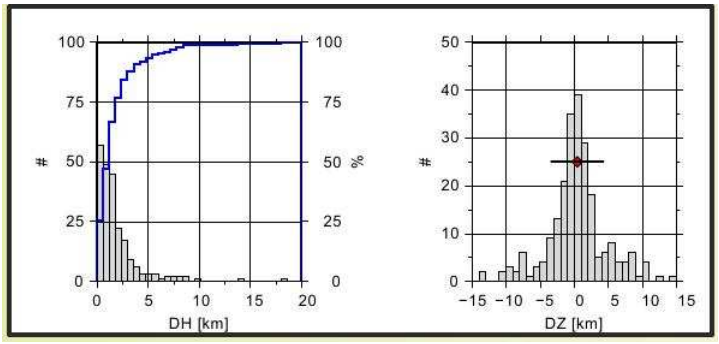

Figure 3.6: Comparison of references location with automatic ones. Left panel: distribution of epicentral differences and cumulative curve. Right panel distribution of depth differences

picking methodology to another one, tested and used daily and in real-time by us to detect and locate events, the STA/LTA technique in the Antelope software (see section 1.6). So in the next chapter we present a comparison between these two methodologies.

Chapter 4

AutoPicker test: Comparison with Antelope

Based on the previous results described in chapter 3, we would compare the AutoPicker (see section 1.5) method with a more tested and solide one, the Antelope picking method (see section 1.6) using as reference pickings and locations the manual ones. The software Antelope is daily used at the DMG for the quasi real-time location of the seismic events. This comparison it is fundamental to understand, if there is, which one of the two algorithms better detects phases and/or locates event; in order to merge and implement these two techniques to obtain a better detector and locator.

4.1 Data Set

Our reference data set consists of 44 events of $M_l \geq 4.0$ from Emilia sequence of 2012 occurred in May-June and acquired by RAN (Rete Accelerometrica Nazionale) and INGV (Istituto Nazionale di Geofisica e Vulcanologia) networks in the Po Plain and surrounding regions (mainly broadband stations)(Figure 4.1).

These data are collected through the use of the software Antelope (see section 1.6). In order to extract the data from the Antelope database we use the same automatic procedure described in section 3.1 in Figure 3.3 From the Antelope database we have selected all the events occured from $10°00' E$ to $12°00' E$ and from $44°30' N$ to $45°30' N$. In this study the presignal time and the postsignal time chosen are 40 seconds, less than in the work in chapter 3. This is because in this sequence of events most of them occured near each other in time, then we need shorter seismograms to exclude the subsequent events; on the other hand in some cases it is possible that the AutoPicker

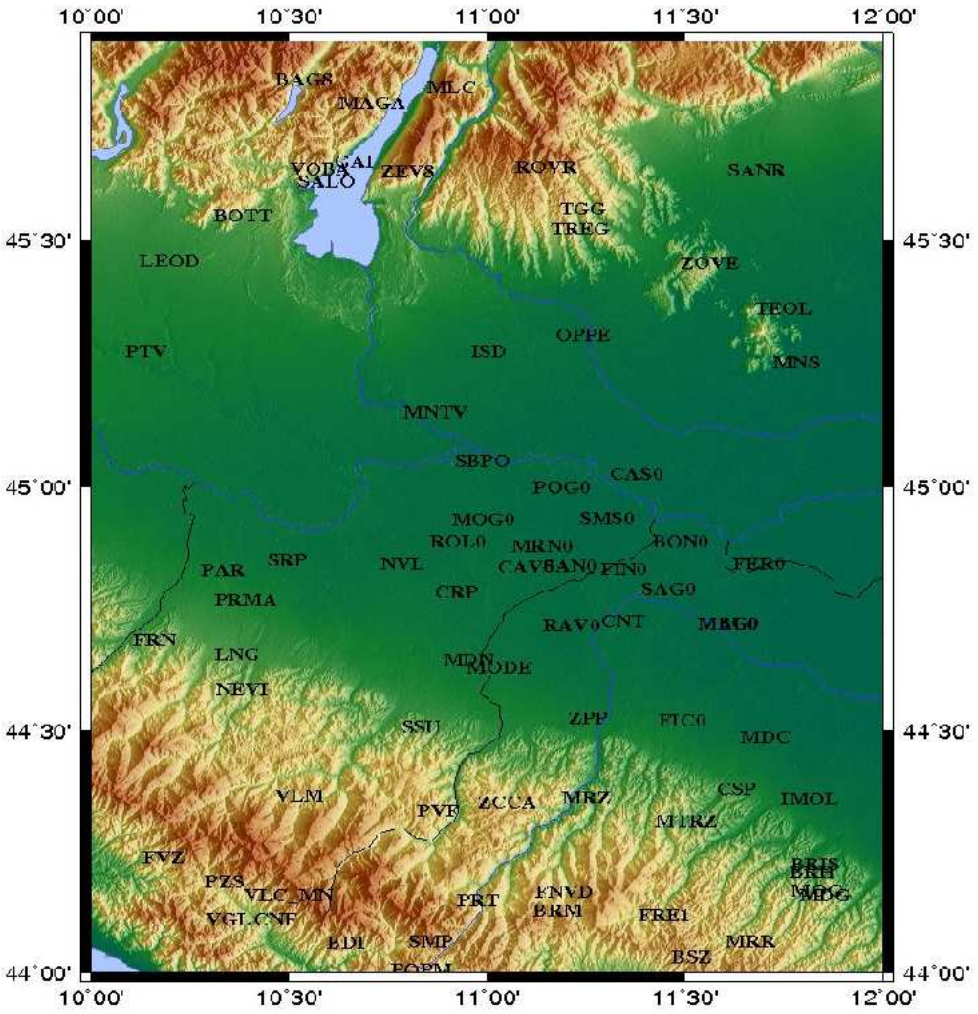

Figure 4.1: Map of the area of interest with all the stations used in this study

does not have the necessary presignal time to rightly calculate the envelope time function.

Through the use of the Hypoellipse code, we elaborate the manually revised P- and S-phase readings in order to obtain hypocentral locations; these ones are used as reference data to test automatic picking and automatic location algorithms, respectively. These manual locations are the results of a previous work done with DPC (Dipartimento di Protezione Civile) and University of Chieti (Dolce et al. [2012]), well described in chapter 2.

In order to use at its best the AutoPicker procedure we have chosen the best parameters for our data, which are the same of the one used in the chapter 3.

	Filter	sta_twin (sec)	lta_twin (sec)	Thresh
1	BW 2. 4 8. 4.	0.25	300.0	5.0
2	BW 1 4 8 4	0.30	10.0	4.0
3	BW 1 4 8 4	0.25	10.0	4.0
4	BW 0.8 4 6 4	1.5	10.0	4.0

Table 4.1: Set of parameters used in this study for the Antelope's detection procedure: the 'Filter' is the one applied to the waveform before the STA/LTA algorithm has been processed. 'Sta_twin' is the windown length in time for the short time average, the 'lta_twin' is the window length in time for the long time average. The thresh is the SNR (signal to noise ratio) value that a sample has to pass over to become a detection

The Antelope procedure is divided in detection and then association. For the STA/LTA algoritm, it is possible to choose more than one set of parameters, for this elaboration we use four set of parameters, related in the table 4.1.

The set of parameters number 1, in table 4.1 is the one used as default, the other three refer to local event, the ones, which we are interested in. The set number 2 and 3 are for the P- phases in fact really similar each other, than the last one that is for the S-phases with a different fequancy band in the filter, and a more longer STA time window.

For the locator part of the Antelope software, we report, in the table below, the parameters for the local events, because all the Emilia sequence, which is the one that we would like to locate, is a local sequence (see section 1.6).

The parameters and options used by the associator for the local grid, are summarized in table 4.2. The nsta_thresh is the minimum number of stations that have triggered the event, that is going to be located. Obviously the number of station depends on the distance of the hypothetical epicenter, so there are three minimum thresholds for this value: if the distance is less of 0.5°, are necessary only 5 stations to locate the events and so on. The three option: try_S, associate_S and reprocess_S are well explained in the section 1.6. This configuration means that firstly we make a preliminary location only with the P-phases (try_S no), after that Antelope calculates a possibile time window in which finds the S-phases and associates them (associate_S yes). Then the associator makes the final location with P- and S-phases (reprocess_S yes). It is also possible to choose which phases used for the

Trigger number of station	5	
nsta_thresh	0.5°	5
	2.0°	10
	180.0°	12
try_S	No	
associate_S	Yes	
reprocess_S	Yes	
Phase_sifter	*	
P channel sifter	*Z	
S channel sifter	*N, *E	

Table 4.2: Set of parameters and options used in this study for the Antelope's association procedure.

location, in this study, we use all the waveforms that we have (phase_sifter *). We, also, choose to detect P-phases only in the vertical component (P channel sifter *Z) and S-phases only in the two horizontal ones (S channel sifter *N, *E).

The AutoPicker location is depending on the one of Antelope software, beacuse in order to extract the SAC waveform for the AutoPicker procedure, we use as starting point the origin time calculated by Antelope methodology.

4.2 Results

We compare the two set of automatic locations: the AutoPicker ones and the Antelope ones, using as reference data set the manual ones (Chapter 2). In figures 4.2 and 4.3 are shown the differences paths of the manual epicentral locations (black stars) and the automatic epicentral locations (blue stars) using Antelope and AutoPicker procedure, respectively.

The results of comparing the Antelope's picks with the AutoPicker's ones are summarized in figures 4.4 and 4.5 for P- and S- phases, respectively.

For P-phases, the distribution of differences are comparable. The average values of P differences are similar, but it's to point out that the AutoPicker procedure gives a st.deviation lower than the Antelope ones and most impor-

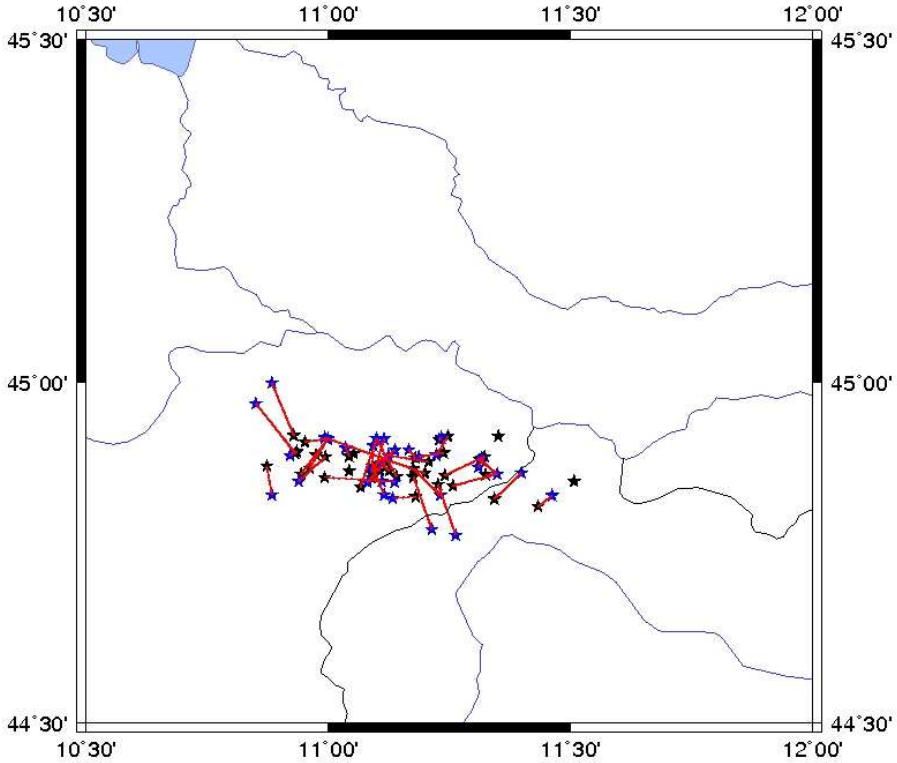

Figure 4.2: Map of the area of interest with difference paths (red lines) between manual epicenters (black stars) of analyzed events located with Hypoellipse using manually picked P- and S- phases as reference and the Antelope epicentral locations (blue stars)

tant picks the 16% of phases more than the other algorithm. For S-phases the AutoPicker algorithm picks 178 phases with a mean value of 0.09 sec, instead of the 16s of Antelope with a mean value of 3.75 sec. In figures 4.6 and 4.7 are shown the effects of the two automatic pickers on the location of 44 events used in this study.

For more than 90% events the epicentral differences of AutoPicker is less than 5 kms (figure 4.6 right panel), instead of the Antelope differences which are less than 10 kms (figure 4.6 left panel). For the depth differences the mean values and the distributions of the two procedures are quite similar, even if Antelope locates only 38 of the 44 events studied, despite of the 43 of the AutoPicker.

In summary, AutoPicker finds more and preciser phases than Antelope both P- and mainly S-phases. Orbassoc process in Antelope, is able to correctly associate the detections and to find the right location. This suggest

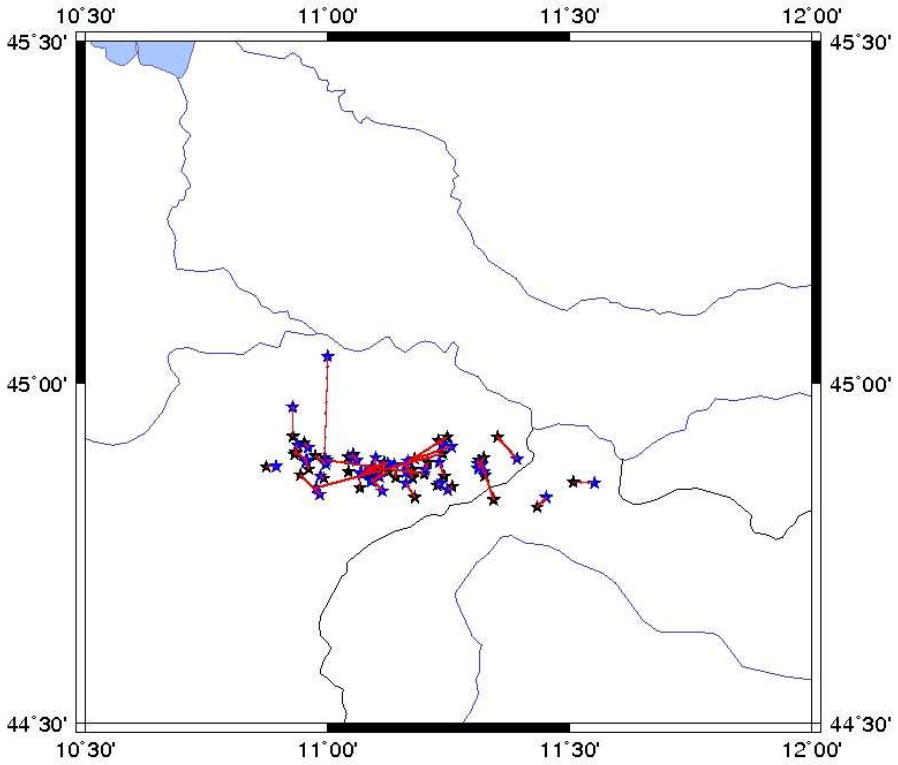

Figure 4.3: Map of the area of interest with difference paths (red lines) between manual epicenters (black stars) of analyzed events located with Hypoellipse using manually picked P- and S- phases as reference and the AutoPicker epicentral locations (blue stars)

to us to implement the AutoPicker algorithm in Antelope in order to use the AutoPicker to define P- and S-onset and Antelope to associate them and locate the events.

4.3 Preliminary implementation

We have implemented the Autopicker procedure in the Antelope ones using an external program written by us, described in figure 4.9. At this step, this procedure extracts Antelope data and changes the format of them in order to be usable by the AutoPicker.

As a starting time to calculate the time window in which extracts the waveforms, our procedure used the origin times calculated by Antelope. This program starts to work when a new row in the origin table is written. It reads

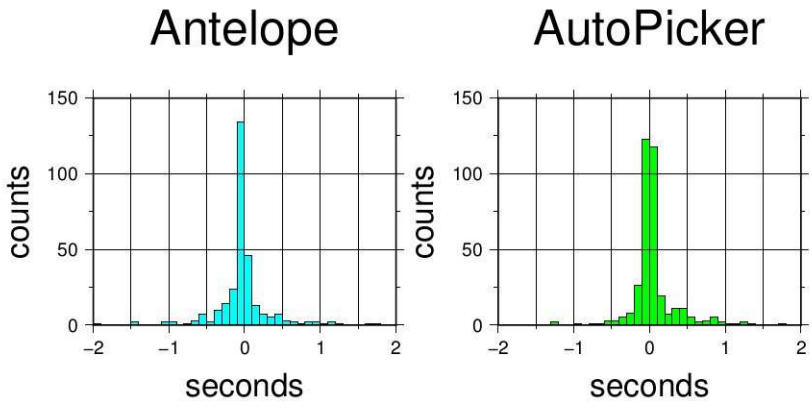

Figure 4.4: On the left: Distribution of differences between Antelope P pickings and the manual ones; on the right: distribution of differences between Autopicker P pickings and the manual ones

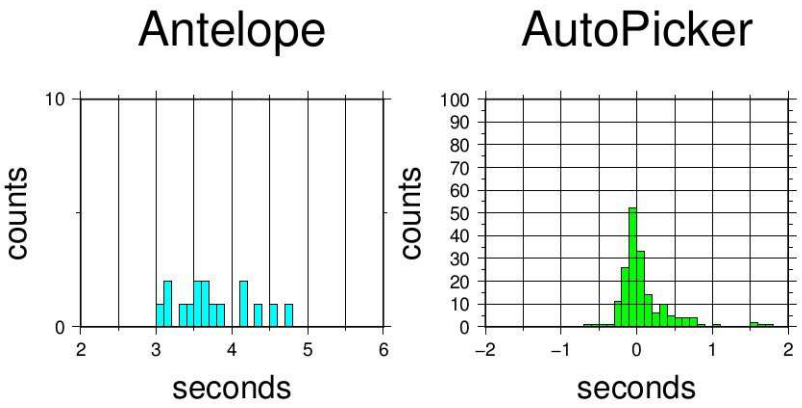

Figure 4.5: On the left: Distribution of differences between Antelope S pickings and the manual ones; on the right: distribution of differences between Autopicker S pickings and the manual ones

the origin time from the origin table and then a Fortran program calculates the presignal and the postsignal time, the two extremes of the time interval to extract. The choice of these two values are essential if we would like to elaborate local, regional or tele seismic events. Then our procedure reads and extracts the SAC waveform reading these two parameters: pre-signal time and post-signal time. Then the Autopicker procedure stars reading the cut SAC waveforms.

This procedure must be tested for a long period of time comparing the two automatic locations produced by Antelope and by the Autopicker. Then

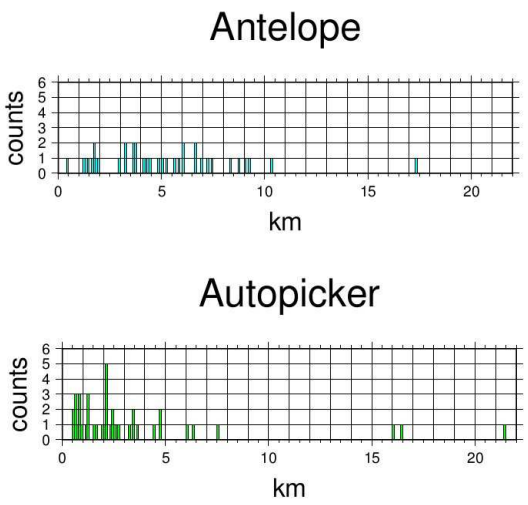

Figure 4.6: Top panel: Distribution of absolute epicentral differences between Antelope locations and the references ones. Bottom panel: Distribution of absolute epicentral differences between Autopicker locations and the reference ones

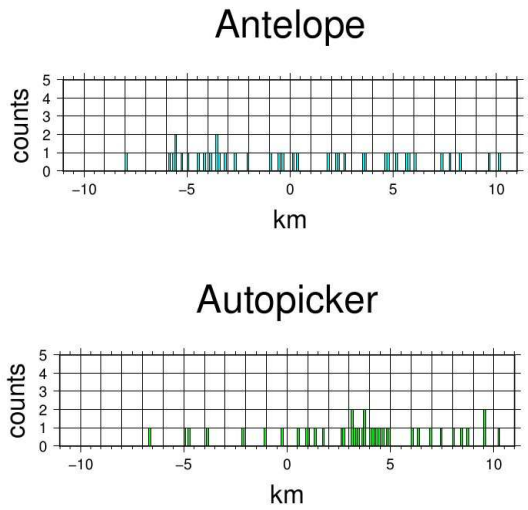

Figure 4.7: Top panel: Distribution of depth differences between Antelope locations and the references ones. Bottom panel: Distribution of depth differences between Autopicker locations and the reference ones

we can implemented more in detail the AutoPicker procedure without the initial Antelope solution. In the final configuration the AutoPicker is used to rilevate the P- and S-phases, and then these P- and S-onset are associated

	P phases		S phases	
	Antelope	Autopicker	Antelope	Autopicker
Mean	-0.017	0.044	3.75	0.09
St.Dev	0.408	0.27	0.52	0.35
N° phases	298	356	16	178
Max value	2.69	1.76	4.78	1.769
Min value	-2.067	-1.242	3.047	-0.695

	HEPICENTRAL DIFF		DEPTH DIFF	
	Antelope	Autopicker	Antelope	Autopicker
Mean	5.05	3.5	4.36	4.95
St.dev.	3.27	4.44	2.51	3.44
N° events	38	43		

Figure 4.8: Summary of the differences between the Antelope and AutoPicker pickings (on top) and locations (on bottom)

through the use of the Antelope associator and localizator (Figure 4.10).

In particular, after the first location with Antelope, the new procedure read the waveform data and the origin time from the Antelope tables. These informations are transferred to the AutoPicker, which detects and determines the P- and S-onset, those are written in the detection and arrivals table of Antelope. Then Antelope's orbassoc process, using the AutoPicker phases, associates and locates the seismic events. This procedure wil be written in collaboration with the Department of Civil Protection, in order to make possible an installation of it at the Department for a quasi real time use.

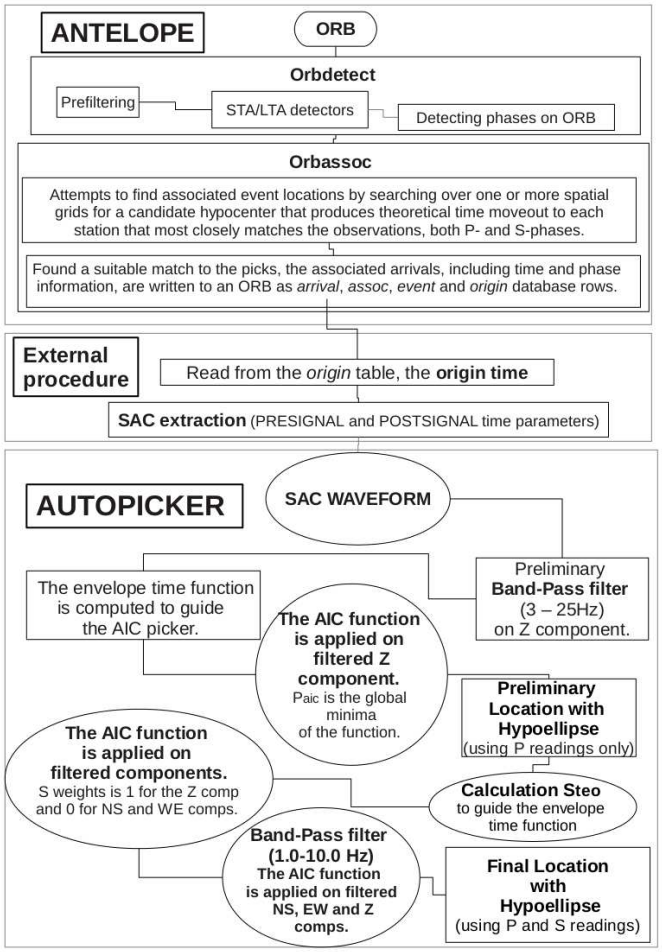

Figure 4.9: Description of the implementation of AutoPicker procedure in the Antelope ones.

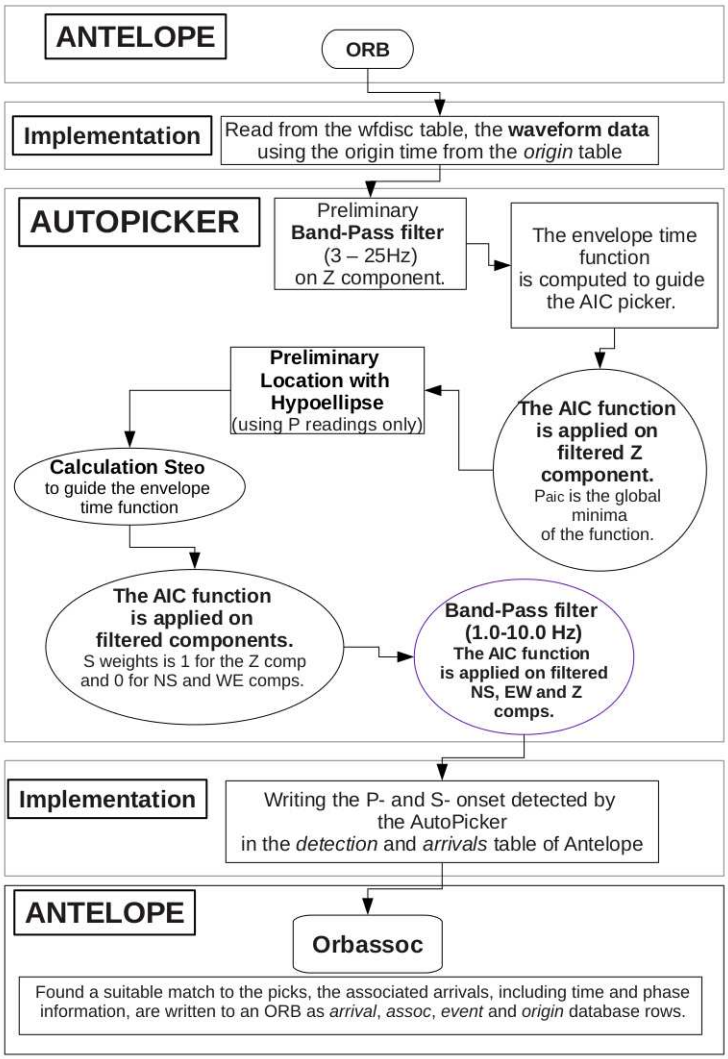

Figure 4.10: Description of the FINAL implementation of AutoPicker procedure in the Antelope ones.

Chapter 5

Travel-time tomography: Cat3D software

The travel-time tomography is a common technique to obtain a tridimensional velocity models and relative event locations, from P- and S- phases. In this study we have applied this methology to a limitated area so we are interested to a local earthquake tomography, which offers higher structure resolution respect the teleseismic ones; but it is limited by the maximum earthquake depths, in our study it is a crustal tomography (maximum depth 20 km).

The Cat3D is the software, powered by the OGS and distribuited by the PANEURA, used to product our travel-time tomography. This software is basically used for active seismology; in this study we apply it to a seismic sequence, so a passive seismology case of study.

In this chapter we introduce the theory of the travel-time tomography and the Cat3D algorithm [Cat3D user manual, 2008].

5.1 Local earthquake tomography (LET)

In this study we have used local earthquakes: the Emilia sequence occured in May-June 2012; this choice has inherent advantages and disadvantages compared with the controlled-source and teleseismic tomography. Two principal advantages, compared with the controlled-source, are the excitation of both compressional and shear-wave and their 3D spatial distribution. Compared with the teleseismic tomography, the local earthquake tomography (LET) offers much higher spatial resolution of structure, due to increased ray density sampling, higher wave frequency and closer station spacing. On the other hand, the depth of the local tomography is limited by the maximum earth-

quake focal depths in the area, while the depth of teleseismic tomography models can have the order of the array dimension (Aki [1982]).

5.1.1 Basic theory

The travel-time tomography requests to calculate the travel-times of the waves along a path, into the model. The body wave travel time T from an event i to a seismic station j is expressed using ray theory as a path integral:

$$T_{ij} = \int u \cdot ds \tag{5.1}$$

where u is the reciprocal of velocity, the slowness field and ds is an element of path length. The observations are the arrival times t_{ij}, where

$$t_{ij} = \tau_i + T_{ij}, \tag{5.2}$$

and τ_i is the earthquake origin time. The knows in the LET problem, are the receiver locations and the observed arrival times, both of which suffer some uncertainty. The source coordinates, the origin times, the ray-paths and the slownessess are the unknowns.

Given a set of arrival times t_{ij}^{obs}(times of first P and S waves), the calculated t_{ij}^{calc} are determined from equations 5.1 and 5.2 using as a priori informations: hypocenters, origin times and an initial structure model. The misfit between the observed and calculated arrival times are the residuals, r_{ij}:

$$r_{ij} = t_{ij}^{obs} - t_{ij}^{calc} \tag{5.3}$$

The residuals can be related to the desired perturbations to the hypocenter and velocity structure parameters by a linear approximation:

$$r_{ij} = \sum \frac{\partial T_{ij}}{\partial x_k} \Delta x_k + \Delta\tau_i + \int \delta u ds \tag{5.4}$$

This is the same fo P or S arrival times. For Thurber [1986], we have:

$$\frac{\partial T_{ij}}{\partial x_k} = -\frac{1}{V} \cdot \left(\frac{dx_k}{ds} \right)_{source}. \tag{5.5}$$

If we adopt any finite parameterization of the velocity structure, then equation 5.4 becomes:

$$r_{ij} = \sum \frac{\partial T_{ij}}{\partial x_k} \Delta x_k + \Delta\tau_i + \sum \frac{\partial T_{ij}}{\partial m_l} \Delta m_l \tag{5.6}$$

where m_l represents the L parameters of the velocity model. The last partial derivatives are line integrals along the ray-path reflecting the relative influence of each model parameter on a given travel time datum.

The LET goal is to improve the model parameters, both structure and hypocenters, by perturbing them in order to minimize some measure of the misfit to the data. This requires an iterative procedure.

After this general introduction to the LET theory, we present the algorithm, that we have applied to our data in this study.

5.2 Cat3D travel-time tomography

In detail, in this paragraph, we describe, the characteristics of the Cat3D procedure.

5.2.1 Wave choice and ray tracing

In our simulations we have chosen the diving waves. These one have a bent rays, as the arch of a circle; and they are determined by a velocity gradient of the layers beyond the surface, positive to the bottom 5.1.

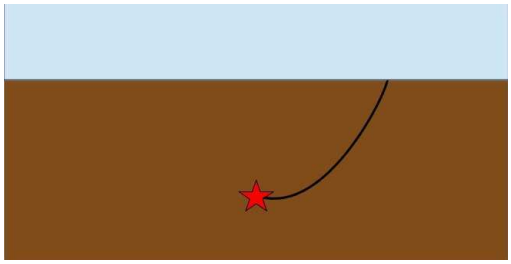

Figure 5.1: Example of a diving wave

The algorithm, used in the Cat3D software to calculate the path at a minimum time between two points (source and receiver), utilizes an iterative procedure, which works on single triple of points. These points represent the interactions of the ray with the velocity grid. The procedure is well described by the figure 5.2. The first hypothesis (fig. 5.2 on top left) is to consider a straight line between the source and the receiver, as ray. Then, starting from the source (or from the receiver), the algorithm takes into account the first triple of points of intersection of the straight ray (fig. 5.2 on top middle); in the middle point it calculates (point B) the displacement along the side, between the two pixels, using the Snell's law, considering the velocities of the two adjacent pixels. And then the procedure is the same with the second

triple of points, and so on in an iterative way. This work is applied on all the intersections of the ray, both belong to the pixels sides and belong to the interfaces of the horizons.

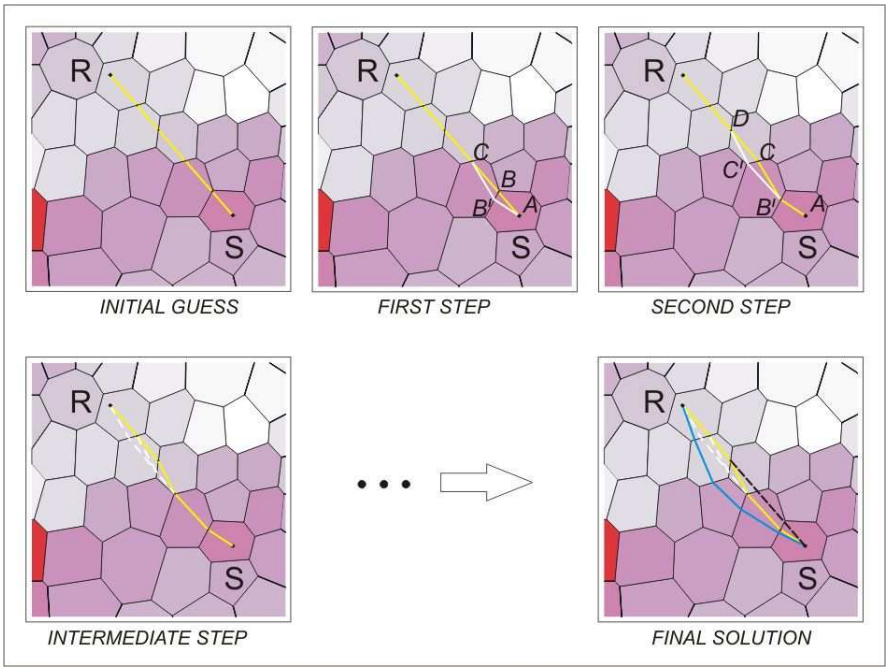

Figure 5.2: Iterative procedure of ray tracing with a minimum time in a generic grid. The pixel shape is the result of the adaptive grid, a technique not used in this study.

In figure 5.3 the algorithm of the minimum time is described in detail.

Given the triple points A-P-B, with A and B in two half planes separated by the plane R, the problem consists on find the path, which connects A to B in the minimum time, taking into account the two different velocities V_1 and V_2 of the two half planes. After the application of the Pitagora theorem, the time of the path A-P-B is:

$$F(x) = \frac{\sqrt{a^2 + x^2}}{V_1} + \frac{\sqrt{b^2 + (c - x)^2}}{V_2} \tag{5.7}$$

The next step is the calculation of the first derivative of this function, in order to find the minimum values:

$$F'(x) = [b^2 + (c - x)^2]x^2 - \frac{[V_1^2(c - x)^2(a^2 + x^2)]}{V_2^2} = 0 \tag{5.8}$$

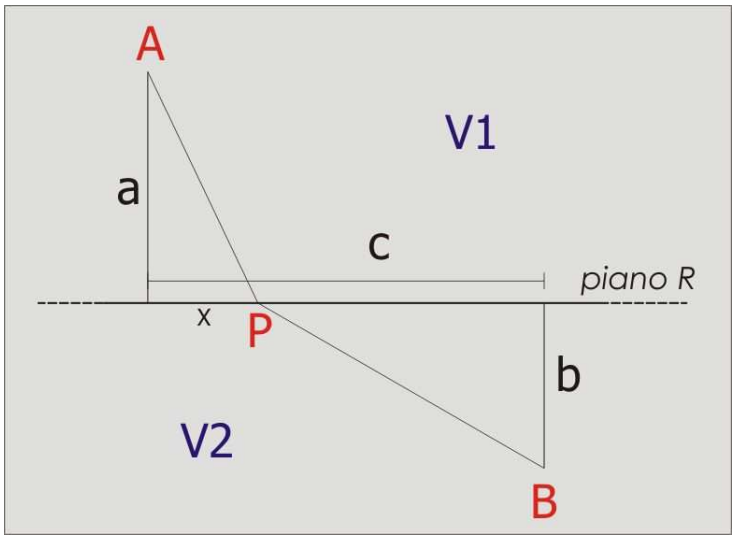

Figure 5.3: The triple of points for the determination of the minimum time

At this point using the bisection method, it is possible to find the x value, for which this function is zero (figure reffig:bisection), and then calculate the first derivative in this points in which the f' is zero so in $x = 0$, $x = c/2$ and $x = c$.

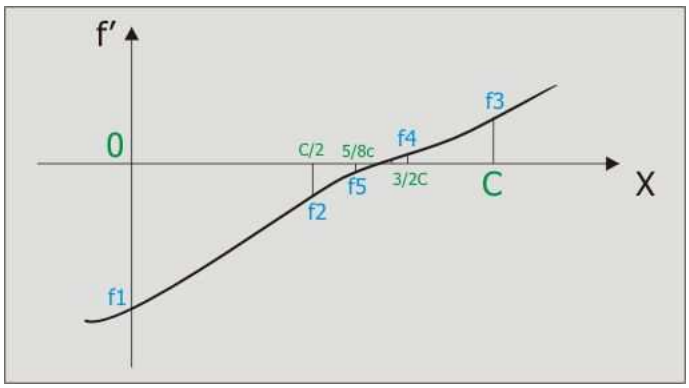

Figure 5.4: Illustration of the bisection method

After the verification, which one of the f' is zero, it is possible to eliminate the excluded value and then calculate a new value of the f' with the $x/2$ and so on, until an infinitesimal threshold is obtained. For the diving waves, the initial ray is defined by an arch, represented in a discrete way, from a set of ten straight segments. This number is fixed for all the archs, whereas the depth could be defined manually or automatically. For a manual define of the depth, it is calculated in base of the offset/depth ratio, this K number could

be chosen by the user (figure 5.5); this ratio is the same for every couple source-receiver of the acquisition. In the automatic way, the model must be defined in the interesting area by a vertical velocity gradient, otherwise the depth will be forced manually by the existing K factor. On this gradient the maximum depth of penetration of the arch is calculated from the Herglotz-Wiechert (Geldart and Sheriff [2004]).

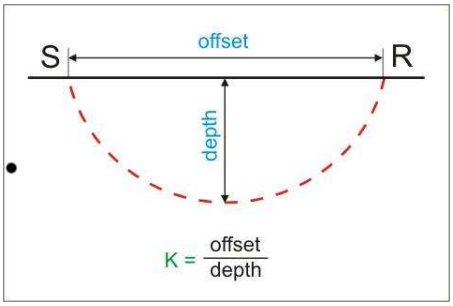

Figure 5.5: Rappresentation of the arch as initial path for the diving waves, in which the depth is function of the chosen ratio K.

In figure 5.6 it is possible to see all the parameters which have a role in the Herglotz-Wiechert formula, which is:

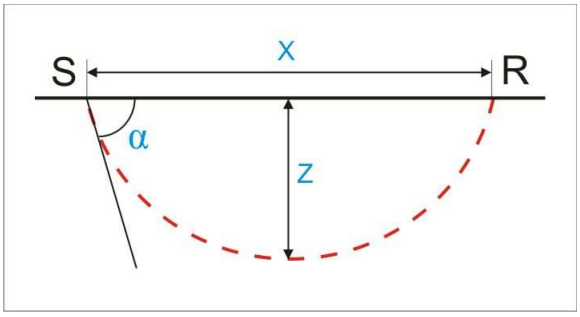

Figure 5.6: Illustration of the Herglotz-Wiechert parameters in the case of a diving wave

$$Z = \frac{V_0}{\Delta\nu}\left[\cosh\left(\Delta\nu\frac{t}{2}\right) - 1\right] \tag{5.9}$$

with V_0, as surface velocity and $\Delta\nu$ as velocity gradient in depth;

$$t = \frac{2}{\Delta\nu}\ln\left(\cot\frac{\alpha}{2}\right)$$

and

$$\alpha = \arctan\left(\frac{2V_0}{X\Delta\nu}\right)$$

5.2.2 Inversion method

In order to estimate the velocity field (inversion of arrivals time), we use the SimuItaneous Reconstruction Technique (SIRT) algorith. This method is an iterative process; in fact it is necessary to select the number of iterations to do (in this study, 100 iterations with straight rays and 2 with bent rays). The velocity of each pixel is upgraded at each iteration, considering all the rays, as average of the single values of velocity calculated for each ray passing through this pixel.

This is a series expansion method, where the investigating area is divided into elements with costant velocity (pixel or voxel). The ray, which connects the source to the receiver, is composed by many straight segments, so the wave propagating time from the point S to the point R is:

$$t^i = d_1 s_1 + d_2 s_2 + d_3 s_3 + ... + d_m s_m = \sum_{j=1}^{m} d_j s_j \tag{5.10}$$

where d_j is the single segment of the pixel j, s_j is the slowness in the pixel and m is the total number of the pixels in the model (figure 5.7).

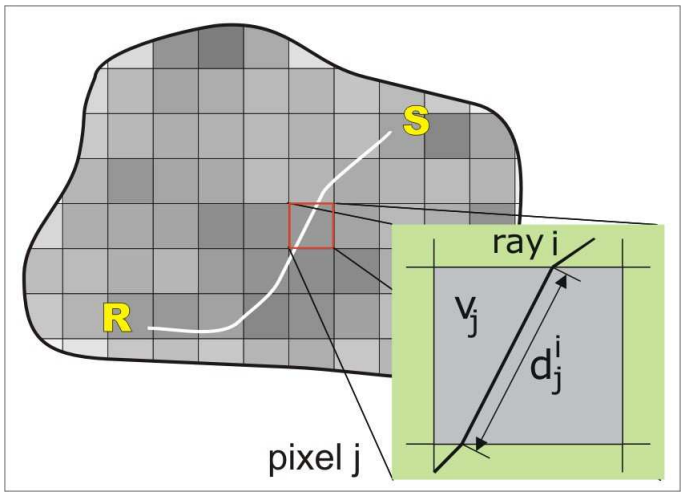

Figure 5.7: Discretization of the investigating area into regular pixels with costant velocity and representation of the ray into wave segment, propagating from S (source) to R (receiver)

To minimize the time residuals, the SIRT uses an iteration procedure of convergence of the searching solution:

$$\Delta s_j = \frac{1}{N} \sum \left(\frac{\Delta t^i d_j^i}{\sum (d_j^i)^2} \right) \tag{5.11}$$

where Δt^i is the residual of the i-th ray; d^i_j is the i-th ray segment of the j-th pixel; N is the total number of rays and M is the total number of pixels.

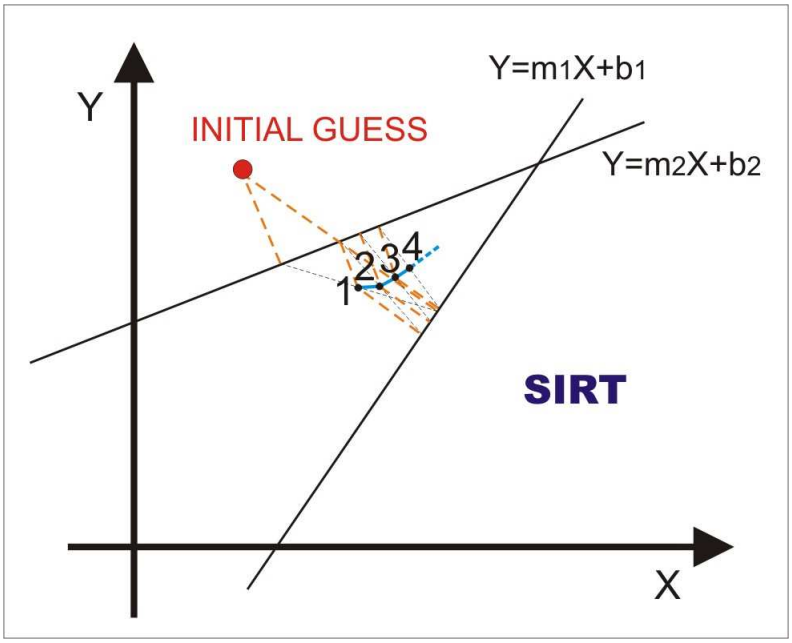

Figure 5.8: Schematic representation of the SIRT behavior in the reaserch of the intersection of two straight line. The SIRT is a slow method but with smooth solutions (Stewart [1993])

5.3 Attendibility of the inversion

The attendibility of the inversion could be measured in two steps. The first is about the attendibility of the tomographic system (model + ray density), the second concerns on the estimation of the errors through the use of the results analysis.

The attendibility of the tomographic system could be calculated in several methods: simple and fast, but less reliable as the angular coverage and the ray density; or complex and expensive in time and calculations but more correct as the null space map. The error estimation, as well, could be estimated in several ways as the analysis of the time residuals, with statistical studies.

5.3.1 Attendibility of the tomographic system

The solution of the inversion of the arrival times is equal as the resolution of this system:

$$\begin{aligned} t_1 &= a_{11}s_1 + a_{12}s_2 + a_{13}s_3 + ... + a_{1n}s_n \\ t_2 &= a_{21}s_1 + a_{22}s_2 + a_{23}s_3 + ... + a_{2n}s_n \\ t_3 &= a_{31}s_1 + a_{32}s_2 + a_{33}s_3 + ... + a_{3n}s_n \\ ... & \\ t_m &= a_{m1}s_1 + a_{m2}s_2 + a_{m3}s_3 + ... + a_{mn}s_n \end{aligned}$$

where t_i is the arrival time of the i-th ray, a_{ij} is the lenght of the segment of the i-th ray in the j-th pixel and s_j in the slowness in the j-th pixel.

The system could be expressed as:

$$t = \mathbf{A}u$$

where t is the vector of the arrival times, $\mathbf{A}$ is the tomographic matrix with the ray paths and u is the vector of the unknown parameters, e.g. slownessess.

The tomographic system could be defined as the set of the ray paths with the applied discretization, as the acquisition model.

The ray density, that is the number of ray which pass through the pixel, is the most popular and intuitive marker of local attendibility: the most higher is the number of rays, the most reliable is the solution in the analyzed pixel. This could be not so true in some particular cases, as a beam, even if it is copious, if it is composed by sub-parallel rays in a perpendicular grid. This system has low attendibility (high presence of null space) because of the linear dependence of the segments which compose the rays (figure 5.9), the tomographic solutions (velocity values) are infinite, because the ray paths inside the pixel are proportional to each other.

The most reliable and correct methodology to determine the attendibility of our tomographic system (presence of null space) is using the decomposition to singular values of the tomographic matrix $\mathbf{A}$. This matrix, in fact, could be decomposed into three parts:

$$\mathbf{A} = \mathbf{U}\mathbf{W}\mathbf{V}^T \tag{5.12}$$

where $\mathbf{W}$ represents the diagonal matrix of the singular values, $\mathbf{U}$ is the eigenvectors of the eigenvalues of $\mathbf{W}$ and $\mathbf{V}$ is the eigenvectors of $\mathbf{A}^T$. $\mathbf{U}$ and $\mathbf{V}$ are squared ortonormal matrices, so $\mathbf{U}^T\mathbf{U} = \mathbf{I} = \mathbf{V}^T\mathbf{V}$ (with I identity matrix).

The coloumns of the $\mathbf{V}$ matrix are the ortonormal base of the model space, so the summation of the elements squares v_i is equal to 1:

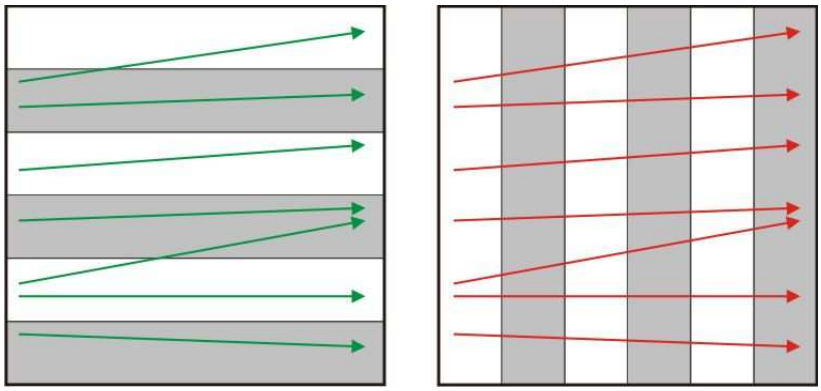

Figure 5.9: Two different discretizations of the model with the same rays dispositions. To the left the attendibility is lower than the other on the right

$$e_j = \sum_i v_{ij}^2 = 1 \tag{5.13}$$

The instability of the tomographic system is determined by the presence of singular values w_i equal or next to zero. After defining a threshold value, (below that the system is considered instable) it is possible to calculate the map of the null space in all the model, summing the squares of the elements of each coloumn of the V matrix (each coloumn refers to a pixel) equivalent to the singular values of the W matrix, which are below the threshold value. More this sum is near to 1, more the found solution (velocity) in this pixel will be not reliable, this means that the influence of the singular values on this pixel is high (high null space value). The rest of the sum, which is the complement value of the previous ones (near to 1), represents the positive value of the local attendibility of the system.

This is the null space map, the most efficient marker, which represents the quality of the inversion. It is to point out two fundamental aspects:

- high computational price; to calculate the scomposition of the singular values, it is necessary a lot of machine time, so much that for biggest tomographic systems could be not workable.

- The choice of the threshold value for the singular values. If this value is too high, the null space map will be much smooth and uniform; on the other hand a low threshold value with a small S/N ratio, could cause twisted informations.

The null space map is an efficient tool to work on the grid and, with a minimal modification, it is possible to reduce, substantially, the null space

map and to obtain a reliable tomographic system. In figure 5.10 there are four examples of reliability of the tomographic system; to the left the two examples of a bad conditioned system, and to the right the ones good conditioned. In general, the irregular geometries are the ones that best conditioned the systems.

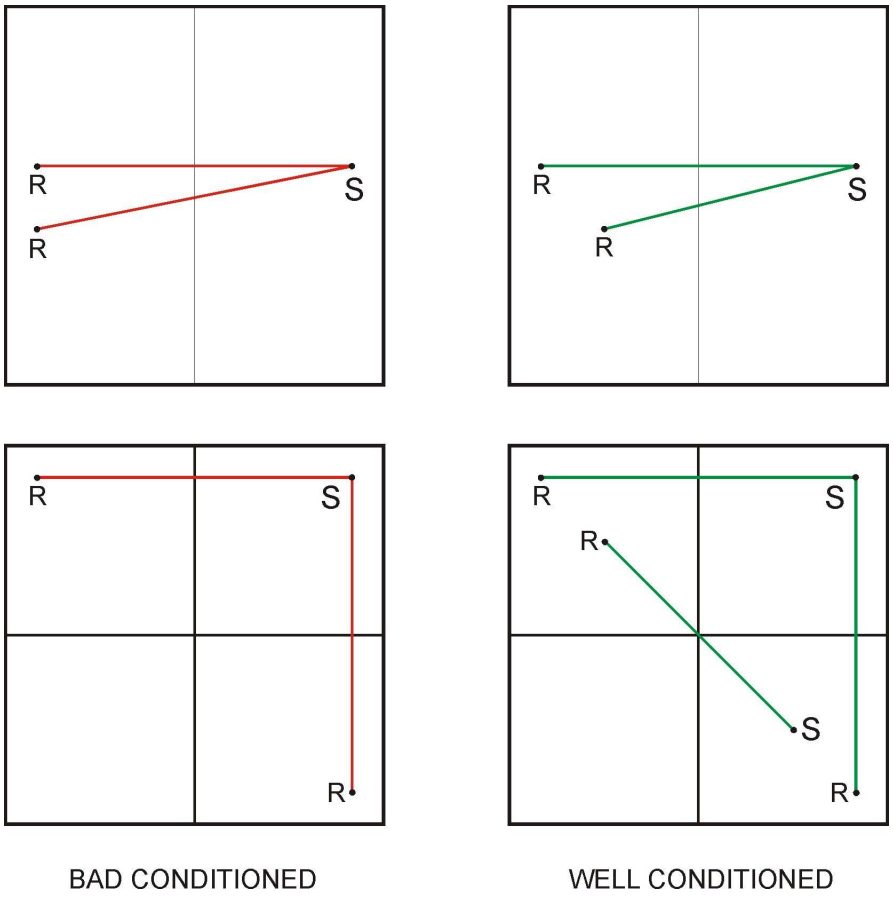

Figure 5.10: Examples of reliability of tomographic systems

5.3.2 Error estimation

In the inversion calculation for the travel-times tomography, a lot of variables are required, and many of them can influence the error estimation, as the picking errors, the location errors, numerical ray-tracing errors, the insufficient ray coverage and the presence of null space.

To taking into account all these quantities, and to valutate the inversion quality, besides the calculation of many statistical parameters (variance,

residuals rms, etc..), it is fundamental to define some quality controls (as QC panels), as the distribution of residuals in time, picking errors in the velocity, calculation of the ray coverage and the null space map. Here we describe these panels, that we have used during this study to verify the quality of our inversion.

Time

For the times, it is possible to calculate the residuals, as the differences between the calculated times from the final tomographic model and the observed times, also as percentage. We estimate the quality of the tomographic model with a unique value for all the data-set, for these statistical parameters:

$$rms = \sqrt{\frac{1}{n}\sum_{i=1}^{n} R_i^2} \tag{5.14}$$

$$average = \bar{M} = \frac{1}{n}\sum_{i=1}^{n} R_i \tag{5.15}$$

$$st.deviation = \sigma = \sqrt{\frac{1}{n}\sum_{i=1}^{n}(R_i - \bar{M})^2} \tag{5.16}$$

$$variance = \sigma^2 \tag{5.17}$$

$$skewness = y = \frac{1}{n}\sum_{i=1}^{n}[(R_i - \bar{M})/\sigma]^3 \tag{5.18}$$

with R, as the residual and n the ray number.

It is also possible to eliminate from the inversion of the arrival times, the ones that exceed a residual threshold (positive or negative) chosen by us. This was done at the start of the work in order to eliminate some picking errors or ray tracing errors.

Checkerboard test

The checkerboard test is one of the most popular test to check the inversion quality. It consists on the creation of a model, where the seismic velocities are alternated from high values to low ones, allocated in a checkerboard pattern, superimposed to the final model of the tomography. Using the same

acquisition geometry (sources and receivers) utilized for the inversion, it is possible to create a new set of travel-times, used, then for a new inversion. The ratio between the obtained velocity from this new inversion and the one producted with the original data, represents the map of the resolvability of the tomographic system studied. The checkerboard test could be done also, before the inversion, creating a set of synthetic travel-times directly from the checkerboard model and then analyzing the velocity field obtained from these data, starting from the costant velocity field. The values of the resolvability of the system could be calculated as the ratio between the true velocity and the one obtained from the inversion. For our study we have used this last method.

To prepare the checkerboard test with the Cat3D software, using the checkerboard model superimposed to the final tomographic velocities, it is recommended to use a regulare grid for the inversion of the data. The cells of the checkerboard model must be of the same type and with multiple dimension (each grid of the checkerboard model must be composed only an integer number of cell grid of the inversion).

5.4 Particular procedures: Staggered grids

In this work we have used the staggered grid method, because it allows us to obtain an image with a high resolution from the summation of several images with a low resolution but well conditioned in the tomographic system. The first step is to start from an initial grid , which can be the same grid used for the initial model or a regular grid defined directly from the tomographic parameters; from that grid, many other grids of the same type have been build; many as the chosen shifts on which are calculated the tomographic inversions. Any result of this shifts, is summed and averaged on an arranged regular grid or calculated automatically from the number of shifts and from the dimensions of the initial grid. This final grid will be regular as the initial one, but will result more dense and more resoluted for the velocity field, conserving an high tomographic reliability (see figure 5.11).After the choice of parameters necessary to the application, the method is automatically applied during the inversion procedure. It is recommended to choose a regular initial grid, especially in the case of a homogeneous distribution of rays in the investigated area. On the contrary an irregular grid is auspicable in the case of an irregular ray coverage, used for the inversion. In this case the shift paremeters must be manually added in the right way. In this study we have prefererred a regular initial grid.

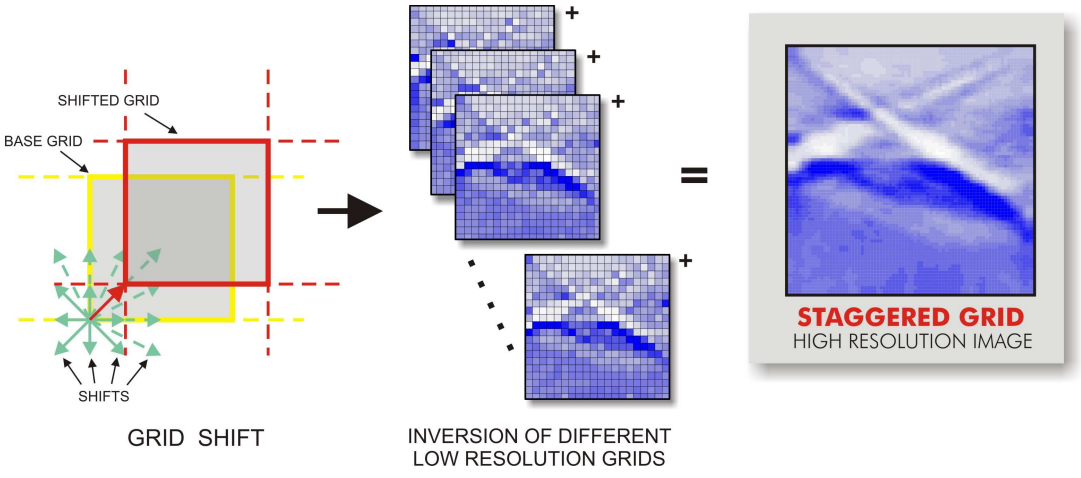

Figure 5.11: Scheme of the staggered grids procedure

Chapter 6

Travel-time tomography

In this chapter we describe the application of the travel time tomography in the case of the Emilia sequence May-June 2012. This area is really interesting beacuse it is characterized by a complex fault system (see figure 2.1). Because of the seismic sequence interests only a small part of this region (about $30x30\,km^2$ wide and 0-20 km deep). The investigated area will be limited to the upper crust. The travel time tomography and the event location are performed, respectively, using Cat3D software and NonLinLoc software through an iterative procedure. The main difference between active seismic and seismology are the unknowns in the tomographic system. In seismology the source location is an unknown parameter with high uncertainty, while in active seismic the source locations are well defined. In this study, the introduction of the source location in the tomographic system, could introduce uncertainties in the ray tracing and travel-times estimation.

6.1 Study of the tomographic problem

The reliability of the inversion, as explained in chapter 5, can be calculated in two steps. In the first one, related to the tomographic system (model + rays distribution), we computed the null space map of the model (see paragraph 5.3.1); in the second one we estimated the error by the time residual analysis.

To compute the null space analysis, we used the samegeometry of the real data (Figure 6.2) applied to a Vp velocity model defined by a general 1-D velocity function in depth (Figure 6.1).

Then we have calculated the null space maps for every layers of the grid; here we report the most significative results, at three different depths, which represent the layers that mostly influence the location of the events (figures 6.3, 6.4 and 6.5). At the surface and at 32 km, the pixels with high null

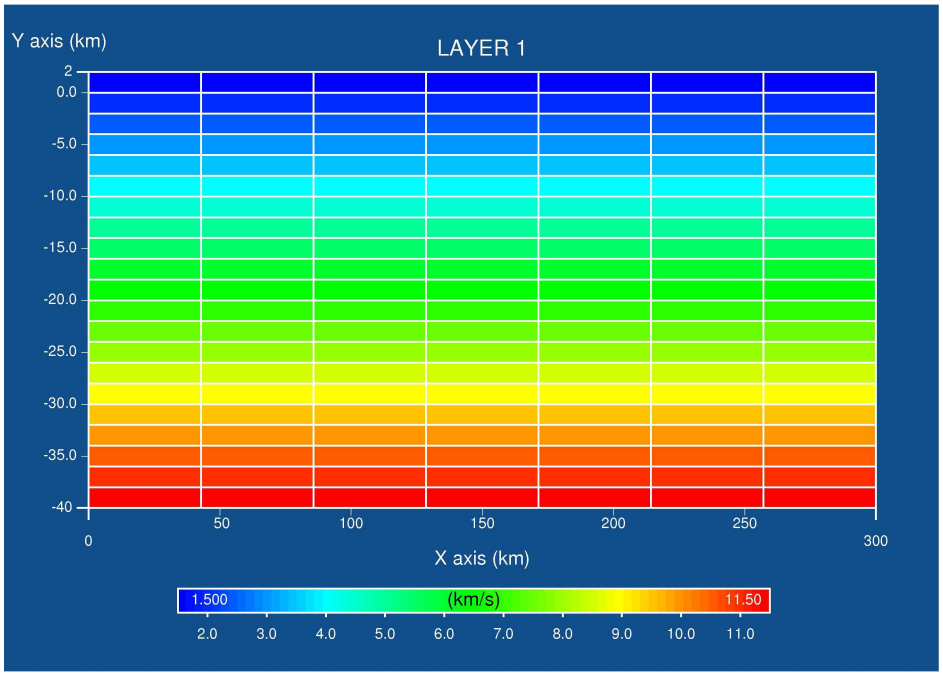

Figure 6.1: General Vp velocity model used to study the null space of the tomographic matrix

space (near to one), are predominant, so at these depths the tomographic solution is not reliable. Even at 32 kilometers of depth only one pixel can be considered reliable. At 16 kilometers, in the central part of the grid there are few reliable pixels, this is because, see figure 6.2, the events are located at the center of the grid. From these results we are obliged to choose an initial velocity model which is related to the area of study and not a general one as in this test (figure 6.1), because the null space is elevate and we need a realistic value of velocity in every pixel. In this study we have used 11 velocity models (see chapter 2), we report the elaboration and the results of only three of them. The three models chosen (figure 6.6)are those that have vertical errors lower than one kilometer, in the analysis described in chapter 2: Costa et al. [1992](MODEL 1); Massa [2012] (MODEL2) and Lavecchia et al. [in prep.] (MODEL 3).

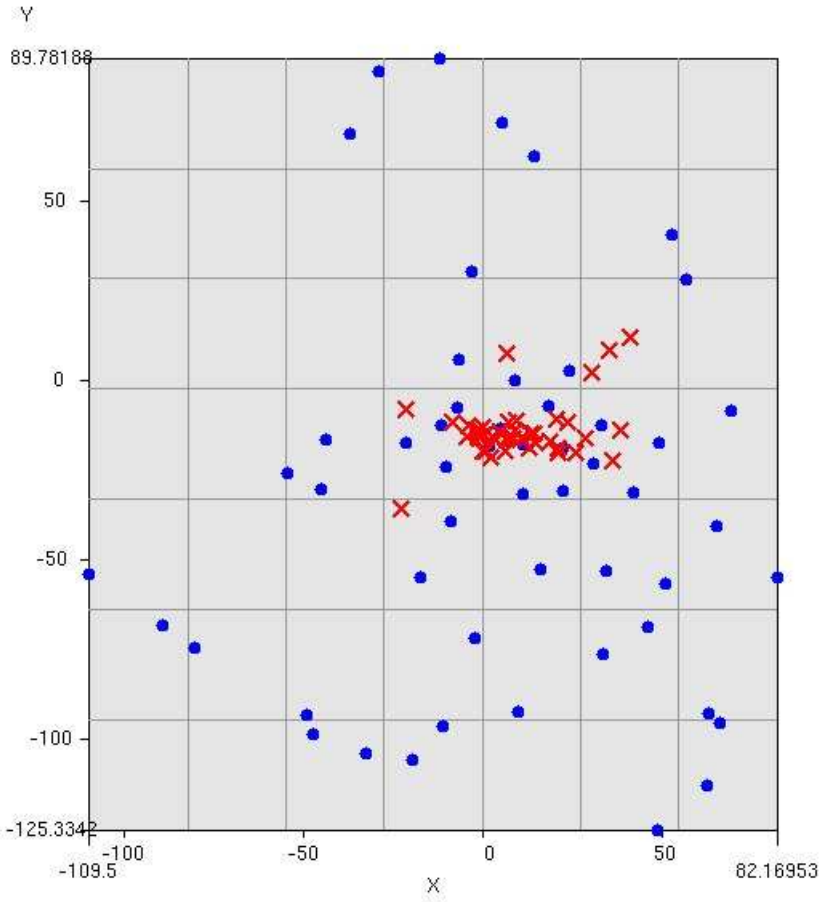

Figure 6.2: Map of the acquisition geometry used for the tomographic inversion. The red crossess are the event locations, the blue dots are the stations used in this study

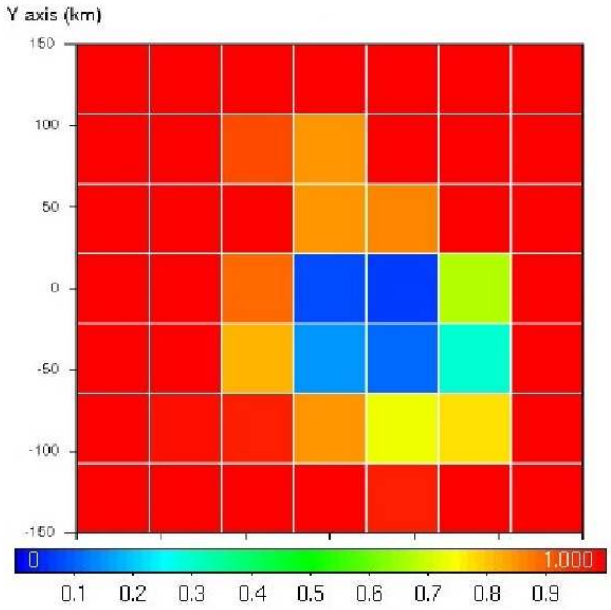

Figure 6.3: Null space map at 2 kilometers of depth

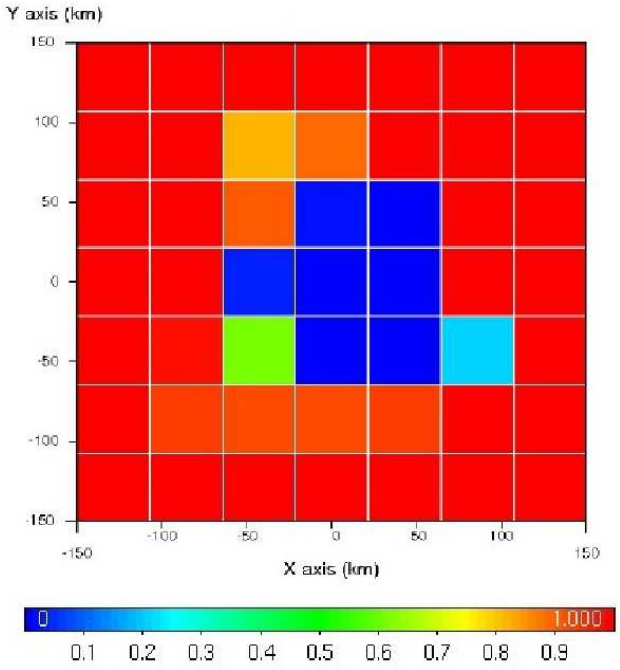

Figure 6.4: Null space map at 16 kilometers of depth

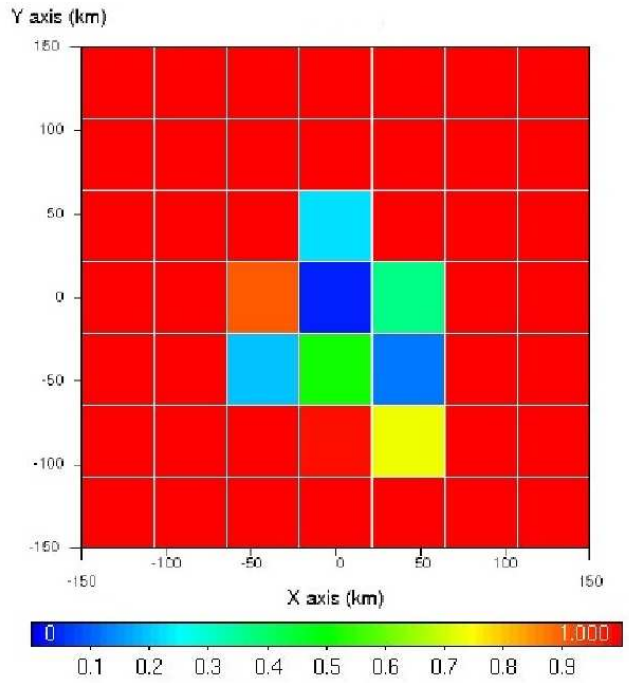

Figure 6.5: Null space map at 32 kilometers of depth

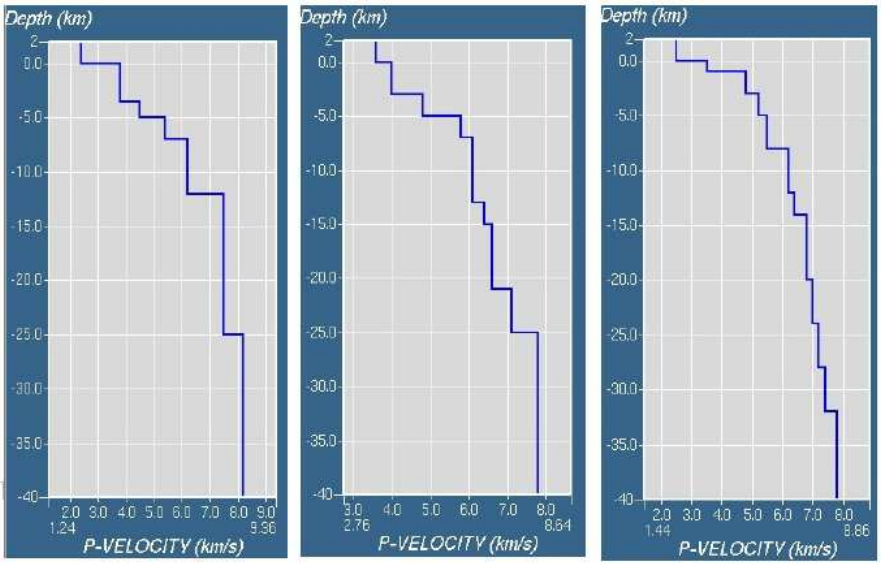

Figure 6.6: The three initial Vp velocity models: MODEL 1; MODEL 2 and MODEL 3 respectively from left to right

6.2 Choice of the horizontal grid and checkerboard test

For each of the three velocity models, we choose the grid step that present the lowest null space values (near to zero) (see paragraph 5.3.1). Here we show the results for MODEL 1:in figure 6.7 the null space map using a 6x6 grid; in figure 6.8, the null space using a 7x7 grid and in figure the 6.9, null space using a 8x8 grid. We take into account only the most significant four layers: layer 3 corresponds to 5 kilometers of depth; layer 4 to 7 kilometers; layer 5 to 12 kilometers and layer 6 to 25 kilometers. For MODEL 2 and MODEL 3, we used the same test, and we report the results.

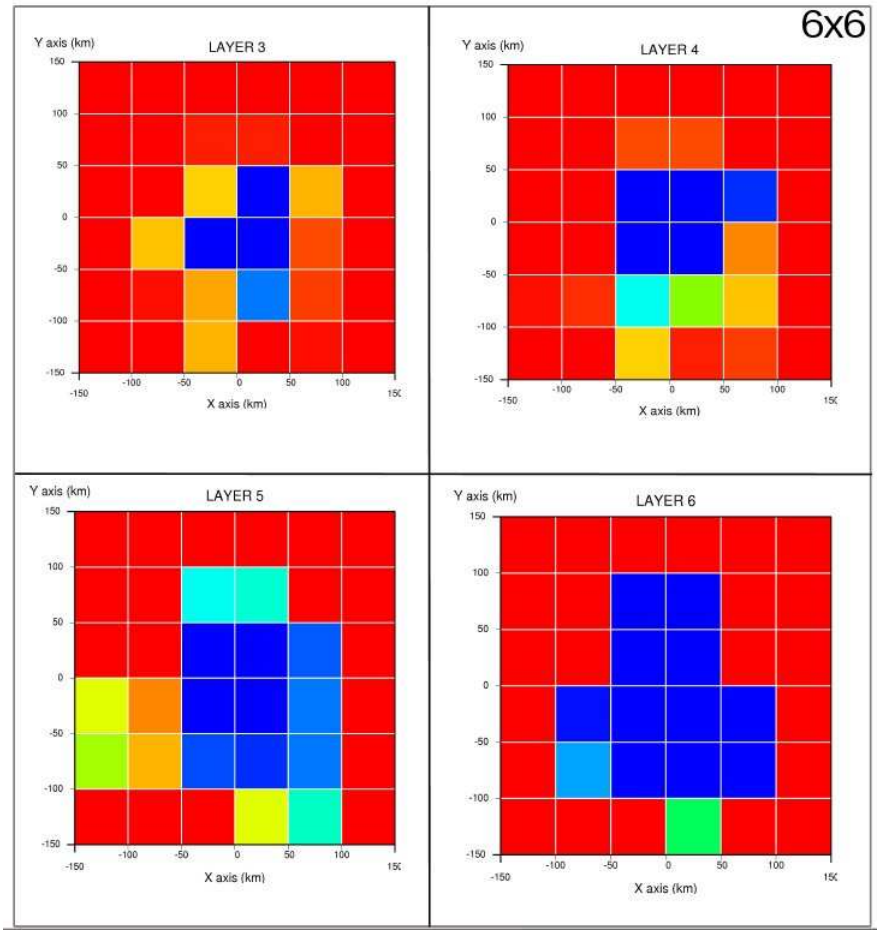

Figure 6.7: Null space map using the MODEL 1 Vp velocity model with a 6x6 horizontal grid

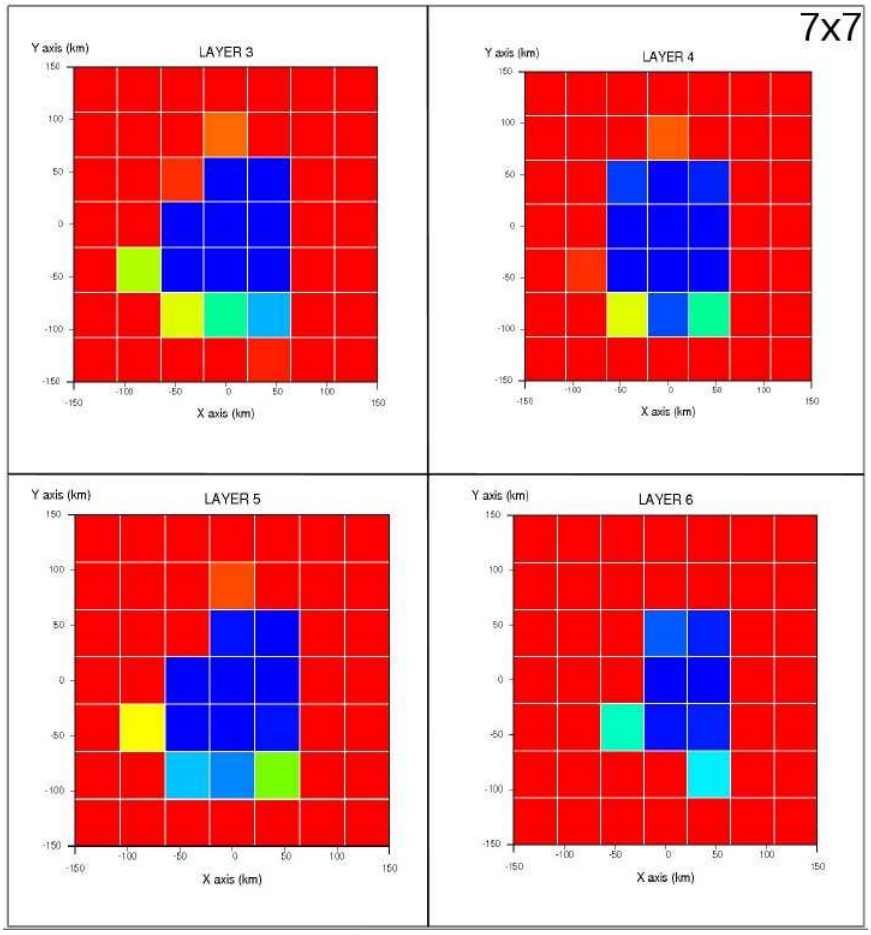

Figure 6.8: Null space map using MODEL 1 Vp velocity model with a 7x7 horizontal grid

For MODEL 2, the layers depths are: layer 3, 5 km; layer 4, 7 km; layer 5, 13 km and layer 6, 15 km (figures 6.10, 6.11 and 6.12).

For MODEL 3, the layers depths are: layer 4, 5 km; layer 5, 8 km; layer 6, 12 km and layer 7, 14 km (figures 6.13, 6.14 and 6.15).

Depending on this analysis for all the three velocity models we have chosen as favorite horizontal grid, the 7x7, because it is the best compromise between the resolution and the null space energy.

After that, we performed the checkerboard test (see paragraph 5.3.2) for each of the three models, in order to understand, at which depth and in which pixels the tomographic solutions are reliable with respect to the acquisition geometry used. Here we present the solutions of the checkerboard tests done for the three models considered at three different depths: 7, 15

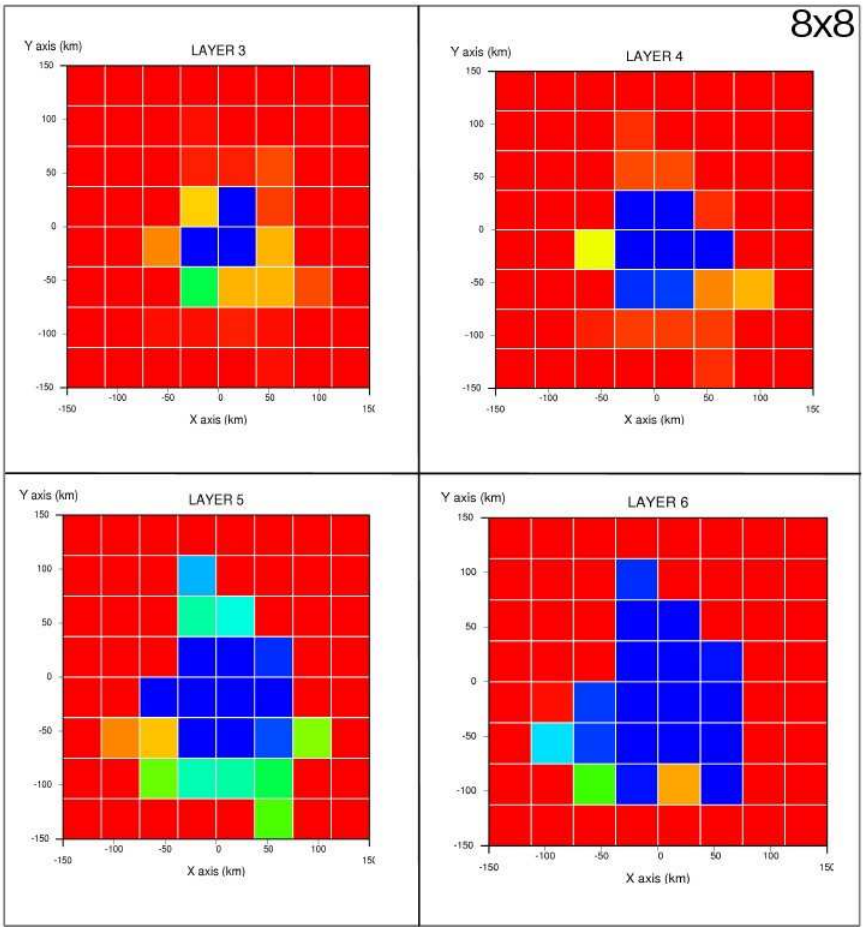

Figure 6.9: Null space map using MODEL 1 Vp velocity model with a 8x8 horizontal grid

and 32 kilometers (figures 6.16, 6.17 and 6.18). The first column represents the velocity model to reproduce, obtained summing and subtracting the 10% at the initial value. The second column displays the velocity model, obtained by the inversion of the travel times computed by using the model of the first column; and the last column shows the difference of the two first models, where white pixels represent difference close to zero.

From this analysis, the three initial velocity models have a checkerboard test really similar; so we present the tomographic results for all of them. It is to point out that our results will be reliable in the middle of the grid and at 5-15 km of depth, as we expect (our events are all located in the central part of the grid and with depths between 5 to 20 km).

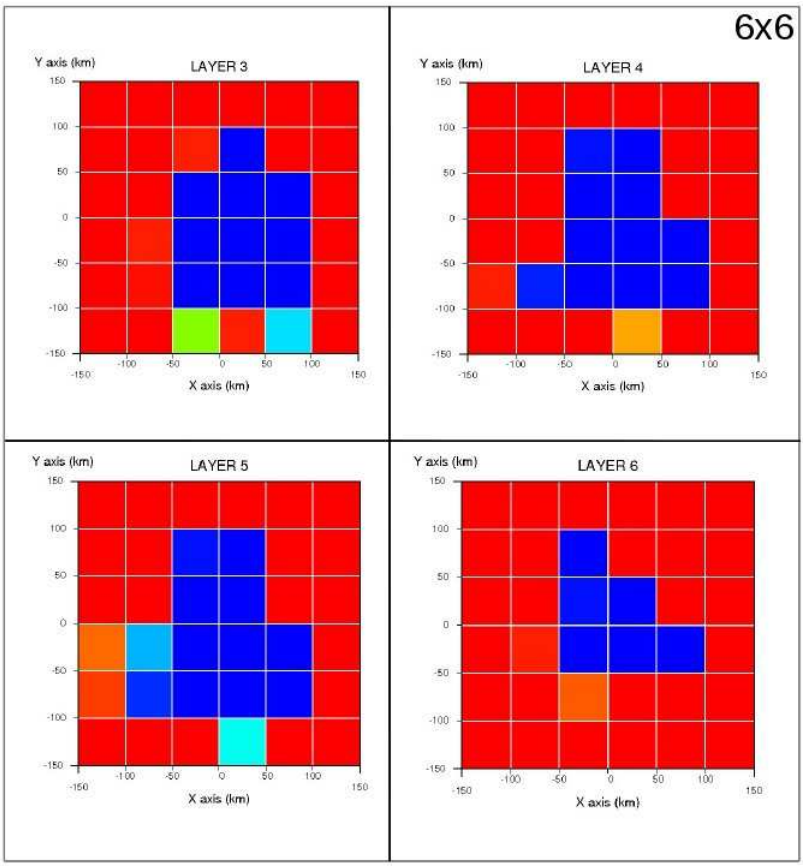

Figure 6.10: Null space map using MODEL 2 Vp velocity model with a 6x6 horizontal grid

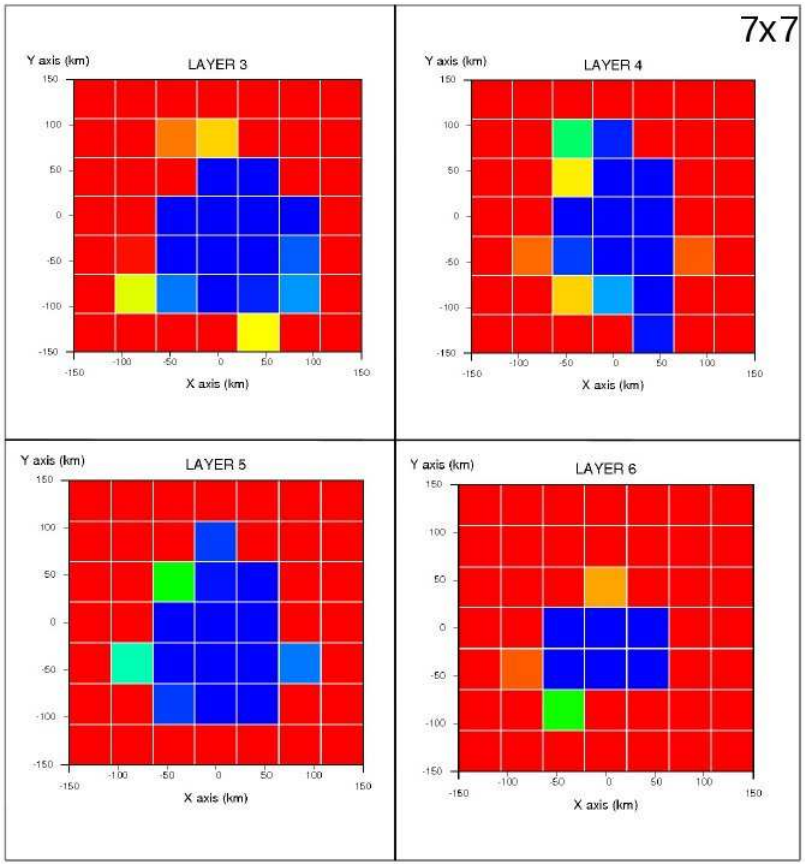

Figure 6.11: Null space map using MODEL 2 Vp velocity model with a 7x7 horizontal grid

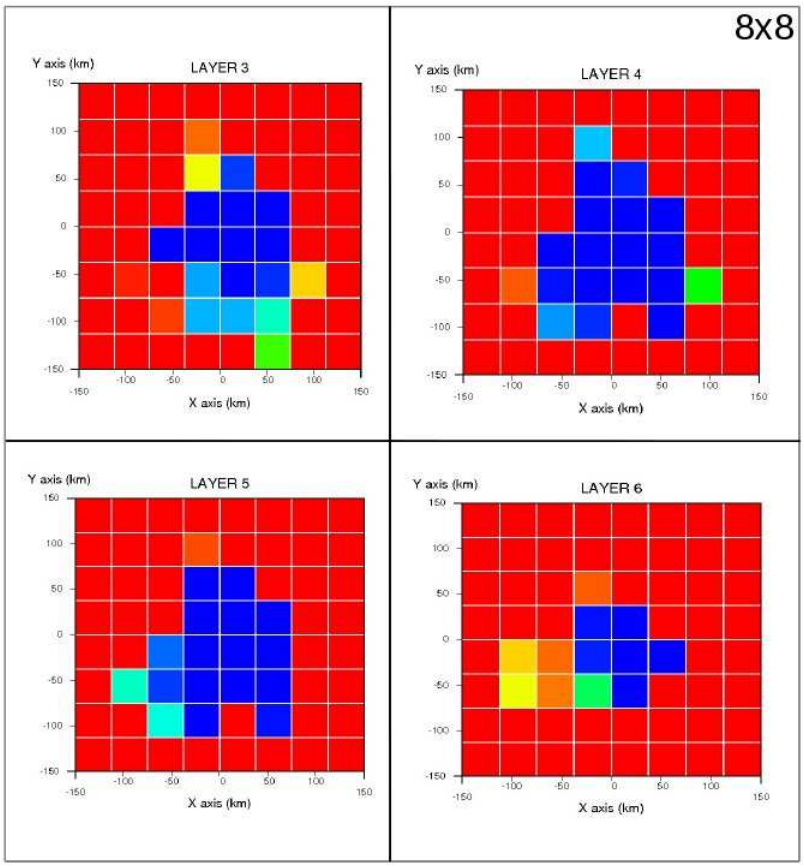

Figure 6.12: Null space map using MODEL 2 Vp velocity model with a 8x8 horizontal grid

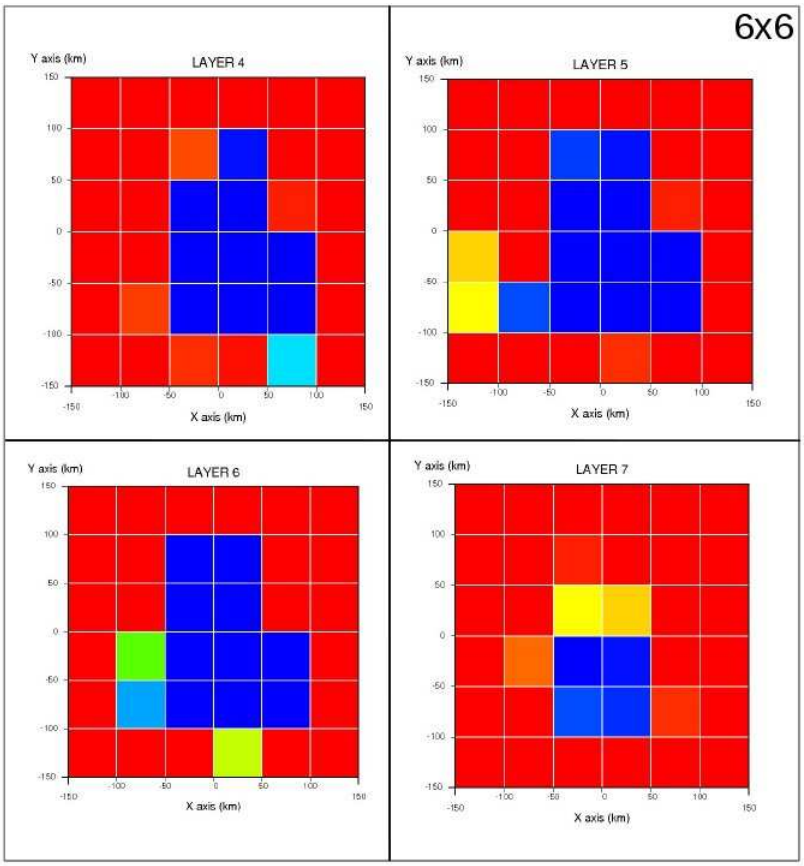

Figure 6.13: Null space map using MODEL 3 Vp velocity model with a 6x6 horizontal grid

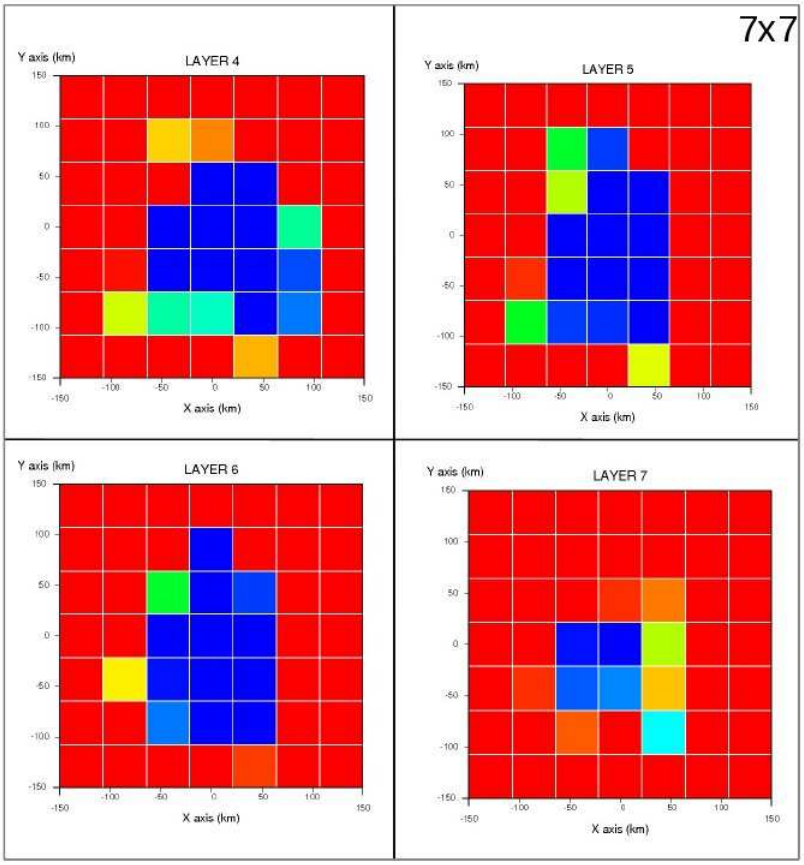

Figure 6.14: Null space map using MODEL 3 Vp velocity model with a 7x7 horizontal grid

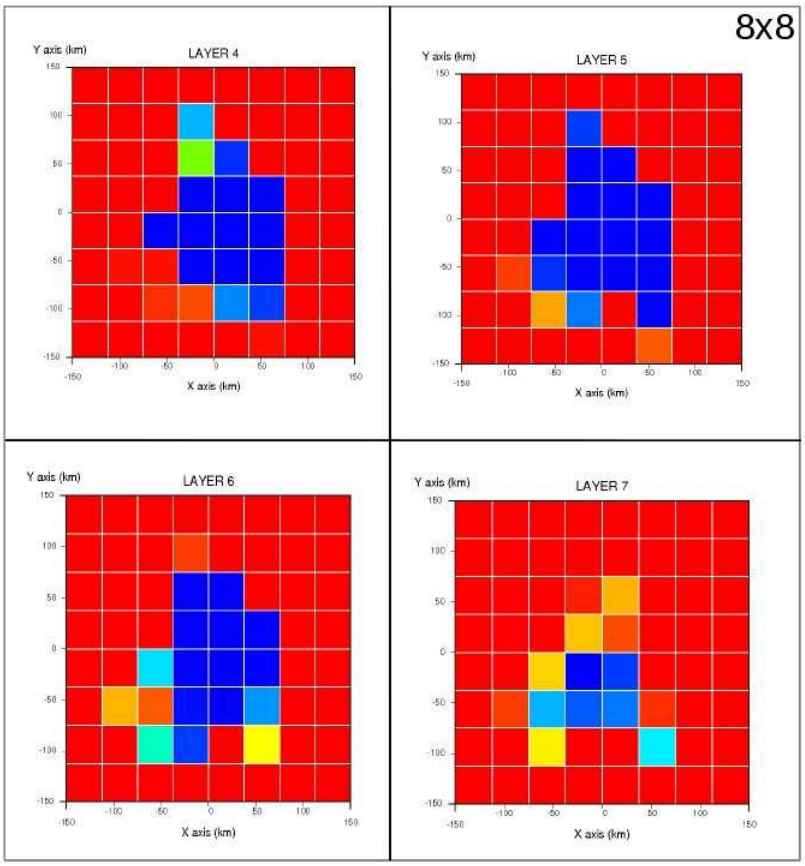

Figure 6.15: Null space map using MODEL 3 Vp velocity model with a 8x8 horizontal grid

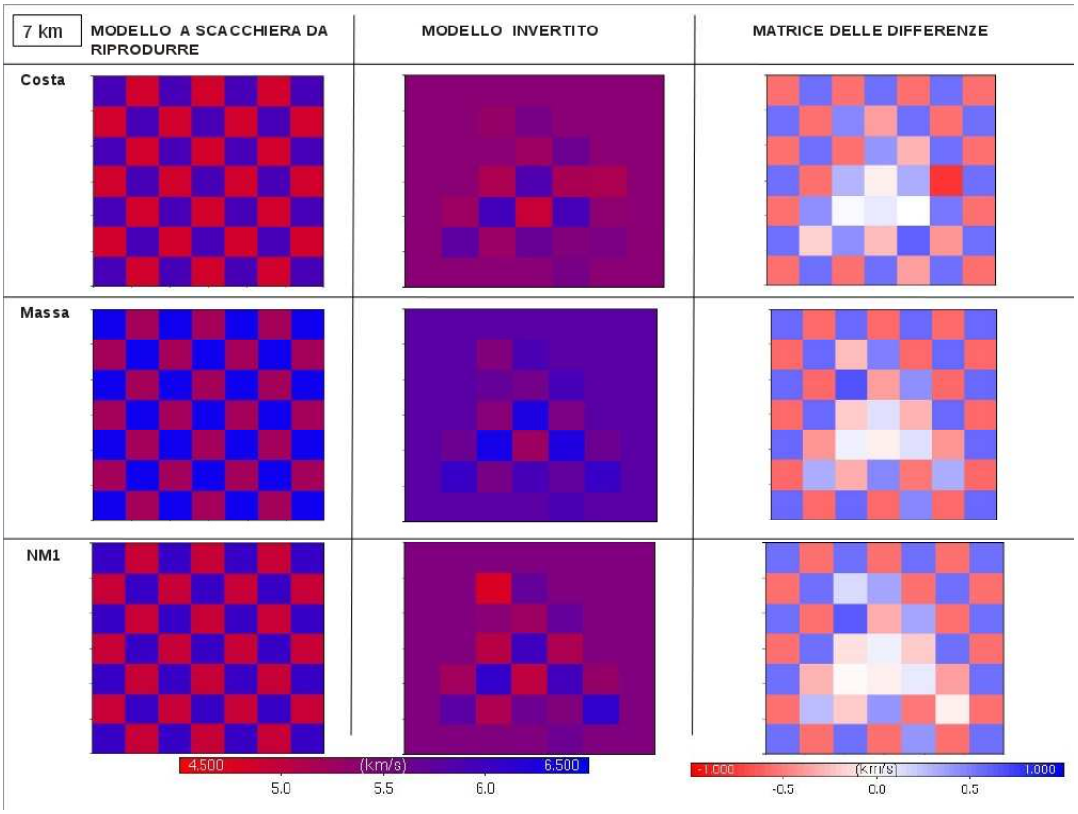

Figure 6.16: Checkerboard test for the three different velocity models at 7 kilometers of depth

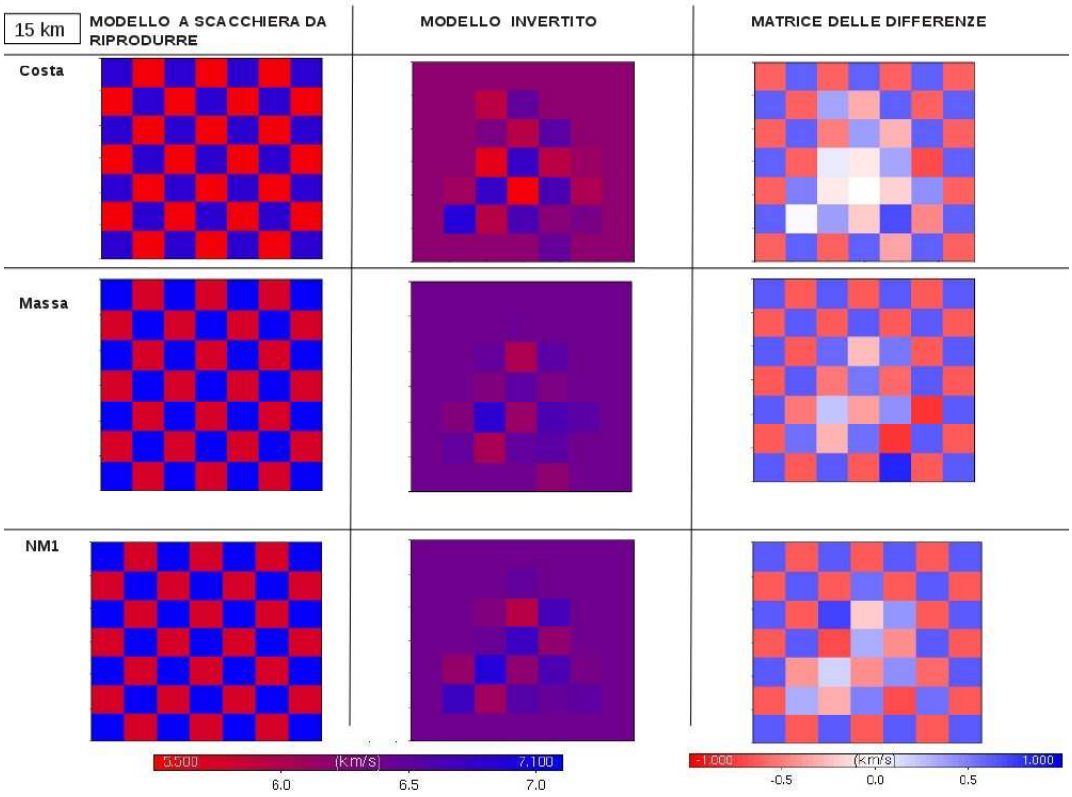

Figure 6.17: Checkerboard test for the three different velocity models at 15 kilometers of depth

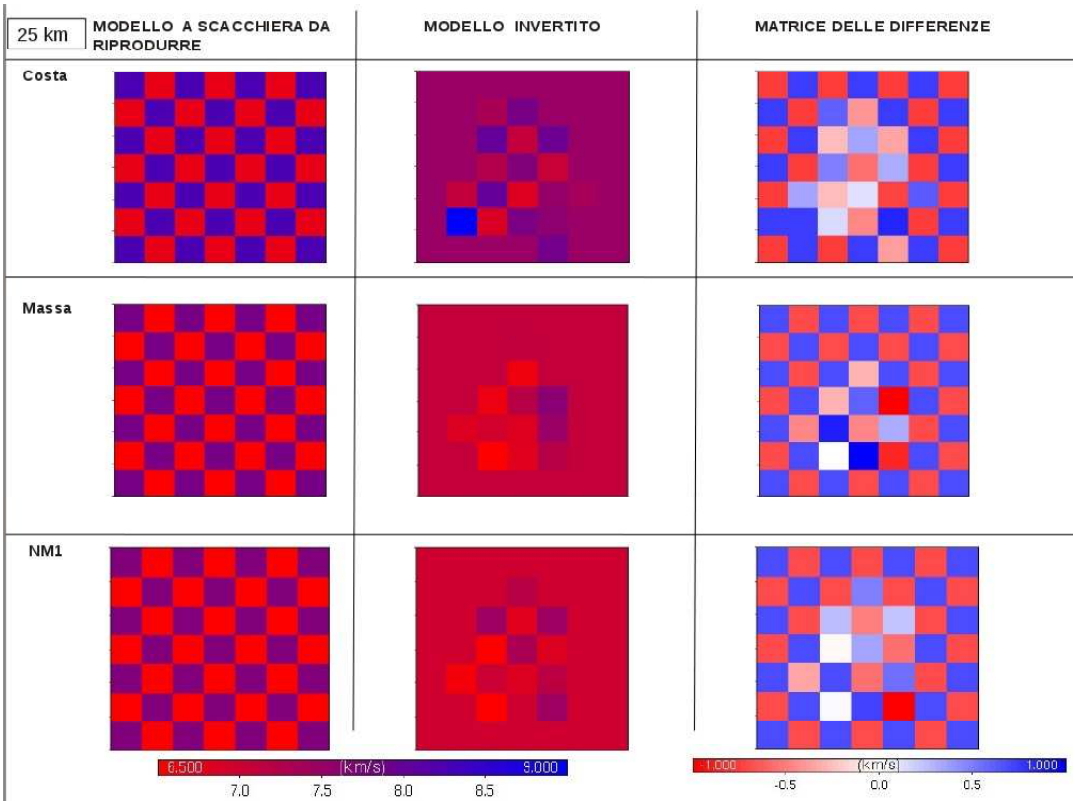

Figure 6.18: Checkerboard test for the three different velocity models at 25 kilometers of depth

6.3 Tomographic results

At each tomographic iteration, we have calculated the rms (root mean square) of the time residuals (the difference between computed and picked travel times) (figure 6.19). The solutions obtained from MODEL 1 are unstable and with the higher rms values than the other solutions. The best velocity model is the one from MODEL 2, which shows rms values lower than the others. We present the resulting velocity models of the inversion, reporting only the best iteration, with the lowest rms value in a vertical section, perpendicular to the event locations trand obtained (NWW-SEE) (figure 6.20).

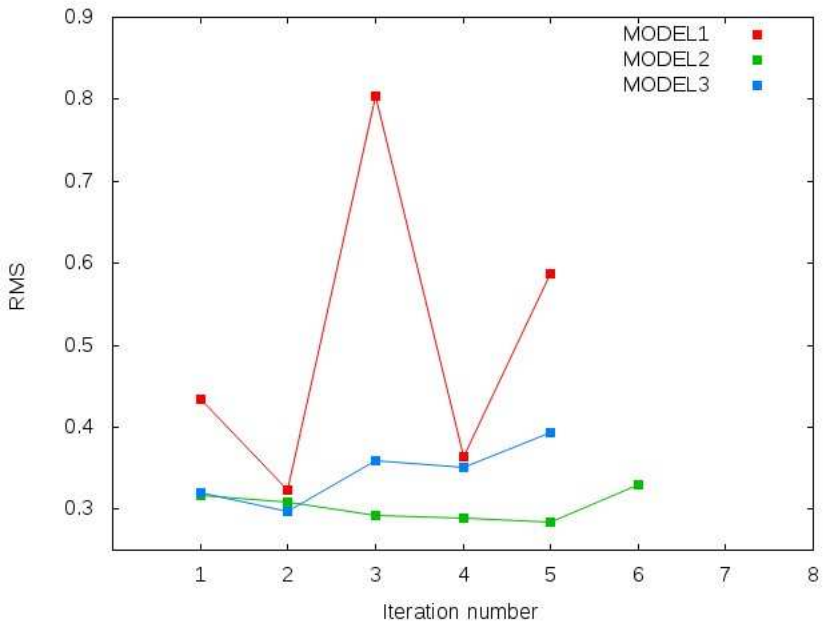

Figure 6.19: Root mean square values estimated at each tomographic iterations for the three velocity models: MODEL 1, red line; MODEL 2, green line; MODEL 3, blue line

We report the final results, represented by a vertical section of the Vp velocity volume by using the three different initial models: MODEL 1 (figure 6.21), MODEL 2 (figure 6.22) and MODEL 3 (figure 6.23). In all these images the white parts represent the zones not covered by the rays.

The tridimensional Vp velocity model (figure 6.21), with respect to MODEL 1 (figure 6.6 - on the left), presents: a thicker surface layer, characterized by low velocity values (0 - 3 km) and a deepest layer (13 25 km), where the velocity is considerably lower (about 5.5 km/s for the 3D Vp model and 7.3 km/s for the 1-D model).

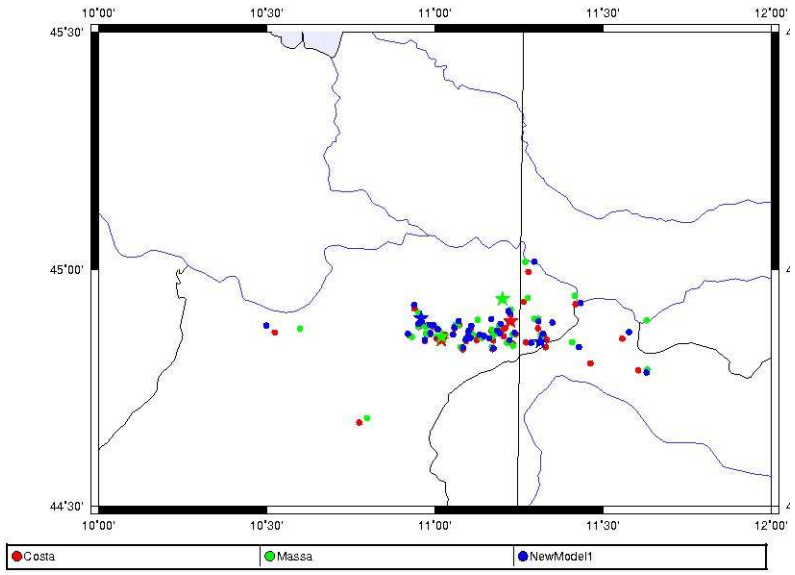

Figure 6.20: Maps of the located events, solutions of the lowest rms value iteration for each velocity models. The stars are the solutions for the main shocks, occurred the 20th of May, 2012 and the 29th of May, 2012. The black line is the section chosen by us to represent the resulting velocity models

The Vp velocity model, resulting from the travel-times tomography (figure 6.22), presents velocity values considerably lower (about 50% lower) than the initial MODEL 2 (figure 6.6 in the middle); in fact in the 3D model the Vp velocity values are about 2 km/s, in the 1D model, the Vp are 4 km/s. At higher depths the two Vp velocity models are similar.

As in the two previous case, the 3D Vp model (figure 6.23), obtained from MODEL 3 (figure 6.6 on the right), is characterized by a shallow lower velocity layer, with respect to the 1D model case. In the deeper layers, the velocities are similar in the two models (about 5.5 km/s).

From figures 6.21, 6.22 and 6.23, one can observe that these three tridimensional Vp velocity models are characterized by a surface layer (0 5 km) of low Vp velocity, about 1,8 km/s, and a thick layer (5 20 km) of 5.5 km/s .

Now we would like to analyze the Vs velocity models resulted by our tomographic study. As for the Vp tomogram, in all these images, the white parts represent the zones not covered by the rays.

The tomographic result from MODEL 1 Vs velocity model (figure 6.24) presents, as that one from MODEL 2 (figure 6.25) a shallow layer (0 - 3 km) of low velocity (about 1 km/s) and then a thick layer (3 - 13 km) characterized by a Vs velocity value of about 3.0 km/s. The tomographic results from

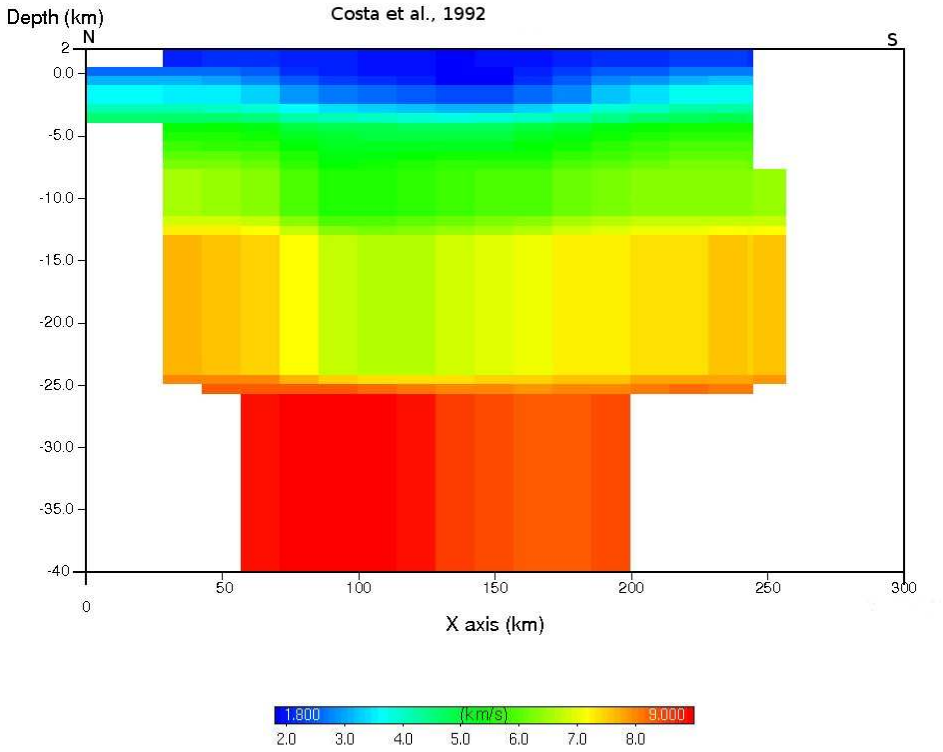

Figure 6.21: Vp velocity section resulting by the travel-time tomography, by using the MODEL 1 initial model

MODEL 3 Vs velocity model (figure 6.26) is similar to the other two, but it presents Vs values, at 4 5 km, lower than the other two models.

We calculated also the Vp/Vs values from each model: figure 6.27 from MODEL 1; figure 6.28 from MODEL 2 and figure 6.29 from MODEL 3.

Even if the Vp and Vs velocity models do not differ too much, the resulted Vp/Vs models are quite different from each other; a common characteristic is the presence at depths 5 - 10 kilometers of a discontinuity in the values of the Vp/Vs ratio, especially in the Massa [2012] solution in figure 6.28. It is necessary to complete this study with some more analysis with geological section to verify if this discontinuity correspond to the fault profile, but this is not matter of this study.

6.4 Location solutions

Another term that we can use to discriminate a velocity model with respect to another, are the events locations resulted from the whole inversion procedure

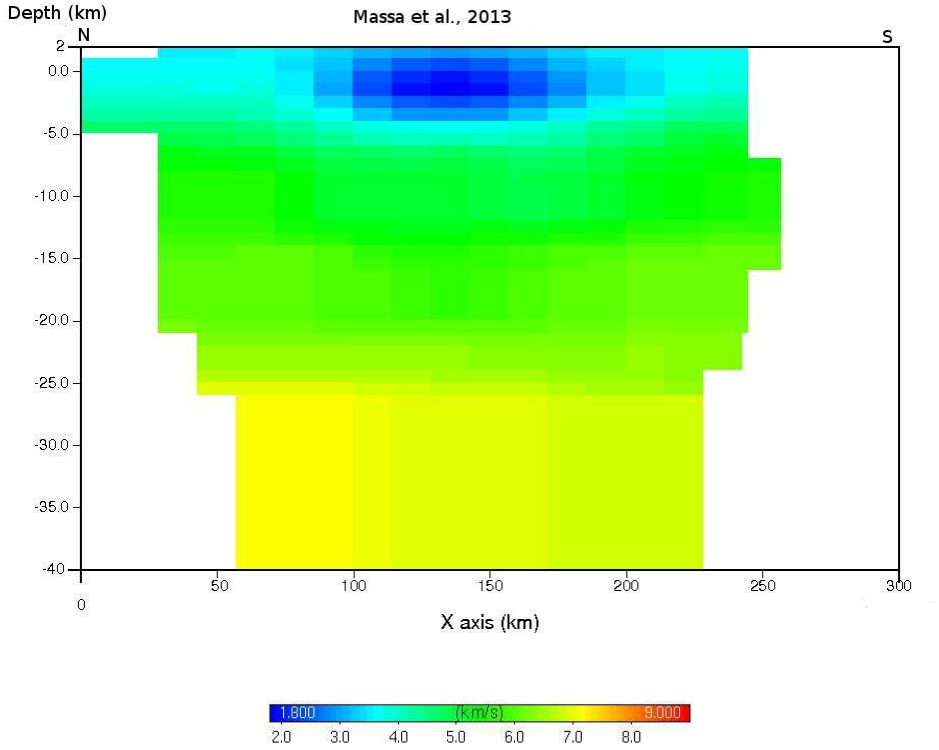

Figure 6.22: Vp velocity section resulting by the travel-time tomography, by using the MODEL 2 initial model

(tomography + events location). So here we present the solutions for the three velocity models in map (figure 6.30) and in section (figure 6.31).

The three set of solutions from the different velocity models are consistent in the error's range. The locations for the main-shock of the 20th of May, 2012 are more scattered respect the solutions for the 29th's. A possible reason could be the installations of temporary stations in the near field of the sequence after the 20th of May, 2012. So for the 29th event we have more waveforms than for the previous main-shock, and all of them in the near field of the earthquakes. For every events for the three velocity models, we have calculated the rms, in order to understand if it is possible to discriminate a velocity model with respect to another from the quality of the events locations. This study is presented in figure 6.32, and no velocity models are better or worse than the other two.

For MODEL 2 we presents a comparison between the events locations obtained using the 1-D velocity model and the events locations obtained using the tridimensional tomographic model in figure 6.33 and 6.34.

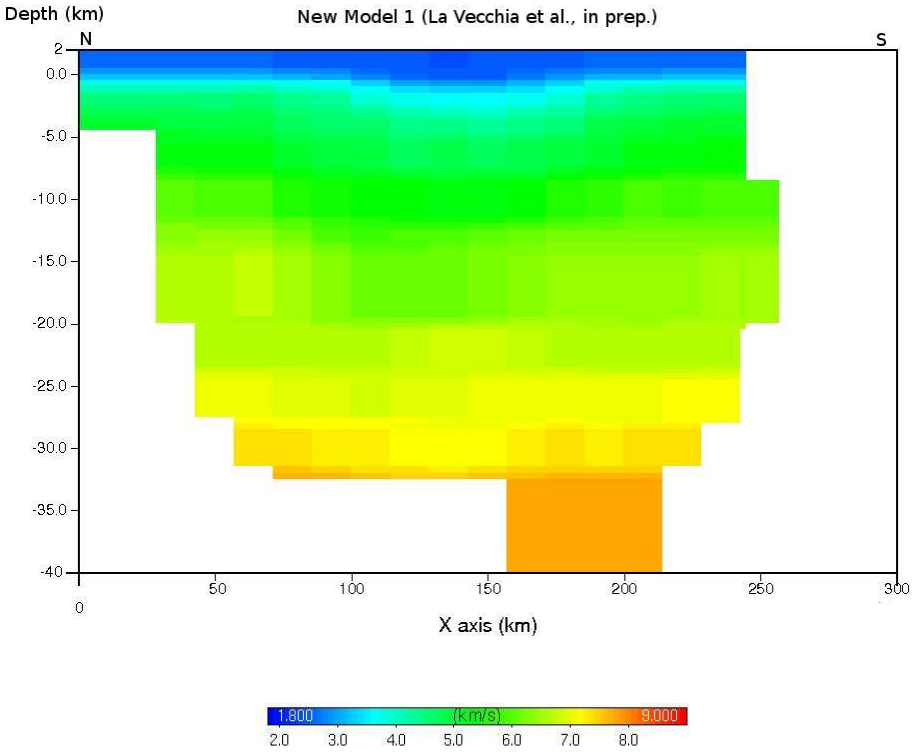

Figure 6.23: Vp velocity section resulting by the travel-time tomography, by using the MODEL 3 initial model

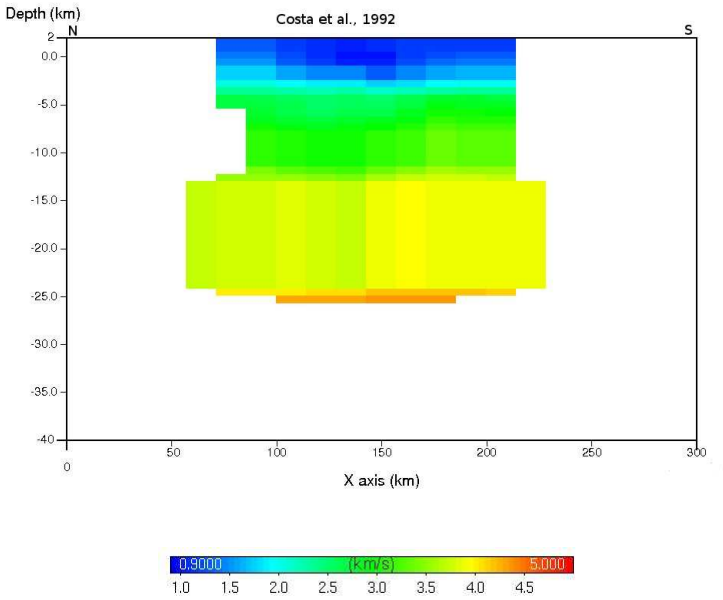

Figure 6.24: Vs velocity section resulting by the travel-time tomography, by using the MODEL 1 initial model

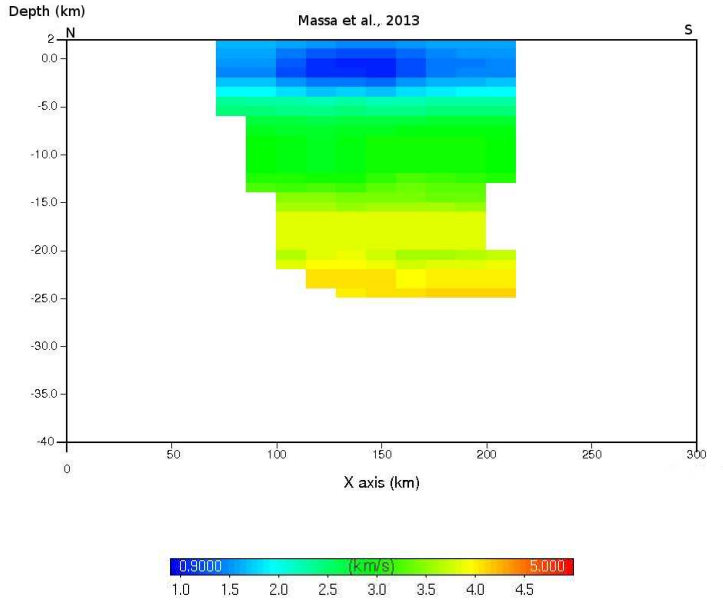

Figure 6.25: Vs velocity section resulting by the travel-time tomography, by using the MODEL 2 initial model

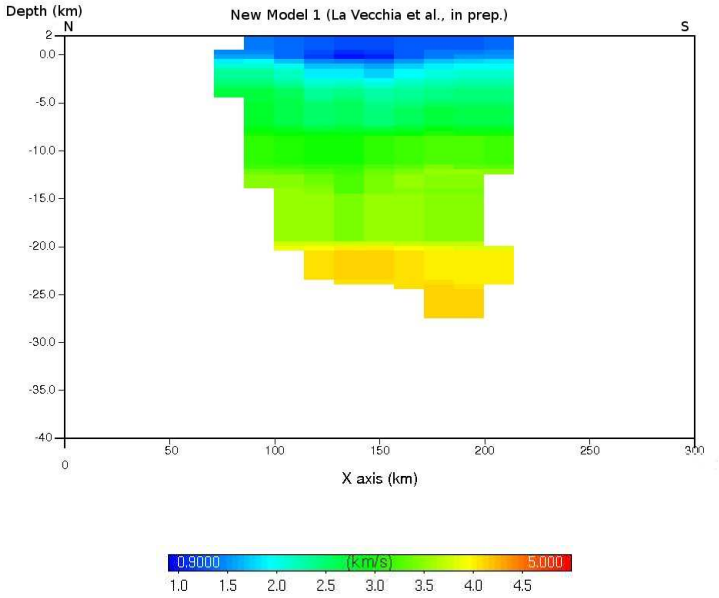

Figure 6.26: Vs velocity section resulting by the travel-time tomography, by using the MODEL 3 initial model

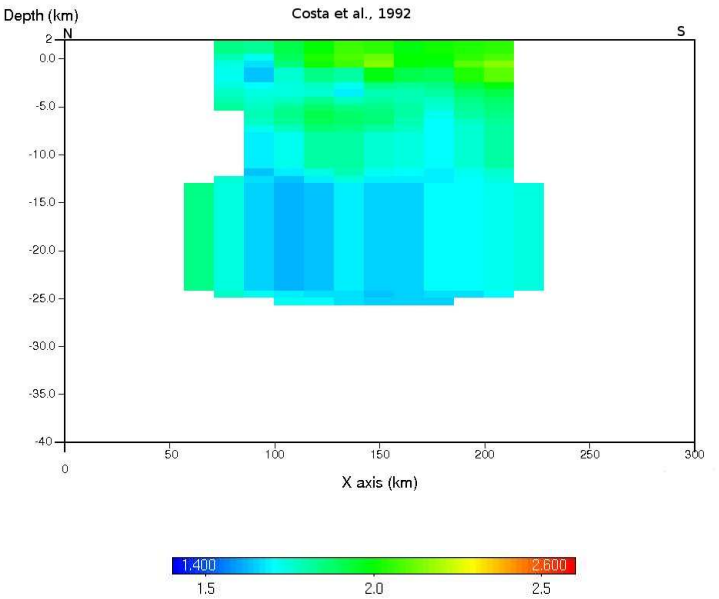

Figure 6.27: Vp/Vs velocity section resulting by the travel-time tomography, by using the MODEL 1 initial model

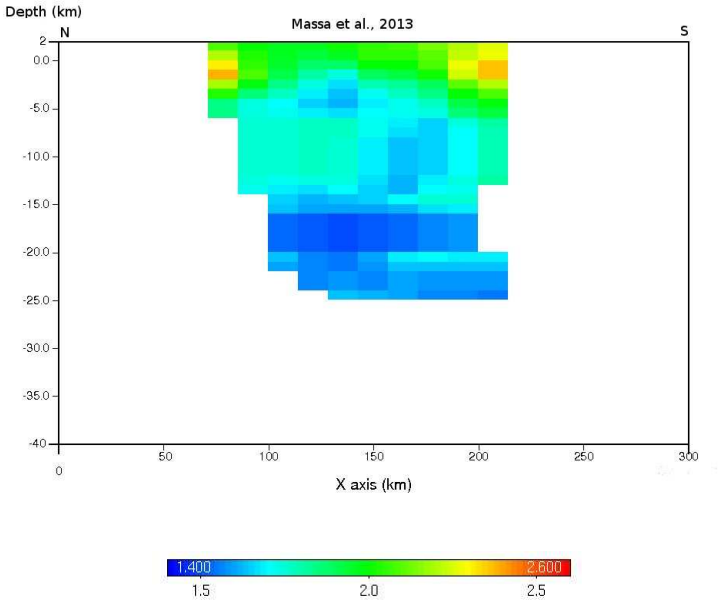

Figure 6.28: Vp/Vs velocity section resulting by the travel-time tomography, by using the MODEL 2 initial model

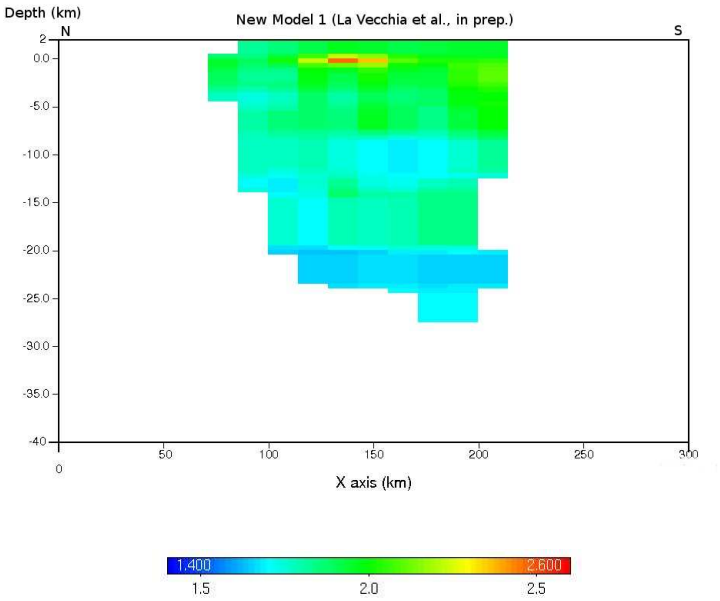

Figure 6.29: Vp/Vs velocity section resulting by the travel-time tomography, by using the MODEL 3 initial model

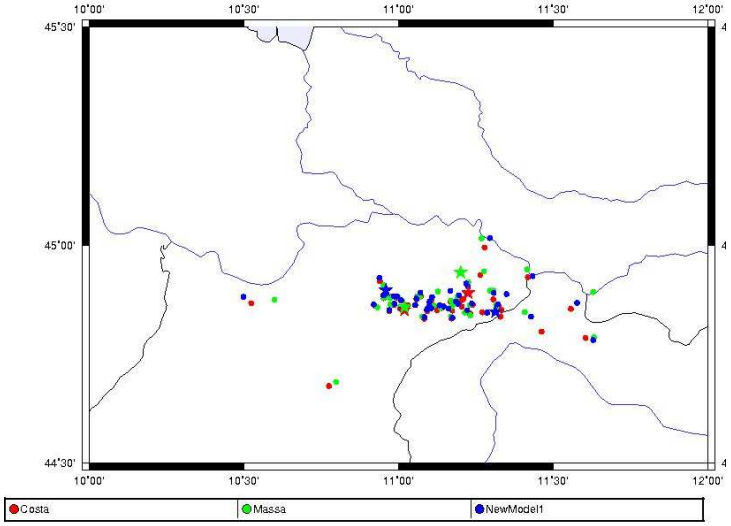

Figure 6.30: Map of the location events resulted from the tomographic inversion. In red the solutions from the MODEL 1, in green the solutions from the MODEL 2 and in blue the solutions from the MODEL 3. The stars are the locations of the two main-shocks: the 20th of May, 2012 (eastern solutions) and the 29th of May, 2012 (western solutons)

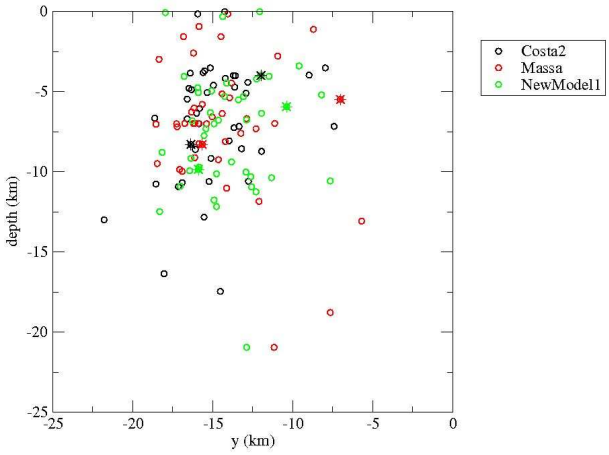

Figure 6.31: Location events resulted from the tomographic inversion, projected on a vertical section N-S of the model. In black the solutions from the MODEL 1, in red the solutions from the MODEL 2 and in green the solutions from the MODEL 3. The stars are the locations of the two main-shocks: the 20th of May, 2012 (eastern solutions) and the 29th of May, 2012 (western solutions)

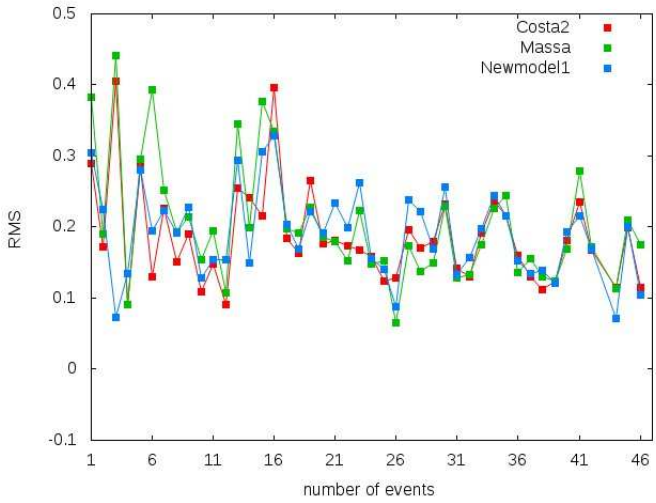

Figure 6.32: Rms values calculated for every located events for the three velocity models: red from the MODEL 1; green from the MODEL 2 and blue from the MODEL 3

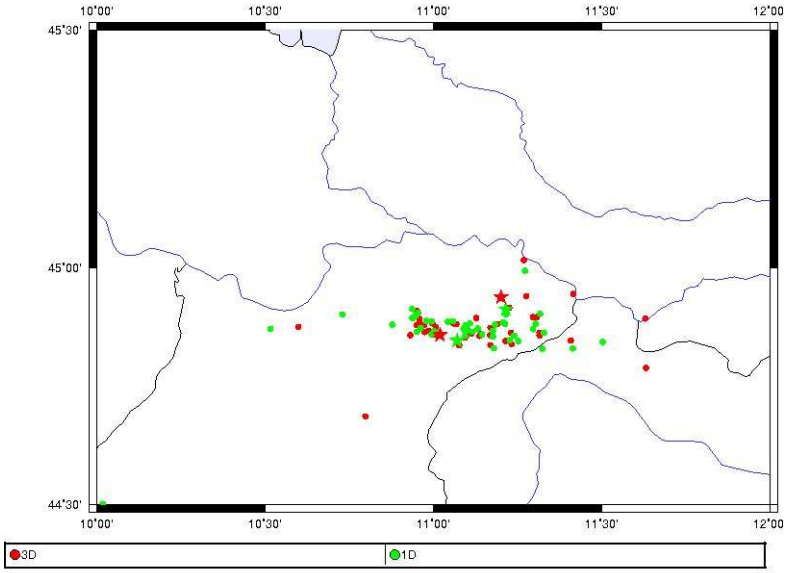

Figure 6.33: Map of the events locations resulted by using MODEL 2 velocity model (green dots) and the tomographic results of it (red dots) . The stars are the locations of the main events: 20th of May on the left; 29th of May on the right

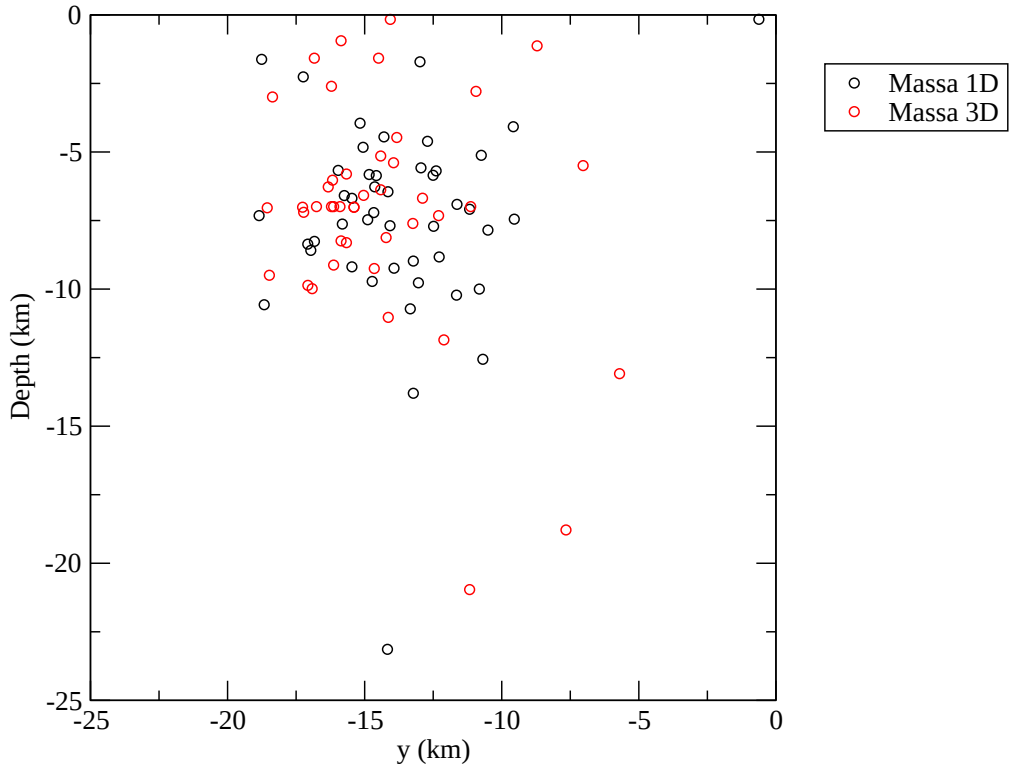

Figure 6.34: Section (N-S) of the events locations resulted from the tomographic inversion. In black the solutions from MODEL 2, in red the solutions of the tomographic velocities by using MODEL 2

In figure 6.33 the events locations from 3-D tomographic models seem to be less scattered than those one computed from the 1-D ones; otherwise the locations of the two main-shock events seem to be quite similar. In depth, figure 6.34 the two set of solutions do not differ in a significative way. Probably we need more data to determine the different quality of these two methods.

6.5 Conclusions

We have applied the Cat3D software at the Emilia sequence occurred in May-June 2012. As initial velocity models, we have chosen those ones, that have vertical errors lower than one kilometer, as shown in the analysis described in chapter 2, as Costa et al. [1992]; Massa [2012] and NewModel1 (Lavecchia et al. [in prep.]). The Vp and Vs velocity models resulted from the tomography are comparable but not equal. The events locations are consistent with

bibliography and with the solutions found in chapter 2. It should be necessary compare our results with geological informations, in order to better comment the results, but this is not matter of this study.

Chapter 7

Automatic and manual traveltimes tomography

With the improvement of seismic networks and the possibility to storage an hugh amount of data, it is necessary to produce big databases and to have a rapid access to the data and to rielaborate them in real time o quasi real time mode. For big databases, the manual picking is an onerous work, which requires a lot of time. The possibility to have a good quality automatic tool for phase recognition and picking, which produces similar results from tomographic inversion by using manual phases picking, could be convenient and useful. For this reason, we have compared two different travel time tomographies made with the same technique of the previous chapter, which differ only from the input phase files: the first one obtained from manual pickings, and the second one from the automatic AutoPicker pickings of the Emilia sequence, previously studied. This test is done to analyze and compare the different results: locations and velocity models, in order to study how much the location's errors influence the tomography's errors.

7.1 Input Data

The initial velocity model chosen for this test is that one proposed by Massa [2012], because in the analysis described in chapter 6, this model resulted to have the lowest rms values and it produced the most stable solution between the three models considered. The two different input data differ only from the input phase files: one are the manual pickings used in the chapter 22 (model A), and the automatic pickings (model B), obtained applying the AutoPicker algorithm to the Emilia sequence (see chapter 4).

7.2 Tomographic results and comparison

We have applied the same procedure as in chapter 6. We compared the rms time residuals computer for each tomographic iteration by using the model A and the model B.

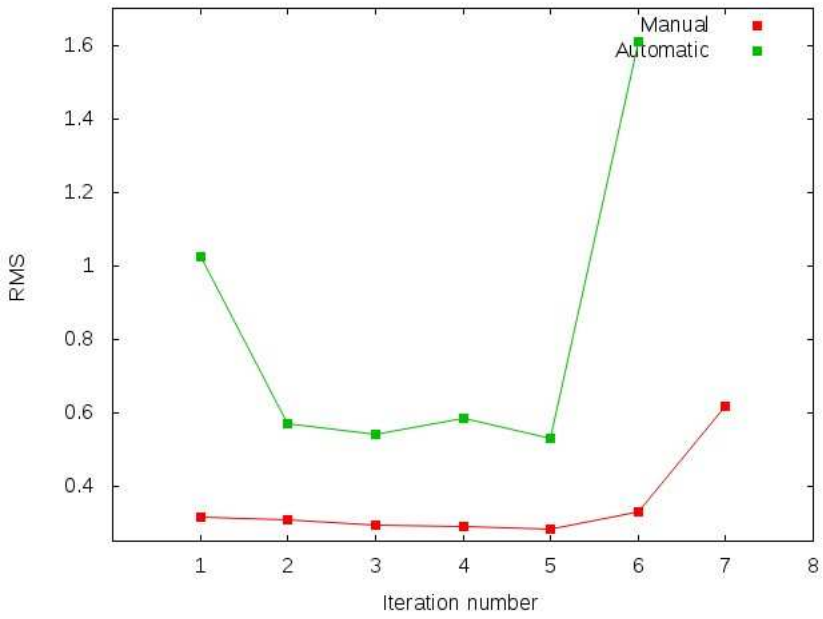

Figure 7.1: Rms values calculated at each tomographic iteration: green line for model B; red line for model A.

We can observe in figure 7.1,that the rms values of the model B are higher than that ones of the model A, and the model A solution is more stable than the model B ones. We have studied also the distribution of the rms values calculated for each event located using as velocity model that one produced by the tomography with the lowest rms value. In figure 7.2 are represented the rms values for the model B event locations and that ones for the model A.

As for the tomographic rms residuals, the model B produces higher values of rms at each location. But how much these comparisons influence the final results? How much different are the velocity models and the locations estimated?

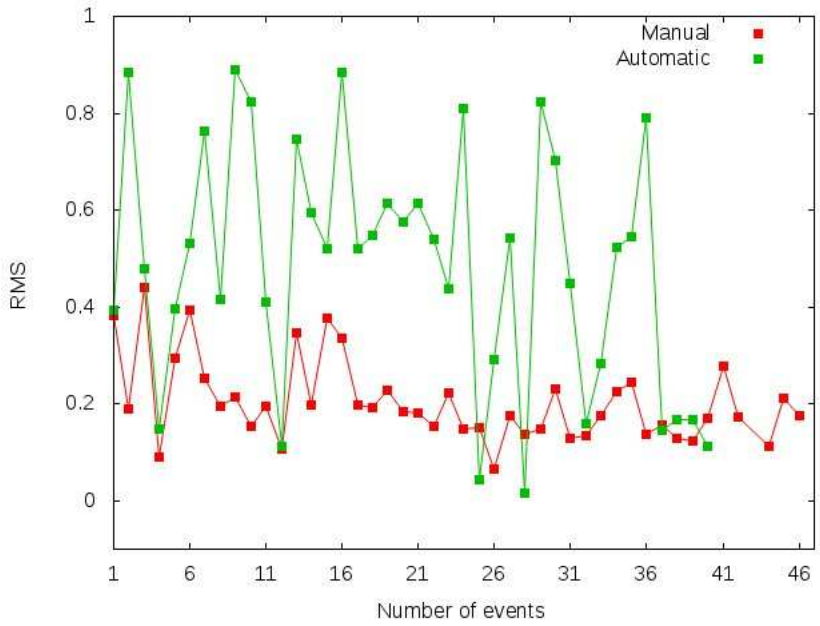

Figure 7.2: Rms residuals calculated for each event located using as velocity model that one with the lowest rms value (see figure 7.1) using model B (green line) and using model A (red line)

7.2.1 Location results

We report the locations obtained using the velocity models (at iteration 5 for model A and B (see figure 7.1) with the lowest RMS. In figure **??**(on map) the event locations in red are the ones produced with the model A, the green ones with model B; the stars are the main events. The manual and automatic locations are comparable and are similarly clustered in the epicenters area. It is to point out, as done in chapter 6, that the two solutions of the main event of the 20th of May, are more scattered than the two of the 29th May. This could be due to the presence of a large amount of registrations for the 29th's respect the 20th's, because of the installation of many temporary instruments near the epicenter region following the main shock of the 20th May 2012.

In figure 7.4 we report the event locations along a section (N - S) in depth. From this rapresentation of the results, as from the previous, it is not possible to assume that the manual and automatic solutions are severely different from each other. The depth of the two main events are pictured by stars, and also in this case the 20th's depths are more distant than the 29th's ones.

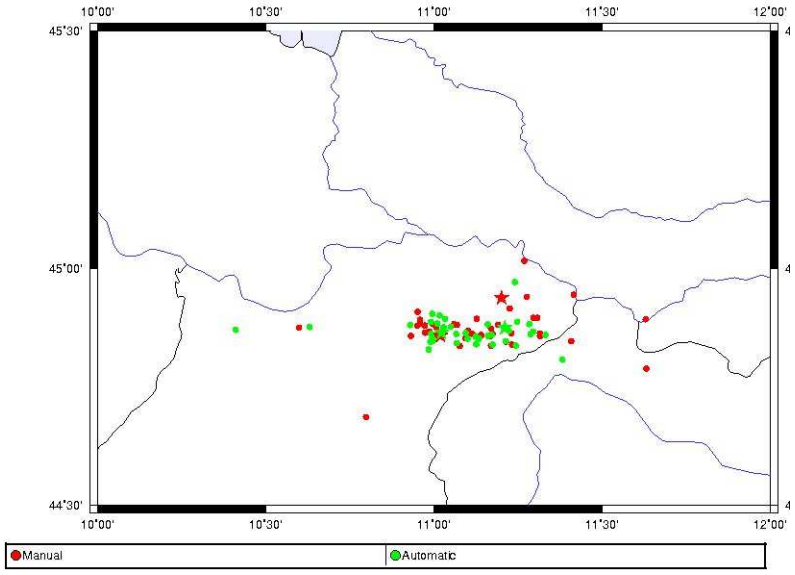

Figure 7.3: Map of the located events: the red dots are the events produced using model A, the green dots are the events obtained using model B; the stars are the main events

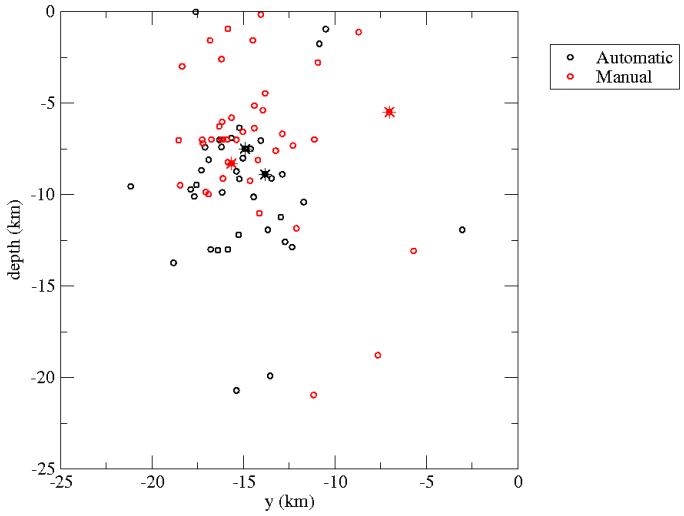

Figure 7.4: Section of the located events: the red dots are the events produced using as tomographic input the model A, the black dots are the events obtained using model B; the stars are the main events

7.2.2 Tomographic results

We present the tomographic results along a section perpendicular to the event locations, shown in figure 7.5.

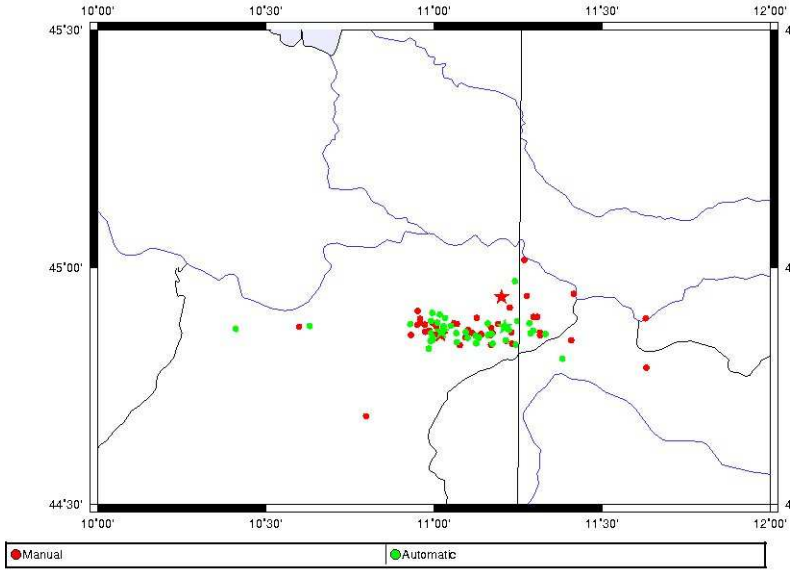

Figure 7.5: Map of the located events with a (N-S) section (black line): the red stars are the events producted using as tomographic input the model A, the green stars are the events obtained using model B

In figure 7.6 and 7.7 are represented (using the same color scale for the velocity values for both the images) the manual Vp velocity models (model A) and the automatic Vp velocity models (model B), respectively. The white pixels represent the parts not covered by seismic rays. In figure 7.10 is represented the same velocity field of figure 7.9, where the smoothed colors represent poor ray coverage.

The two velocity models seems to be similar, even if the automatic rms values are systematically higher than the manual ones.

The Vs velocity models, manual and automatic are in figures 7.8 and 7.9, respectively. The figure 7.10, is reported to really figure out that the reliable pixels are only the ones at the center of the model grid. This is what we expect, in fact our events are collocated all at the center of the grid with depths between 5 to 20 kilometers.

Comparing the figures 7.8 and 7.9 considering as reliable the colored pixels of figure 7.10, as for the Vp velocity models, also the Vs velocity models seem not to be so different each other.

As final tomographic result, we present the Vp/Vs ratio in figures 7.11 and 7.12. As for the Vs models, in figure 7.13 is represented the Vp/Vs velocity model with a threshold value of 10%.

As for the Vp velocity models, and for the Vs models, the Vp/Vs ratio

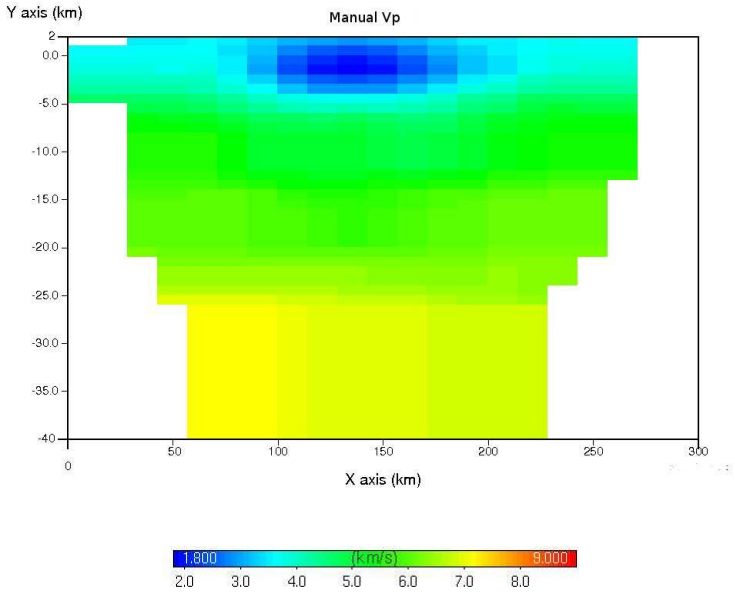

Figure 7.6: Vp velocity model obtained using model B as input.

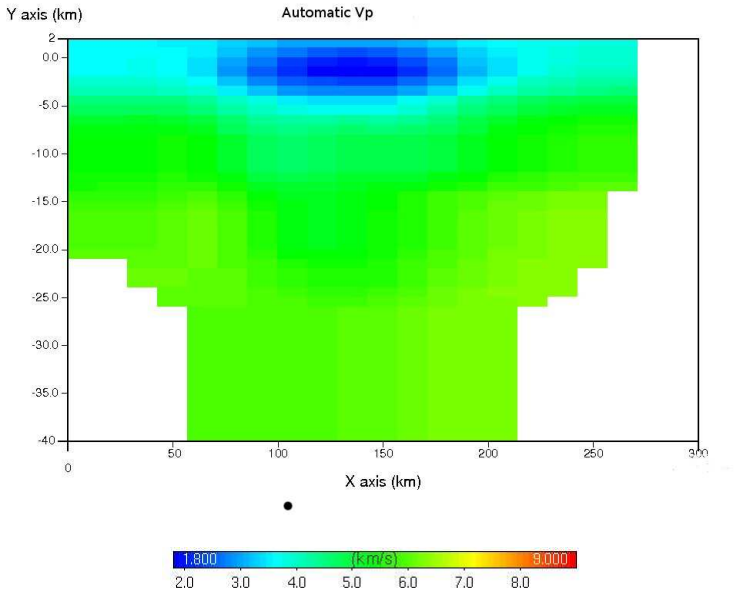

Figure 7.7: Vp velocity model obtained using model A as input

models (figures 7.11 and 7.12), as we expected, do not differ to much from each other.

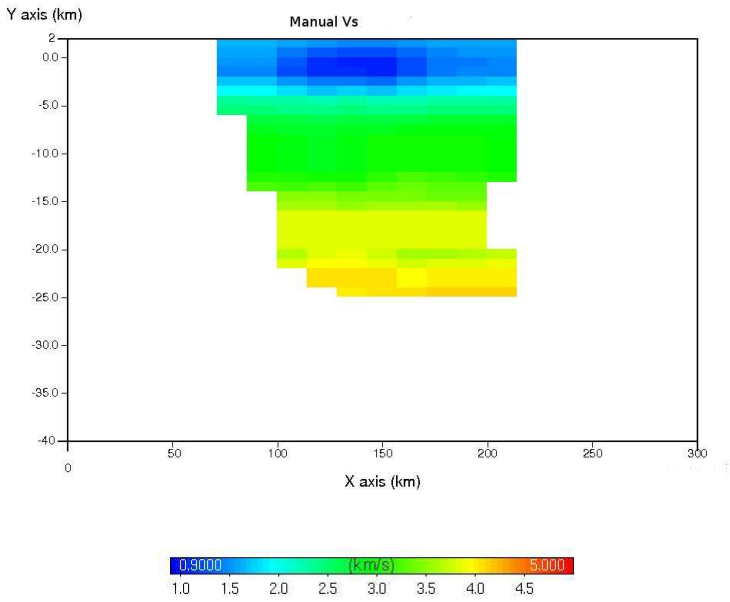

Figure 7.8: Vs velocity model obtained using model A as input

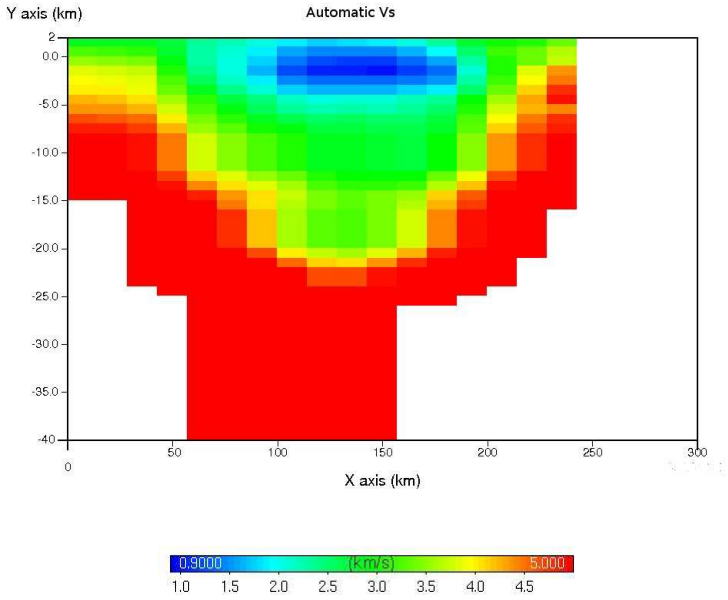

Figure 7.9: Vs velocity model obtained using model B as input

7.3 Conclusions

We have done an additional study to understand, if, using automatic phases as input for the travel time tomography, the resulting velocity models and

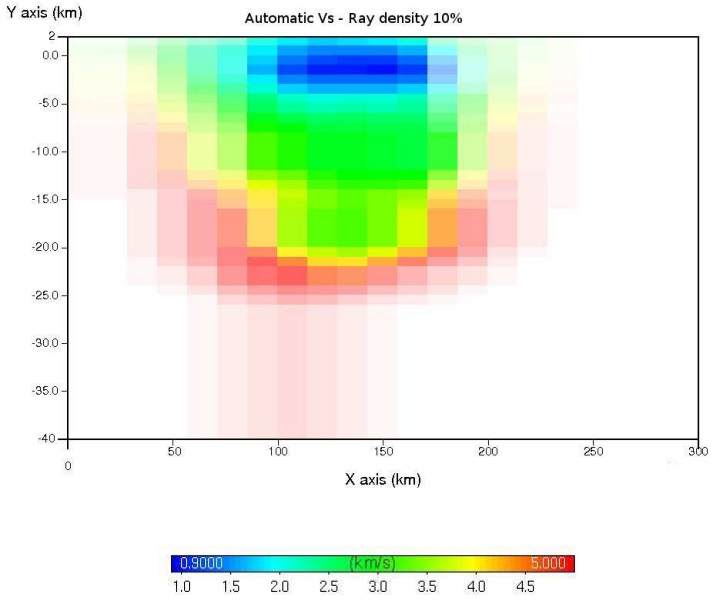

Figure 7.10: Vs velocity model obtained using model B as input with smoothed pixels color, depending on the ray coverage

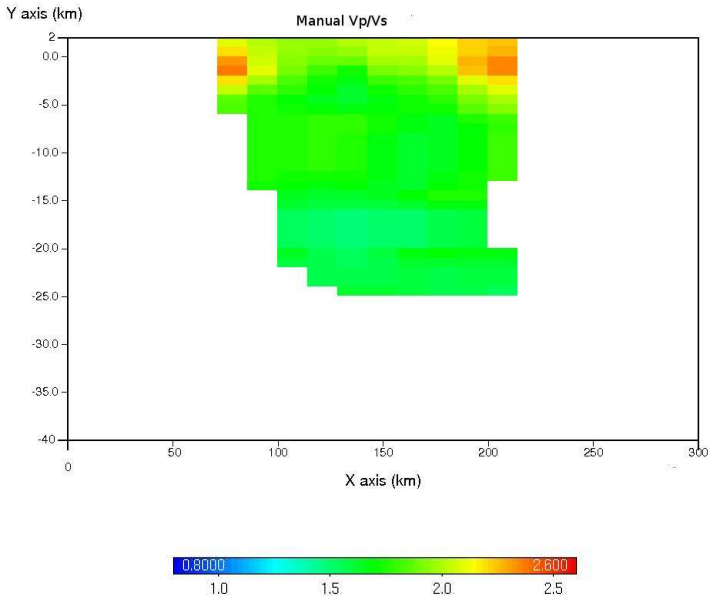

Figure 7.11: Vp/Vs ratio model obtained using model A as input

locations are reliable and significant as that ones produced with the manual revised phases. This test was done comparing the velocity models and

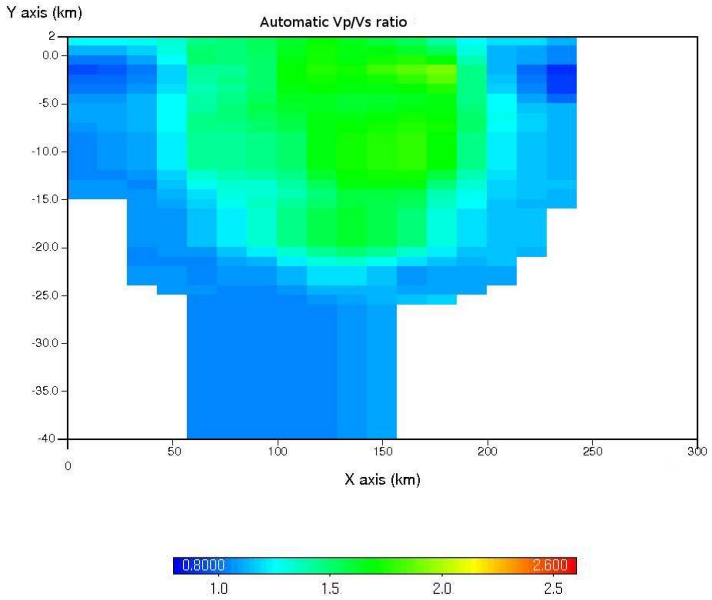

Figure 7.12: Vp/Vs ratio model obtained using model B as input

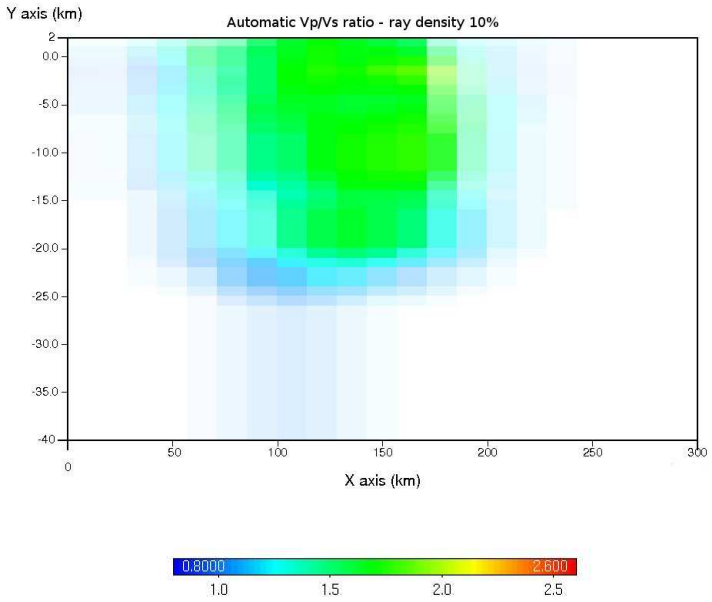

Figure 7.13: Vp/Vs ratio model obtained using model B as input, wth smoothed colored pixels, depending on the ray coverage

the events locations obtained with the tomographic procedure starting from manual and automatic phase picking. The obtained results, indicate an in-

crease of the average rms residuals both on the events locations and on the travel time inversion. Despite that, the tridimensional velocity models (Vp, Vs and Vp/Vs) are comparable, so it seems that the location's errors do not influence the tomographic results but the precision of the tomographic system. So for a large database it is possible to use the automatic phases as input, considering that the errors produced are in the ranges of location errors.

Conclusions

The main purpose of this study is the production of a routine that will accurately locate seismic event in real-time. The quality of the locations strongly depends on the correct determination of the P- and S- phases. For this reason we compared and evaluated different procedures of picking and location.

One of the procedures used in this work, is the AutoPicker. In order to test its performances, we applied it to a database of 250 events recorded in the year 2011, by the C3ERN Network at the Alps-Dinarides contact. Out of 3100 P-phase onsets our implementation detects 85% and gives a mean difference of -0.012 sec. For S-phase our implementation detects 70% and gives a mean difference of 0.072 sec. For hypocentral distances less than 60 km we found that about 95% of P autopicks are within 0.1 sec of manual picks. For S phases about 85% of autopicks are within 0.2 sec of the manual picks. For more than 90% events the epicentral difference is less than 5 km. The average value of differences between depths is 0.4 km and the standard deviation is 3.9 km. The proposed automatic picker appears to be a useful tool for assigning automatically onset P and S times to detected seismic signals for the purpose of rapid epiceter calculations. Provided, however, that an high frequency filtering is applied to broad-band data and a priori information (time windows for the AIC function application) is needed to guide the picker. This encouraging results have allowed us to proceed comparing this new picking methodology to another one, tested and used daily and in real-time by us to detect and locate events, the Antelope software.

After the occurrence of the Emilia seismic sequence in May-June 2012, we have decided to investigate it as an interesting study case. We manually picked the phases of the events with $M_l \geq 4.0$, and elaborated them to produce the event locations with the Hypoellipse software, using different velocity models found in literature: Bragato et al. [2011], Ciaccio and Chiarabba [2002],Costa et al. [1992], Iside, Zollo et al. [1995], Malagnini et al. [2012], Massa [2012] and four geological models proposed by Lavecchia et al. [in prep.]. The idea is to produce a set of clustered event locations with

the lowest residuals, in order to understand which is the generating fault in the complex system of faults. The resulting solutions are quite similar, therefore, there is not a favourite velocity model in terms of rms vertical and horizontal errors, even if all the velocity models used differ quite a lot.

After that, we located these sequence of events using the HypoDD software, based on the double differences technique, in order to determine, in a quantitative mode, the degree of clusterization of two or more events in the considered area. The HypoDD algorithm did not locate all the events as Hypoellipse did, because it clustered the solutions, but not so much to identify the best velocity model.

To proceed our analysis we have excluded from the statistical analysis, all the 'bad' events. An event is defined 'bad', or of a D-quality when the rms is upper then 0.5 and the SEH (the horizontal 68% confidence limit in the least-well-constrained direction) is upper than 5.0. We have eliminated from our statistical study the events which have a D-quality station distribution, which it means that the number of phases are less than 6, the GAP (largest azimuthal separation between stations from the epicenter) is upper than 180 and the distance between the event location and the nearest station is upper than 50 km. From 48 events we examine only the 41 with best quality. We have decided to eliminate from the final tests the models: 'Iside', because it is an average model from all the Italian territory; 'Ciaccio' because it is the starting point from the Massa [2012] model. We have chosen only one of the four geological models because they are similar. By the study of the mean residuals and rms, as in the previous data set, it is not possible to discriminate a velocity model with respect to the others. We have selected the velocity models: Costa et al. [1992]; Massa [2012] and the NewModel1 [Lavecchia et al., in prep.] as the best ones among the analyzed ones, because they have vertical error st.deviation values lower than 1 km.

The locations obtained using these three models, are similar. From the hypocentral distribution, it seems that the Mirandola thrust was not involved during the Emilia sequence, whereas the internal and middle segments of the Ferrara thrust systems were activated by 29 and 20 May seismic sequences, respectively.

Using 1-D velocity models the solutions are unstable, in order to stabilise them, we located the seismic events in a 3-D velocity model. To do that we have made a travel time tomography, applying the Cat3D software at the Emilia sequence. Because of the seismic sequence interests only a small part of this region (about $30x30\,km^2$ wide and 0-20 km deep), the investigated area will be limited to the upper crust. As initial velocity models, we have chosen those ones: Costa et al. [1992]; Massa [2012] and the NewModel1 [Lavecchia et al., in prep.] that have vertical errors lower than one km. The travel

time tomography and the event location are performed, respectively, using Cat3D software and NonLinLoc software through an iterative procedure. At each tomographic step, we have calculated the rms of the time residuals (the difference between computed and picked travel times). The solutions, obtained using as initial model the Costa et al. [1992], are unstable and with the higher rms values than the other solutions. The best velocity model is the one, obtained using as initial model the Massa [2012], which shows rms values lower than the others. The three resulting 3-D Vp velocity models shows similar characteristcs: a surface layer (0 5 km) of low Vp velocity, about 1,8 km/s, and a thick layer (5 20 km) of 5.5 km/s. The tomographic results for Vs velocity model present a common shallow layer (0 - 3 km) of low velocity (about 1 km/s) and a thick layer (3 - 13 km) characterized by a Vs velocity value of about 3.0 km/s.

The three set of solutions, from the different velocity models, are comparable in the errors range. The locations for the main-shock of the 20th of May, 2012 are more scattered respect the solutions for the 29th's. A possible reason could be the installations of temporary stations in the near field of the sequence after the 20th of May, 2012. For the 29th event, in fact, we have more waveforms than for the previous main-shock, and all of them in the near field. We calculated the rms for each event in order to discriminate a velocity model with respect to another from the quality of the locations. We obtained three similar rms values trends, so we were not able to choose a best velocity model. The events locations from 3-D tomographic models are less scattered than those one computed from the 1-D ones; otherwise the locations of the two main-shock events seem to be quite similar. In depth the two set of solutions do not differ in a significative way.

Based on the previous results of the AutoPicker application, we compared it with a more tested and solid method, the Antelope picking and locator method using as reference pickings and locations the manual ones. This comparison it is fundamental to understand which one of the two algorithms better detects phases and/or locates event. Our reference data set consists of the Emilia sequence of 2012 occurred in May-June. For P-phases, the distributions of differences between the manual and the two automatic P-onsets are comparable, as their average values. It is to point out that the AutoPicker procedure gives a standard deviation value lower than the Antelope ones and, most important, it picks the 16% of P-onsets more than the other algorithm. For S-phases the AutoPicker algorithm picks 178 onsets with a mean difference value of 0.09 sec, instead of the Antelope 16 S-phases with a mean difference value of 3.75 sec with respect to the manual ones. For more than 90% events the epicentral differences of AutoPicker is less than 5 kms, instead of the Antelope differences which are less than 10 kms. For

the depth differences the mean values and the distributions are quite similar, even if Antelope locates only 38 of the 44 events studied, despite of the 43 of the AutoPicker.

AutoPicker finds more and preciser phases than Antelope both P- and mainly S-phases. Despite that the associator process in Antelope, is able to correctly associate the detections and to find the correct location. The obtained results suggest us to implement the AutoPicker algorithm in the Antelope procedure in order to use the AutoPicker to define P- and S-onset and Antelope to associate them and locate the events.

We have done an additional study to understand, if, we introduce errors in the estimation of the velocity models and the locations, using automatic AutoPicker phases as input for a travel time tomography. The obtained results indicate an increase of the average rms both on the locations and on the tomography. Despite that, the tridimensional velocity models (Vp, Vs and Vp/Vs) are comparable, therefore, it seems that the location errors do not influence the tomographic results but the precision of the tomographic system. So for a large database it is possible to use automatic phases as input in a travel-time tomography, obtaining similar results as those obtained using manually picked phases.

Acknowledgements

I thank Dott. Gaultiero Bohm, Dott. Rita De Nardis and Prof. Daniele Spallarossa for tremendous help and support during this thesis. I should like to thank Dott. Luisa Filippi and Prof. Peter Suhadolc for fruitful discussions on various aspects of this study. Last but not least I express my gratitude to Dr. Giovanni Costa for help and support during these three years.

Bibliography

Akaike and Hirotugu. A new look at the statistical model identification. *IEEE Transactions on Automatic Control*, 19(6):716–723, 1974.

K. Aki. Three-dimensional inhomogeneities in the lithosphere and asthenosphere: Evidence for decoupling in the litosphere and flow in the astenosphere. *Rev. Geophys. Space Phys.*, 20(-):161–170, 1982.

P. L. Bragato, M. Sugan, and P. Augliera. Moho Reflection Effects in the Po Plain (Northern Italy) Observed from Instrumental and Intensity Data. *Bulletin of the Seismological Society of America*, 101(5):2142–2152, 2011.

M.G. Ciaccio and C. Chiarabba. Tomographic models and seismotectonics of the Reggio Emilia region, Italy. *Tectonophysics*, 344(-):261–276, 2002.

G. Costa, G.F. Panza, P. Suhadolc, and F. Vaccari. Zoning of the Italian region with synthetic seismograms computed with known structural and source information. 1992.

G. Costa, , L. Moratto, and P. Suhadolc. The Friuli Venezia Giulia Accelerometric Network RAF. *Bullettin of Earthquake Eng.*, 2009.

M. Dolce, M. Nicoletti, A. Ammirati, R. Bianconi, L. Filippi, A. Gorini, S. Marcucci, F. Palma, E. Zambonelli, G. Lavecchia, R. De Nardis, F. Brozzetti, P. Boncio, D. Cirillo, A. Romano, G. Costa, A. Gallo, L. Tiberi, G. Zoppe, P. Suhadolc, F. Ponziani, and A. Formica. The Emilia Thrust Earthquake of 20 May 2012 (Northern Italy): Strong Motion and Geological Observations Report 1. Technical report, 2012.

L. Geiger. Herbesetimmung bei Erbeben aus den Ankunfzeiten. *K. Gessell, Wiss. Goett.*, 4(-):331–349, 1910.

L. Geiger. Probability method for the determination of earthquake epicenters from the arrival time only. *Bulletin of St. Louis University*, 8(-):60–71, 1912.

L. Geldart and R. Sheriff. Problems in exploration Seismology and their solutions. *Society of Exploration Geophysicists*, 14(-):–, 2004.

A. Gorini, M. Nicoletti, P. Marsan, R. Bianconi, R. De Nardis, L. Filippi, S. Marcucci, F. Palma, and E. Zambonelli. The Italian Strong Motion Network. *Bull.Earth.Eng.*, 8(-):1075–1090, 2010.

A. Govoni, A. Marchetti, P. De Gori, M. Di Bona, F.P. Lucente, L. Improta, C. Chiarabba, A. Nardi, L. Margheriti, N.P. Agostinetti, R. Di Giovambattista, D. Latorre, M. Anselmi, M.G. Ciaccio, M. Moretti, C. Castellano, and D. Piccinini. The 2012 Emilia seismic sequence (Northern Italy): Imaging the thrust fault system by accurate aftershocks location. *Tectonophysics*, -(-):–, 2014.

J.C. Lahr. *HYPOELLIPSE: a computer program for determining local earthquake hypocentral parameters, magnitude, and first-motion pattern: U.S. Geological Survey Open-File Report 9923.* http://pubs.usgs.gov/of/1999/ofr-99-0023/, 1979.

G. Lavecchia, R. De Nardis, D. Cirillo, F. Brozzetti, and P. Boncio. The May-June 2012 Ferrara Arc earthquakes (northern Italy): structural control of the spatial evolution of the seismic sequence and of the surface pattern of coseismic fractures. *Annals of Geophysics*, 55(4), 2012.

G. Lavecchia, R. De Nardis, L. Tiberi, G. Costa, F. Brozzetti, D. Cirillo, F. Ferrarini, and L. Filippi. Seismogenic thrusting in Italy - new earthquake data and constraints on structural style from the 2012 Ferrara seismic sequence (M_w 6.1). *To be submitted to Tectonphysics*, in prep.

M. Leonard. Comparison of manual and automatic onset time picking. *Bulletin of Seismological Society of America*, 90(6):1384–1390, 2000.

M. Leonard and B. L. N. Kennett. Multi-component autoregressive techniques for the analysis of seismograms. *Phys Earth Planet Interior*, 113 (2):247–264, 1999.

A. Lomax, J. Virieux, P. Volant, and C. Berge. Probabilistic earthquake location in 3D and layered models: Introduction of a Metropolis-Gibbs method and comparison with linear locations. *Advances in Seismic Event Location*, -(-):101–134, 2000.

N. Maeda. *A method for reading and checking phase times in auto-processing system of seismic wave data.* Zisin=Jishin 38:365379, 1985.

L. Malagnini, R.B. Hermann, I. Munaf, M. Buttinelli, M. ad Anselmi, A. Akinci, and E. Boschi. The 2012 Ferrara seismic sequence: Regional crustal structure, earthquake sources, and seismic hazard. *Geophysical Research Letters*, 39, 2012.

M. Massa. Report di Progetto, DPC-INGV 2012-2013 Deliverable D18b2. Technical report, 2012.

Cat3D user manual(versione 0). OGS and Paneura, November 2008.

G.L. Pavlis, F. Vernon, D. Harvey, and D. Quinlan. The generalized earthquake-location (GENLOC) package: an earthquake-location library. *Computer&Geosciences*, 30(-):1079–1091, 2004.

L. Scognamiglio, L. Margheriti, Mele F.M., E. Tinti, A. Bono, P. De Gori, V. Lauciani, F.P. Lucente, A.G. Mandiello, C. Marcocci, S. Mazza, S. Pintore, and M. Quintillani. The 2012 Pianura Padana Emiliana seimic sequence: locations, moment tensors and magnitudes. *Annals of Geophysics*, 55(4):549–559, 2012.

R. Sleeman and T. Van Eck. Robust automatic P-phase picking: an on-line implementation in the analysis of broad band seismogram recordings. *Phys Earth Planet Interior*, -(113):265–275, 1999.

R. Stewart. Exploration Seismic Tomography: Fondamentals. Corse note series. *SEG Society of Exploration Geophysicists*, 3:–, 1993.

C.H. Thurber. Analisys methods for kinematric data from local earthquakes. *Rev.Geophys.*, -(24):793–805, 1986.

C. Turino, P. Morasca, G. Ferretti, D. Scafidi, and D. Spallarossa. Reliability of the automatic procedures for locating earthquakes in southwestern Alps and northern Appennines (Italy). *Journal of Seismology*, 14(5):393–411, 2010.

F. Waldhauser and W.L. Ellsworth. A Double-Difference Earthquake Location Algorithm: Method and Application to the Northern Hayward Fault, California. *Bulletin of the Seismological Society of America*, 90(6):1353–1368, 2000.

E. Weber, G. Iannaccone, A. Zollo, A. Bobbio, L. Cantore, M. Corciulo, V. Convertito, M. Di Crosta, L. Elia, A. Emolo, C. Martino, A. Romeo, and C. Satriano. Development and testing of an advanced monitoring

infrastructure (ISNet) for seismic early-warning applciations in the Campania region of the southern Italy. *Seismic Early Warning Springer-Verlag*, 2006.

E. Zambonelli, R. De Nardis, L. Filippi, M. Nicoletti, and M. Dolce. Performance of the Italian strong motion network during the 2009, L'Aquila seismic sequence (Central Italy). *Bullettin of Earthquake Engineering*, 9 (1):39–65, 2011.

H. Zhang, C. Thurber, and C. Rowe. Automatic P-wave arrival detection and picking with multiscale wavelet analysis for single-component recordings. *Bulletin of the Seismological Society of America*, 93(5):1904–1912, 2003.

A. Zollo, R. De Matteis, P. Capuano, F. Ferulano, and G. Iannaccone. Constaints on the shallow crustal model of the northern Apeninnines (Italy) from the analysis of microearthquake seismic records. *Geophysical Journal International*, 120(3):646–662, 1995.